박사 학위논문
Ph. D. Dissertation

3차원 탄성 부유체의 정적/동적 해석을 위한 수치해석 기법 개발

Numerical methods for hydro -static and -dynamic analysis of 3D elastic floating structures

이 강 헌 (李 剛 憲 Lee, Kang-Heon)
기계항공공학부, 기계공학과
School of Mechanical and Aerospace Engineering
Department of Mechanical Engineering

KAIST

2016

3차원 탄성 부유체의 정적/동적 해석을 위한 수치해석 기법 개발

Numerical methods for hydro -static and -dynamic analysis of 3D elastic floating structures

Numerical methods for hydro -static and -dynamic analysis of 3D elastic floating structures

Advisor : Professor Lee, Phill-Seung

by

Lee, Kang-Heon
School of Mechanical and Aerospace Engineering
Department of Mechanical Engineering
KAIST

A thesis submitted to the faculty of KAIST in partial fulfillment of the requirements for the degree of Doctor of Philosophy in the School of Mechanical and Aerospace Engineering, Department of Mechanical Engineering . The study was conducted in accordance with Code of Research Ethics[1].

2015. 11. 13.

Approved by

Professor Lee, Phill-Seung

[Advisor]

____

[1]Declaration of Ethical Conduct in Research: I, as a graduate student of KAIST, hereby declare that I have not committed any acts that may damage the credibility of my research. These include, but are not limited to: falsification, thesis written by someone else, distortion of research findings or plagiarism. I affirm that my thesis contains honest conclusions based on my own careful research under the guidance

3차원 탄성 부유체의 정적/동적 해석을 위한 수치해석 기법 개발

이 강 헌

위 논문은 한국과학기술원 박사학위논문으로
학위논문심사위원회에서 심사 통과하였음.

2015년 11월 13일

심사위원장 이 필 승 (인)

심사위원 권 순 홍 (인)

심사위원 홍 사 영 (인)

심사위원 김 진 환 (인)

심사위원 정 현 (인)

of my thesis advisor.

DME
20117039

이 강 헌. Lee, Kang-Heon. Numerical methods for hydro -static and -dynamic analysis of 3D elastic floating structures. 3차원 탄성 부유체의 정적/동적 해석을 위한 수치해석 기법 개발. School of Mechanical and Aerospace Engineering, Department of Mechanical Engineering . 2016. 106p. Advisor Prof. Lee, Phill-Seung. Text in English.

ABSTRACT

In this work, a numerical method for a 3D linear hydroelastic analysis of floating structures with liquid tanks subjected to surface regular water waves is developed and compare the numerical results with experimental tests. Considering direct couplings among structural motion, sloshing, and water waves, a mathematical formulation and a numerical method are developed. The finite element method is employed for the floating structure and internal fluid in tanks, and the boundary element method is used for the external fluid. The resulting formulation completely incorporates all the interaction terms including hydrostatic stiffness and the irregular frequency effect is removed by introducing the extended boundary integral equations.

Important issues of the 3D hydroelastic problem are the complete inclusion of hydrostatic stiffness and hydrostatic equilibrium of elastic floating structures. The hydrostatic stiffness is composed of the sum of the hydrostatic pressure and initial stress effects. Therefore, an explicit expression of geometric stiffness that is related to the hydrostatic pressure is required, and the hydrostatic analysis should be pre-performed before the hydrodynamic analysis to obtain the initial stress fields.

An updated Lagrangian finite element (FE) formulation for a geometrically nonlinear hydrostatic analysis of flexible floating structures subjected to buoyancy, self-weight, and various external static loads is developed. The nonlinear equation is linearized with respect to a reference configuration and the resulting FE formulation is iteratively solved using the Newton-Raphson method. A special numerical integration technique is developed to handle the wet-surface change without re-meshing. Through the proposed numerical method, the hydrostatic equilibrium can easily be calculated considering various static and quasi-static loading conditions and the stress field of elastic bodies is more accurately evaluated in a large deformation case.

Contents

List of Tables

List of Figures

Chapter 1. Introduction

For a long time, the hydrodynamic analysis of floating structures has been typically based on the rigid body assumption. The rigid body hydrodynamic analysis has been deemed adequate for the design of floating structures where rigid body motions are dominant. However, as the size of floating structures is getting larger to the extent that the flexible motions of floating structures account for a substantial portion of the hydrodynamic responses, the rigid body assumption is no longer resonable for the hydrodynamic analysis of floating structures.

More recently, the hydrodynamic analysis of floating liquid storage structures subjected to surface regular waves has been widely studied due to the significant increase in demand for floating production storage and offloading (FPSO) units, floating liquefied natural gas (FLNG) units, and other related structures. Recently, the size and the weight of floating liquid storage structures are becoming increasingly greater in tandem with growing market demand and on the basis of their economic benefits. In such floating structural systems, the assumption of rigid body motions is no longer suitable because, as the dimensions of floating structures increase, the overall stiffness decreases, resulting in relatively low resonant frequencies close to the range of excitation frequencies and sloshing resonance frequencies.

Most previous studies mainly addressed the coupling effect between rigid body motions and sloshing. However, the size and the weight of floating liquid storage structures are becoming increasingly greater in tandem with growing market demand and on the basis of their economic benefits. In such floating structural systems, the assumption of rigid body motions is no longer suitable because, as the dimensions of floating structures increase, the overall stiffness decreases, resulting in relatively low resonant frequencies close to the range of excitation frequencies and sloshing resonance frequencies. In spite of the increasing importance of the hydroelastic behavior of floating liquid storage structures, few related studies have been reported. Accordingly, a complete mathematical formulation has not been developed and the numerical results have not been verified by experimental studies.

Important issues for the general 3D hydroelastic problem are the explicit inclusion of hydrostatic stiffness and the use of accurate hydrostatic equilibrium of elastic floating structures. The hydrostatic stiffness is related to the sum of the hydrostatic pressure and initial stress effects. Therefore, an explicit expression of geometric stiffness that is related to the hydrostatic pressure is essential, and the hydrostatic analysis should be pre-performed before the hydrodynamic analysis.

Until now, the hydrostatic equilibrium has been calculated based on the rigid body assumption using various methods, where floating structures are assumed to be rigid. While those methods are simple, they are not always applicable to flexible structures and require additional works (such as pressure projection) to calculate the stress fields of floating structures caused by hydrostatic pressure. Recently, the importance of hydrostatic stiffness in hydroelastic analyses has been extensively investigated. A hydrostatic analysis has become a prerequisite to obtain stress fields required for constructing the complete hydrostatic stiffness in hydroelastic analyses.

Nevertheless, it is hard to find methods to accurately calculate the hydrostatic equilibrium (and stress fields) of flexible floating structures. Basically, the hydrostatic analysis of floating structures is nonlinear, mainly because of large motion and wet-surface change. Furthermore, when floating structures are modeled using finite elements, difficulty arises from non-matching between the finite element mesh and the free surface. Such non-matching mesh problems frequently occur in the analysis of fluid-structure interaction problems and proper treatment is an important issue in numerical analyses

.

Therefore, a general method to calculate the hydrostatic equilibrium of 3D flexible floating structures, by which accurate draft and stress fields of structures should be developed in collaborate with the development of numerical method for 3D hydroelasticity.

Chapter 2. Hydrostatic analysis

2.1 Introduction

In ocean environments, floating structures such as ships, offshore platforms, and offshore facilities are always subjected to various hydrostatic and quasi-static loads (e.g. structural weight, ballast water weight, and cargo weight) [1]. Calculating hydrostatic equilibrium is basic and important for analyzing the stability and strength of floating structures.

For a long time, hydrostatic equilibrium has been calculated based on the rigid body assumption using various methods [2, 3, 4, 5, 6, 7, 8, 9], where floating structures are assumed to be rigid. While those methods are simple, they are not always applicable to flexible structures and require additional works (such as pressure projection) to calculate the stress fields of floating structures caused by hydrostatic pressure. Recently, the importance of hydrostatic stiffness in hydroelastic analyses has been extensively investigated [10, 11, 12, 13, 14, 15, 16, 17, 18, 19, 20, 21]. A hydrostatic analysis has become a prerequisite to obtain stress fields required for constructing the complete hydrostatic stiffness in hydroelastic analyses [10, 11, 12].

Nevertheless, it is hard to find methods to accurately calculate the hydrostatic equilibrium (and stress fields) of flexible floating structures. Basically, the hydrostatic analysis of floating structures is nonlinear, mainly because of large motion and wet-surface change. Furthermore, when floating structures are modeled using finite elements, difficulty arises from non-matching between the finite element mesh and the free surface. Such non-matching mesh problems frequently occur in the analysis of fluid-structure interaction problems and proper treatment is an important issue in numerical analyses [22, 23, 24].

The objective of this study is to develop a general method to calculate the hydrostatic equilibrium of 3D flexible floating structures, by which accurate draft and stress fields of structures are obtained. We employ an updated Lagrangian finite element formulation [25, 26] for a nonlinear hydrostatic analysis of flexible floating structures. After nonlinear terms are linearized, we obtain incremental equilibrium equations, which are iteratively solved using the Newton-Raphson method. Wet-surface change, normal vector change, and buoyancy change due to structural displacement are completely considered [10, 12]. To efficiently handle the non-matching mesh problem without re-meshing, a special numerical integration technique is developed. The proposed formulation and numerical method also can be used for a hydrostatic analysis of rigid floating structures as well as flexible floating structures.

The incremental equilibrium equations are presented in Section 2.2. The finite element discretization procedure and the equations for a rigid body analysis are derived in Section 2.3. In section 2.4, an effective numerical integration technique is developed and the feasibility of the proposed numerical procedure is demonstrated through various nonlinear hydrostatic problems in rigid and elastic body cases in Section 2.5.

2.2 Incremental equilibrium equation

As shown in Figure 2.1(a), a three-dimensional (3D) flexible structure is floating in calm water and a fixed Cartesian coordinate system (x_1, x_2, x_3) is introduced. The structural material is assumed to be homogeneous, isotropic, and linear elastic. In the initial state, the floating structure does not interact with water. Through a nonlinear hydrostatic analysis, we can obtain the hydrostatic equilibrium, where the external forces (e.g. surface force, body force, and hydrostatic pressure) are balanced, as shown in Figure 2.1(b). The volume and surface of the floating structure are denoted by V and S, respectively. In particular, hydrostatic pressure is applied on the wet-surface, S_w.

The incremental equations for the freely floating structure are obtained through the updated Lagranagian formulation [25, 26]. In Figure 2.2, two configurations are demonstrated and they are denoted by the left superscripts t and $t+\Delta t$, respectively. The material point vectors for the floating structure in the configuration at time t and $t+\Delta t$ are expressed by ${}^{t}x_i$ and ${}^{t+\Delta t}x_i$, respectively. The displacement vectors of the floating structure are then defined by

$$ {}^{t+\Delta t}_{t}u_i = {}^{t+\Delta t}x_i - {}^{t}x_i, \tag{2.1} $$

Also, the hydrostatic pressure fields are defined as

$$ {}^{t}P = -\rho_w g\, {}^{t}x_3, \quad {}^{t+\Delta t}P = -\rho_w g\, {}^{t+\Delta t}x_3, \tag{2.2} $$

where ρ_w is the density of water and g is the gravitational acceleration.

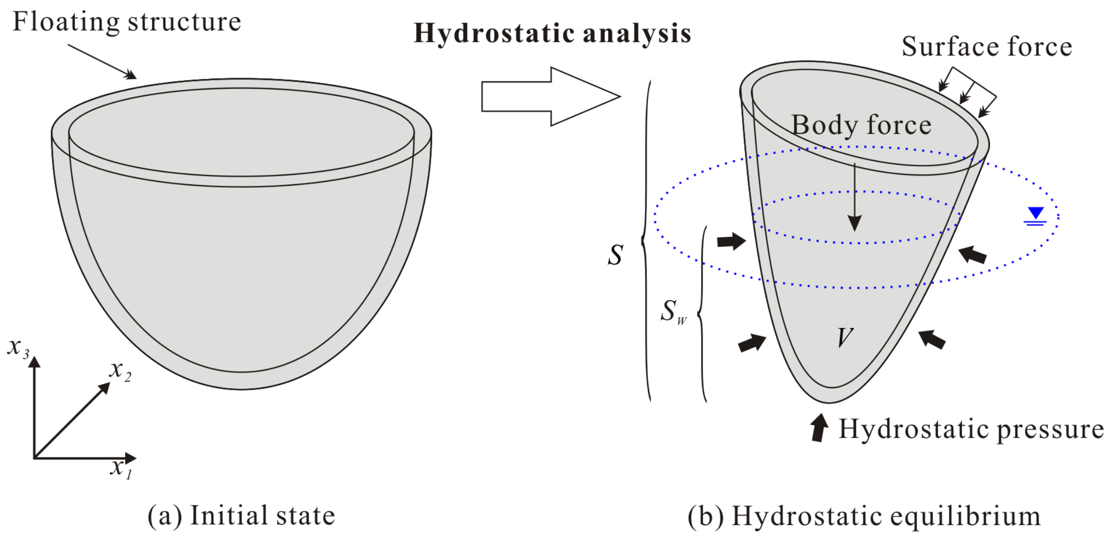

Figure 2.1: Hydrostatic analysis of flexible floating structure.

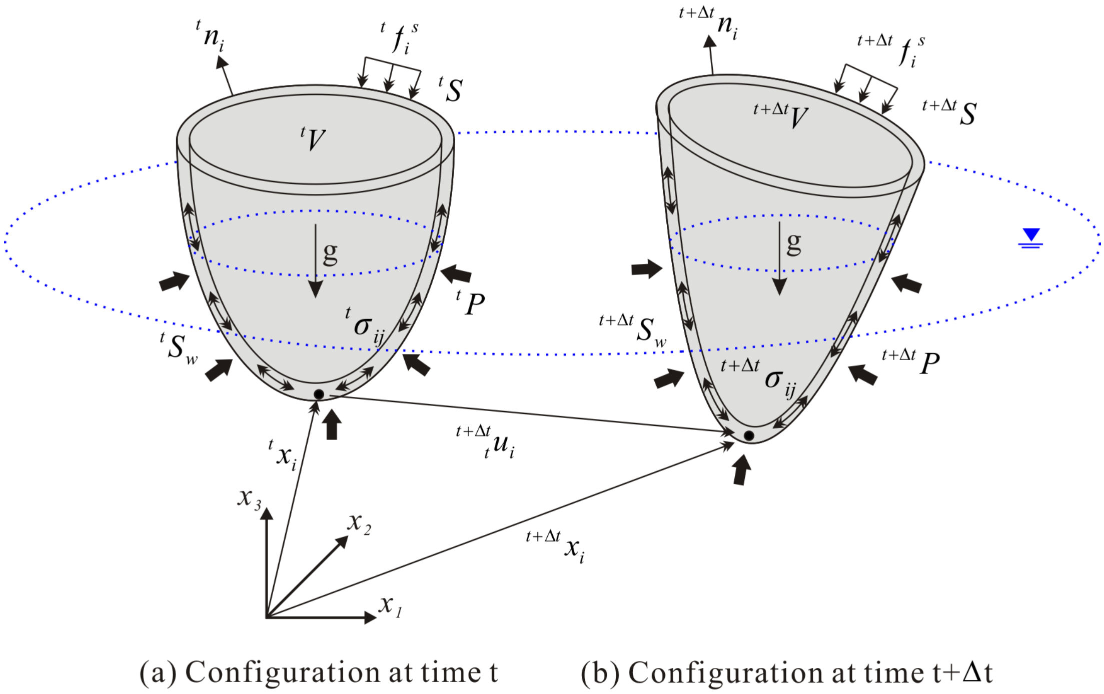

Figure 2.2: Two configurations of flexible floating structure.

The local equilibrium equations at time $t + \Delta t$ are given by

$$\frac{\partial^{t+\Delta t}\sigma_{ij}}{\partial^{t+\Delta t}x_j} - {}^{t+\Delta t}\rho_s g \delta_{i3} = 0 \qquad \text{in } {}^{t+\Delta t}V,$$

$${}^{t+\Delta t}\sigma_{ij}{}^{t+\Delta t}n_j = -{}^{t+\Delta t}P\ {}^{t+\Delta t}n_i \quad \text{on } {}^{t+\Delta t}S_w,$$

$${}^{t+\Delta t}\sigma_{ij}{}^{t+\Delta t}n_j = {}^{t+\Delta t}f_i^s{}^{t+\Delta t}n_i \qquad \text{on } {}^{t+\Delta t}S, \tag{2.3}$$

where σ_{ij} is the Cauchy stress tensor, f_i^s is the surface force, ρ_s is the density of the floating structure, n_i is the unit normal vector outward from the floating structure, and δ_{i3} is the Kronecker delta.

After applying the principle of virtual work at time $t + \Delta t$, the following weak formulation can be obtained:

$$\int_{{}^{t+\Delta t}V} {}^{t+\Delta t}\sigma_{ij}\delta_{t+\Delta t}e_{ij}\mathrm{d}^{t+\Delta t}V = -\int_{{}^{t+\Delta t}V} {}^{t+\Delta t}\rho_s g \delta u_3 \mathrm{d}^{t+\Delta t}V$$

$$+ \int_{{}^{t+\Delta t}S_w} \rho_w g\ {}^{t+\Delta t}x_3{}^{t+\Delta t}n_i \delta u_i \mathrm{d}^{t+\Delta t}S$$

$$+ \int_{{}^{t+\Delta t}S_w} {}^{t+\Delta t}f_i^s g\ {}^{t+\Delta t}n_i \delta u_i \mathrm{d}^{t+\Delta t}S \tag{2.4}$$

where $\delta_{t+\Delta t}e_{ij}$ is the virtual linear strain tensor that corresponds to the virtual displacements δu_i,

$$\delta_{t+\Delta t}e_{ij} = \frac{1}{2}\left(\frac{\partial \delta u_i}{\partial^{t+\Delta t}x_j} + \frac{\partial \delta u_j}{\partial^{t+\Delta t}x_i}\right). \tag{2.5}$$

We then obtain the incremental equilibrium equation for a nonlinear hydrostatic analysis after linearizing all the terms in Equation 2.4 with respect to the configuration at time t,

$$\int_{^tV} C_{ijrs}\,{}^{t+\Delta t}_{\;\;t}e_{rs}\delta_t e_{ij}\mathrm{d}^tV + \int_{^tV} {}^t\sigma_{ij}\delta\,{}^{t+\Delta t}_{\;\;t}\eta_{ij}\mathrm{d}^tV$$

$$-\int_{^tS_w} \rho_w g\ {}^{t+\Delta t}_{\;\;t}u_3\,{}^tn_i\delta u_i\mathrm{d}^tS - \int_{^tS_w} \rho_w g\ {}^tx_3\,{}^tn_j\ {}^{\;\;\;\;t}_{t+\Delta t}Q_{ij}\delta u_i\mathrm{d}^tS$$

$$= -\int_{^tV} {}^t\rho_s g\ \delta u_3\mathrm{d}^tV - \int_{^tV} {}^t\sigma_{ij}\delta e_{ij}\mathrm{d}^tV + \int_{^tS_w} \rho_w g\ {}^tx_3\,{}^tn_i\delta u_i\mathrm{d}^tS + \int_{^tS} {}^tf_i^s\ {}^tn_i\delta u_i\mathrm{d}^tS \tag{2.6}$$

with

$${}^{t+\Delta t}_{\;\;t}e_{ij} = \frac{1}{2}\left(\frac{\partial\,{}^{t+\Delta t}_{\;\;t}\delta u_i}{\partial^t x_j} + \frac{\partial\,{}^{t+\Delta t}_{\;\;t}\delta u_j}{\partial^t x_i}\right), \delta\,{}^{t+\Delta t}_{\;\;t}\eta_{ij} = \frac{1}{2}\left(\frac{\partial\delta u_k}{\partial^t x_i}\frac{\partial\,{}^{t+\Delta t}_{\;\;t}\delta u_k}{\partial^t x_j} + \frac{\partial\,{}^{t+\Delta t}_{\;\;t}\delta u_k}{\partial^t x_i}\frac{\partial\delta u_k}{\partial^t x_j}\right),$$

$${}^{\;\;\;\;t}_{t+\Delta t}Q_{ij} = \delta_{ij}\frac{\partial\,{}^{t+\Delta t}_{\;\;t}\delta u_k}{\partial^t x_k} + \frac{\partial\,{}^{t+\Delta t}_{\;\;t}\delta u_j}{\partial^t x_i}, \tag{2.7}$$

where ${}^{t+\Delta t}_{\;\;t}u_i$ is the displacement from the configuration at time t to the configuration at time $t+\Delta t$, ${}^{t+\Delta t}_{\;\;t}\eta_{ij}$ is the virtual nonlinear strain tensor, and C_{ijrs} is the stress-strain relation tensor. In Equation 2.6, all the static and kinematic variables refer to the configurations denoted by ${}^tV$, ${}^tS_w$, and ${}^tS$.

The iterative form of Equation 2.6, for the Newton-Raphson method, is for n=1, 2, ...,

$$\int_{^{t+\Delta t}V^{(n-1)}} C_{ijrs}\Delta_{t+\Delta t}e_{rs}^{(n)}\delta_{t+\Delta t}e_{ij}\mathrm{d}^{t+\Delta t}V + \int_{^{t+\Delta t}V^{(n-1)}} {}^{t+\Delta t}\sigma_{ij}^{(n-1)}\delta\Delta_{t+\Delta t}\eta_{ij}^{(n)}\mathrm{d}^{t+\Delta t}V$$

$$-\int_{^{t+\Delta t}S_w^{(n-1)}} \rho_w g\Delta_{t+\Delta t}u_3^{(n)}{}^{t+\Delta t}n_i^{(n-1)}\delta u_i\mathrm{d}^{t+\Delta t}S$$

$$-\int_{^{t+\Delta t}S_w^{(n-1)}} \rho_w g\ {}^{t+\Delta t}x_3^{(n-1)}{}^{t+\Delta t}n_j^{(n-1)}\Delta^{t+\Delta t}Q_{ij}^{(n)}\delta u_i\mathrm{d}^{t+\Delta t}S$$

$$= -\int_{^{t+\Delta t}V^{(n-1)}} {}^{t+\Delta t}\rho_s^{(n-1)}g\delta u_3\mathrm{d}^{t+\Delta t}V - \int_{^{t+\Delta t}V^{(n-1)}} {}^{t+\Delta t}\sigma_{ij}^{(n-1)}\delta e_{ij}\mathrm{d}^{t+\Delta t}V$$

$$+\int_{^{t+\Delta t}S_w^{(n-1)}} \rho_w g^{t+\Delta t}x_3^{(n-1)}{}^{t+\Delta t}n_i^{(n-1)}\delta u_i\mathrm{d}^{t+\Delta t}S + \int_{^{t+\Delta t}S^{(n-1)}} {}^{t+\Delta t}f_i^s\ {}^{t+\Delta t}n_i^{(n-1)}\delta u_i\mathrm{d}^{t+\Delta t}S, \quad (2.8)$$

where $\Delta_{t+\Delta t}e_{ij}^{(n)}$, $\Delta_{t+\Delta t}\eta_{ij}^{(n)}$, and $\Delta^{t+\Delta t}Q_{ij}^{(n)}$ are defined by substituting ${}^{t+\Delta t}_{\ \ t}u_i$ and ${}^tx_i$ with Δu_i and ${}^{t+\Delta t}x_i^{(n-1)}$ in Equations 2.6 and 2.7, respectively, and Δu_i refers to the increment of the structural displacement at the iteration n.

Note that in Equations 2.8, all the quantities with superscripts $(n-1)$ and (n) are evaluated to the configuration updated at the iteration n, i.e., ${}^{t+\Delta t}V^{(n-1)}$, ${}^{t+\Delta t}S_w^{(n-1)}$, and ${}^{t+\Delta t}S^{(n-1)}$, where ${}^{t+\Delta t}V^{(0)} = {}^tV$, ${}^{t+\Delta t}S_w^{(0)} = {}^tS_w$, and ${}^{t+\Delta t}S^{(0)} = {}^tS$. Also, for n=1, ${}^{t+\Delta t}\sigma_{ij}^{(0)} = {}^t\sigma_{ij}$.

The material point vector is updated as

$$ {}^{t+\Delta t}x_i^{(n)} = {}^{t+\Delta t}x_i^{(n-1)} + \Delta u_i^{(n)}; \quad {}^{t+\Delta t}x_i^{(0)} = {}^{t}x_i. \tag{2.9} $$

The structural density and the Cauchy stress tensor should be updated during iterations using the following relations:

$$ {}^{t+\Delta t}\rho_s^{(n)} = \frac{{}^{t+\Delta t}\rho_s^{(n-1)}}{\det\left(\Delta^{t+\Delta t}F_{ij}^{(n)}\right)} \qquad \text{for the structural density,} $$

$$ {}^{t+\Delta t}\sigma_{ij}^{(n)} = \frac{{}^{t+\Delta t}\rho_s^{(n)}}{{}^{t+\Delta t}\rho_s^{(n-1)}} \Delta^{t+\Delta t}F_{ik}^{(n)}\,{}^{t+\Delta t}S_{kl}^{(n)}\,\Delta^{t+\Delta t}F_{jl}^{(n)} \quad \text{for the Cauchy stress tensor,} \tag{2.10} $$

where $\Delta^{t+\Delta t}F_{ij}^{(n)}$ and ${}^{t+\Delta t}S_{ij}^{(n)}$ are the deformation gradient and the second Piola-Kirchhoff stress tensors at the iteration n.

The second Piola-Kirchhoff stress tensor ${}^{t+\Delta t}S_{ij}^{(n)}$ is obtained through the following relation:

$$ {}^{t+\Delta t}S_{ij}^{(n)} = {}^{t+\Delta t}\sigma_{ij}^{(n-1)} + \Delta S_{ij}^{(n)}; \quad \text{with} \quad \Delta S_{ij}^{(n)} = C_{ijrs}\Delta e_{rs}^{(n)}, \tag{2.11} $$

where $\Delta S_{ij}^{(n)}$ and $\Delta e_{rs}^{(n)}$ are the second Piola-Kirchhoff stress increment tensor and the linear part of the Green-Lagrange strain increment tensor, respectively.

2.3 Finite element discretization

In this section, we discretize the incremental equilibrium equation using the standard finite element procedure. In addition, the incremental equation for rigid floating structures is derived by introducing the generalized coordinates.

2.3.1 General flexible body hydrostatics

In the iteration n, for the finite element (e), the increment of the structural displacement $\Delta u_i^{(n)}$ is approximated as,

$$\Delta \mathbf{u}^{(n)(e)} = {}^{t+\Delta t}\mathbf{H}^{(n)(e)} \Delta \mathbf{U}^{(n)}, \tag{2.12}$$

where $\Delta \mathbf{U}^{(n)}$ is the nodal incremental displacement vector and $\mathbf{H}$ is the displacement interpolation matrix used in the finite element method. The same interpolation matrix is also used for the virtual displacement.

Substituting Equation 2.12 into Equation 2.8 and applying the standard finite element assemblage process, the following incremental equation in matrix form is obtained:

$$\left[{}^{t+\Delta t}\mathbf{K}_L^{(n)} + {}^{t+\Delta t}\mathbf{K}_{NL}^{(n-1)} - {}^{t+\Delta t}\mathbf{K}_{HD}^{(n)} - {}^{t+\Delta t}\mathbf{K}_{HN}^{(n)}\right] \Delta \mathbf{U}^{(n)}$$

$$= -{}^{t+\Delta t}\mathbf{R}_B^{(n-1)} - {}^{t+\Delta t}\mathbf{R}_I^{(n-1)} + {}^{t+\Delta t}\mathbf{R}_{HS}^{(n-1)} + {}^{t+\Delta t}\mathbf{R}_S^{(n-1)} \tag{2.13}$$

where the matrices are evaluated by

$$
\begin{aligned}
{}^{t+\Delta t}\mathbf{K}_L^{(n)} &= \sum_e \int_{{}^{t+\Delta t}V^{(n-1)(e)}} {}^{t+\Delta t}\mathbf{B}_L^{T(n)(e)}\ \mathbf{C}^{(e)}\ {}^{t+\Delta t}\mathbf{B}_L^{(n)(e)} \mathrm{d}^{t+\Delta t}V, \\
{}^{t+\Delta t}\mathbf{K}_{NL}^{(n-1)} &= \sum_e \int_{{}^{t+\Delta t}V^{(n-1)(e)}} {}^{t+\Delta t}\mathbf{B}_{NL}^{T(n)(e)}\ {}^{t+\Delta t}\boldsymbol{\sigma}^{(n-1)(e)}\ {}^{t+\Delta t}\mathbf{B}_{NL}^{(n)(e)} \mathrm{d}^{t+\Delta t}V, \\
{}^{t+\Delta t}\mathbf{K}_{HD}^{(n)} &= \sum_e \int_{{}^{t+\Delta t}S_w^{(n-1)(e)}} \rho_w g\, {}^{t+\Delta t}\mathbf{H}^{T(n)(e)}\ {}^{t+\Delta t}\mathbf{n}^{(n-1)(e)}\ {}^{t+\Delta t}\mathbf{H}_3^{(n)(e)} \mathrm{d}^{t+\Delta t}S, \\
{}^{t+\Delta t}\mathbf{K}_{HN}^{(n)} &= \sum_e \int_{{}^{t+\Delta t}S_w^{(n-1)(e)}} \rho_w g\, {}^{t+\Delta t}x_3^{(n-1)}\ {}^{t+\Delta t}\mathbf{H}^{T(n)(e)}\ {}^{t+\Delta t}\mathbf{Q}_N^{(n-1)(e)}\ {}^{t+\Delta t}\mathbf{H}^{(n)(e)} \mathrm{d}^{t+\Delta t}S, \\
{}^{t+\Delta t}\mathbf{R}_B^{(n-1)} &= \sum_e \int_{{}^{t+\Delta t}V^{(n-1)(e)}} {}^{t+\Delta t}\rho_s^{(n-1)(e)}\ g\ {}^{t+\Delta t}\mathbf{H}_3^{T(n)(e)} \mathrm{d}^{t+\Delta t}V, \\
{}^{t+\Delta t}\mathbf{R}_I^{(n-1)} &= \sum_e \int_{{}^{t+\Delta t}V^{(n-1)(e)}} {}^{t+\Delta t}\mathbf{B}_L^{T(n)(e)}\ {}^{t+\Delta t}\hat{\boldsymbol{\sigma}}^{(n-1)(e)}\ \mathrm{d}^{t+\Delta t}V, \\
{}^{t+\Delta t}\mathbf{R}_{HS}^{(n-1)} &= \sum_e \int_{{}^{t+\Delta t}S_w^{(n-1)(e)}} \rho_w g\, {}^{t+\Delta t}x_3^{(n-1)}\ {}^{t+\Delta t}\mathbf{H}^{T(n)(e)}\ {}^{t+\Delta t}\mathbf{n}^{(n-1)(e)}\ \mathrm{d}^{t+\Delta t}S, \\
{}^{t+\Delta t}\mathbf{R}_S^{(n-1)} &= \sum_e \int_{{}^{t+\Delta t}S^{(n-1)(e)}} {}^{t+\Delta t}\mathbf{H}^{T(n)(e)}\ {}^{t+\Delta t}\mathbf{f}^{s(e)}\ {}^{t+\Delta t}\mathbf{n}^{(n-1)(e)}\ \mathrm{d}^{t+\Delta t}S,
\end{aligned} \tag{2.14}
$$

where $\mathbf{C}$ is the stress-strain law matrix, $\mathbf{B}_L$ is the linear strain-displacement relation matrix, $\mathbf{B}_{NL}$ is the nonlinear strain-displacement relation matrix, $\mathbf{H}_3$ is the interpolation matrix for the component Δu_3, and $\hat{\boldsymbol{\sigma}}$ is the vector form of the Cauchy stress tensor σ_{ij}. The matrix ${}^{t+\Delta t}\mathbf{Q}_N^{(n-1)(e)}$ is defined by

$$
{}^{t+\Delta t}\mathbf{Q}_N^{(n-1)(e)} = \delta_{ik}\, {}^{t+\Delta t}x_k^{(n-1)} \frac{\partial}{\partial^{t+\Delta t}x_j^{(n-1)}} - {}^{t+\Delta t}x_k^{(n-1)} \frac{\partial}{\partial^{t+\Delta t}x_i^{(n-1)}} \left(\mathbf{e}_i \otimes \mathbf{e}_j\right), \tag{2.15}
$$

Note that the matrix $\left[{}^{t+\Delta t}\mathbf{K}_L^{(n)} + {}^{t+\Delta t}\mathbf{K}_{NL}^{(n-1)} - {}^{t+\Delta t}\mathbf{K}_{HD}^{(n)} - {}^{t+\Delta t}\mathbf{K}_{HN}^{(n)}\right]$ in Equation 2.13 is a singular matrix, because there is no stiffness for the rigid translational motion in the x_1- and x_2- directions. Therefore, a proper boundary condition is required for the directions.

Equation 2.13 should be iterated until the linearization error satisfies the following criteria:

$$\left\| \frac{\Delta\mathbf{u}^{T(n)} \cdot (-{}^{t+\Delta t}\mathbf{R}_B^{(n-1)} - {}^{t+\Delta t}\mathbf{R}_I^{(n-1)} + {}^{t+\Delta t}\mathbf{R}_{HS}^{(n-1)} + {}^{t+\Delta t}\mathbf{R}_S^{(n-1)})}{\Delta\mathbf{u}^{T(1)} \cdot (-{}^{t+\Delta t}\mathbf{R}_B^{(0)} - {}^{t+\Delta t}\mathbf{R}_I^{(0)} + {}^{t+\Delta t}\mathbf{R}_{HS}^{(0)} + {}^{t+\Delta t}\mathbf{R}_S^{(0)})} \right\|_2 \leq \varepsilon_E \tag{2.16}$$

where ε_E is an energy criterion in the iterative solution procedure.

2.3.2 Rigid body hydrostatics

In this section, we derive equations for the nonlinear hydrostatic analysis of rigid floating structures. The equations for the rigid body hydrostatic analysis can be derived by modifying the Equation 2.6. Basically, in the rigid body case, the linear strain tensor e_{ij} in Equation 2.6 is no longer valid. Therefore, the first and sixth terms in Equation 2.6 are equal to zero.

In addition, using Equation 2.3, we modify the second term in Equation 2.6 as follows, see Reference [10]:

$$\int_{^tV} {}^t\sigma_{ij}\delta^{t+\Delta t}{}_t\eta_{ij}\mathrm{d}^tV = \int_{^tS_w} \rho_w g\ {}^tx_3{}^tn_i \frac{\partial^{t+\Delta t}{}_t u_k}{\partial^t x_i}\delta u_k \mathrm{d}^tS - \int_{^tV} {}^t\rho_s g\ \frac{\partial^{t+\Delta t}{}_t u_k}{\partial^t x_3}\delta u_k \mathrm{d}^tV. \tag{2.17}$$

Substituting Equation 2.17 into Equation 2.6 and applying the usual finite element assemblage process, we obtain the following incremental equation for the rigid body hydrostatic analysis:

$$\left[\boldsymbol{\Psi}^{RT}\left({}^{t+\Delta t}\mathbf{K}_L^{(n)} + {}^{t+\Delta t}\mathbf{K}_{NL}^{(n-1)} - {}^{t+\Delta t}\mathbf{K}_{HD}^{(n)} - {}^{t+\Delta t}\mathbf{K}_{HN}^{(n)}\right)\boldsymbol{\Psi}^R\right]\Delta\mathbf{q}^{R(n)}$$

$$= -{}^{t+\Delta t}\mathbf{R}_B^{(n-1)} + {}^{t+\Delta t}\mathbf{R}_{HS}^{(n-1)} + {}^{t+\Delta t}\mathbf{R}_S^{(n-1)} \tag{2.18}$$

where

$${}^{t+\Delta t}\mathbf{K}_{HS}^{(n)} = \sum_e \int_{^{t+\Delta t}S_w^{(n-1)(e)}} \rho_w g^{t+\Delta t}x_3^{(n-1)}\ {}^{t+\Delta t}\mathbf{H}^{T(n)(e)} \frac{\partial \mathbf{H}^{(n)(e)}}{\partial^{t+\Delta t}x_i^{(n-1)}}{}^{t+\Delta t}\mathbf{n}^{(n-1)(e)}\ \mathrm{d}^{t+\Delta t}S,$$

$${}^{t+\Delta t}\mathbf{K}_{HB}^{(n)} = \sum_e \int_{^{t+\Delta t}V^{(n-1)(e)}} {}^{t+\Delta t}\rho_s^{(n-1)(e)}\ g^{t+\Delta t}\mathbf{H}^{T(n)(e)} \frac{\partial \mathbf{H}^{(n)(e)}}{\partial^{t+\Delta t}x_3^{(n-1)}}{}^{t+\Delta t}\mathbf{n}^{(n-1)(e)}\mathrm{d}^{t+\Delta t}V, \tag{2.19}$$

and

$$\mathbf{u}^R = \mathbf{\Psi}^R \mathbf{q}^R = q_1^R \mathbf{\Psi}_1^R + \cdots + q_6^R \mathbf{\Psi}_6^R \tag{2.20}$$

in which $\mathbf{\Psi}_i^R (i = 1, 2, ...6)$ is the nodal displacement vector for the i-th rigid body mode, and the displacement vector ($\mathbf{u}^R$) of six rigid body motions (surge (R_1), sway (R_2), heave (R_3), roll (R_4), pitch (R_5), and yaw (R_6)) can be constructed about the origin of the Cartesian coordinate system as follows:

$$u_i^{R_1} = q_1^R \delta_{1i}, \quad u_i^{R_2} = q_2^R \delta_{2i}, \quad u_i^{R_3} = q_3^R \delta_{3i}, \quad u_i^{R_4} = q_4^R \varepsilon_{ijk} \delta_{1j} {}^0x_k,$$

$$u_i^{R_5} = q_5^R \varepsilon_{ijk} \delta_{2j} {}^0x_k, \quad u_i^{R_6} = q_6^R \varepsilon_{ijk} \delta_{3j} {}^0x_k; \quad i, j, k = 1, 2, 3 \text{ and } \varepsilon_{ijk} = \text{permutation symbol.} \tag{2.21}$$

Equation 2.18 should be iterated until the error due to linearization satisfies the following criterion:

$$\left\| \frac{\Delta \mathbf{q}^{R(n)} \cdot (-{}^{t+\Delta t}\mathbf{R}_B^{(n-1)} + {}^{t+\Delta t}\mathbf{R}_{HS}^{(n-1)} + {}^{t+\Delta t}\mathbf{R}_S^{(n-1)})}{\Delta \mathbf{q}^{R(1)} \cdot (-{}^{t+\Delta t}\mathbf{R}_B^{(0)} + {}^{t+\Delta t}\mathbf{R}_{HS}^{(0)} + {}^{t+\Delta t}\mathbf{R}_S^{(0)})} \right\|_2 \leq \varepsilon_E \tag{2.22}$$

If Equation 2.22 is satisfied, we can obtain the hydrostatic equilibrium of rigid floating bodies. In other words, the body force $\mathbf{R}_B$, the buoyancy force $\mathbf{R}_{HS}$, and the surface force $\mathbf{R}_S$ are in equilibrium. Note that it is not necessary to consider the update procedure of the structural density in Equation 2.10 because the density of the floating body does not change.

2.4 Numerical integration

Numerical integration is essential to evaluate stiffness matrices and load vectors in the finite element formulation derived in the previous sections. In this section, we develop a special numerical integration technique to effectively consider the non-matching mesh problem in a nonlinear hydrostatic finite element analysis of floating structures. In particular, the integration technique is applied to the surface integration of partially submerged finite elements, whereas the conventional Gaussian quadrature scheme is used for the surface and volume integrations of non- or fully submerged finite elements.

When the floating structure experiences large motions, the wet-surface changes significantly. The structural mesh then does not match with the free-surface of water in general. When the mesh matches with the free-surface well, as depicted in Figure 2.3(a), it is easy to discretize the structural wet and dry surfaces by locating all wet nodes at the free surface. As shown in Figure 2.3(a), when the mesh and free-surface are not matched, the numerical integration should be carefully performed. For example, the mesh can be reconstructed using a re-meshing technique, which is computationally expensive and complicated.

To handle the non-matching mesh problem without modifying the initial mesh, an effective numerical integration technique is developed, as shown in Figure 2.4. We consider four different cases of wetted situations of 4-node finite elements. CASE 1 is a fully wetted element case whereas others are partially wetted element cases. In the following, we explain the numerical integration strategies in detail.

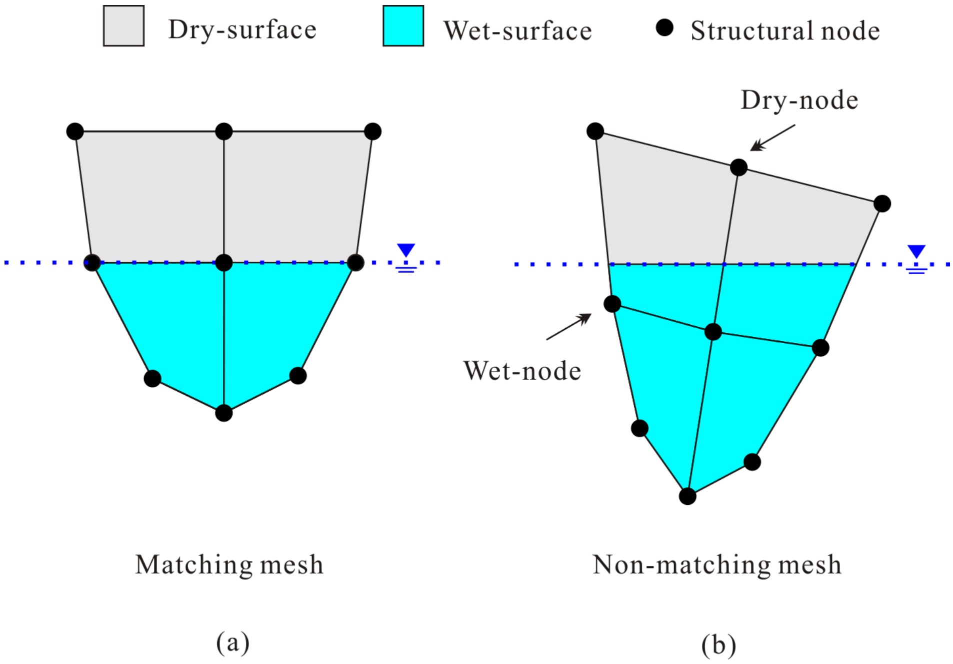

Figure 2.3: Wet-surface change of finite element meshes: (a) Matching mesh and (b) non-matching mesh.

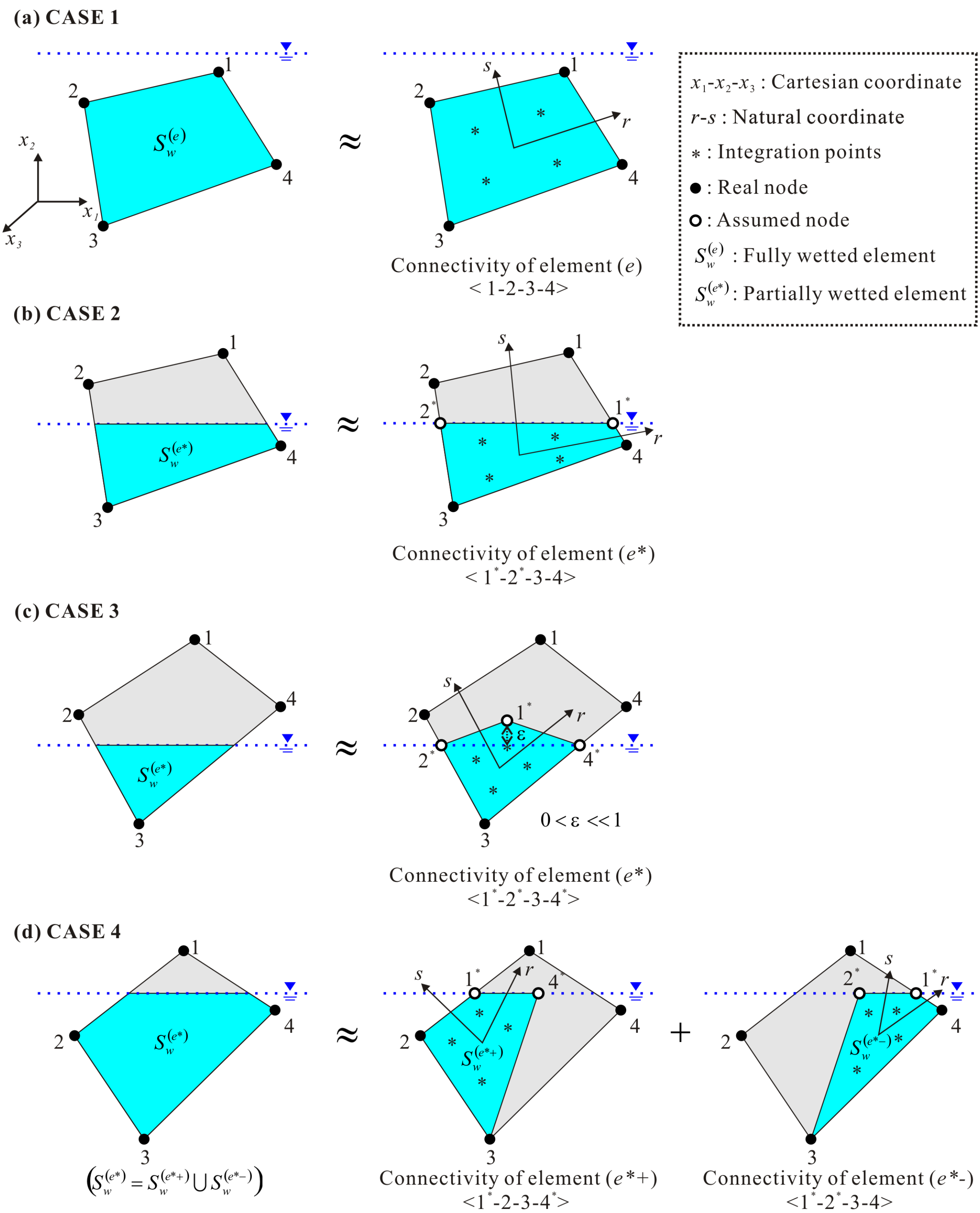

Figure 2.4: Numerical integration strategies for a 4-node wet-element.

- CASE 1 (all nodes are submerged): As depicted in Figure 2.4(a), the fully wetted element connected by nodes 1-2-3-4 can be numerically integrated over the wet surface S_w^e using the conventional 2×2 Gaussian quadrature technique in natural coordinates.

- CASE 2 (2 of 4 nodes are submerged): Figure 2.4(b) shows a partially wetted element case, in which two of four nodes are submerged under the free surface. The wetted part of the element connected by nodes 1-2-3-4 is defined as 1^*-2^*-3-4 by introducing the assumed nodes 1^* and 2^* at the free surface. The assumed nodes 1^* and 2^* are used only for numerical integration. That is, there is no increase in DOFs in the hydrostatic analysis. Using the new elemental connectivity, we can integrate the wetted surface $S_w^{(e^*)}$ through the conventional 2×2 Gaussian quadrature.

- CASE 3 (1 of 4 nodes are submerged): One of four nodes is submerged under the free surface. In this case, the connectivity of the wetted part is defined as 1^*-2^*-3-4^* by introducing the assumed nodes 1^*, 2^*, and 4^*, as shown in Figure 2.4(c). The assumed nodes 1^* and 4^* are exactly located at the free surface and node 1^* is placed slightly higher ($0 < \varepsilon \ll 1$) than the free surface to avoid the geometric singularity of the 4-node finite element.

- CASE 4 (3 of 4 nodes are submerged): As shown in Figure 2.4(d), we consider the case in which three of four nodes are submerged. We here subdivide the pentagon-shape wetted part into two rectangular subparts $\left(S_w^{(e^*)} = S_w^{(e^{*+})} \cup_w^{(e^{*-})}\right)$. The connectivity of the two parts is defined as 1^*-2-3-4^* and 1^*-2^*-3-4, respectively. In this case, the terms $\mathbf{K}_{HD}$, $\mathbf{K}_{HN}$, and $\mathbf{R}_{HS}$ in Equation 2.13 and the term $\mathbf{K}_{HS}$ in Equation 2.18, can be integrated over the wet-surfaces (e^*) as follows:

$$
\begin{aligned}
\mathbf{K}_{HD}^{(e)} \approx& \mathbf{K}_{HD}^{(e^*)} \\
=& \int_{S_w^{(e^+)}} \rho_w g \mathbf{H}^{T(e^{*+})}\ \mathbf{n}^{(e^{*+})}\ \mathbf{H}_3^{(e^{*+})} \mathrm{d}S + \int_{S_w^{(e^-)}} \rho_w g \mathbf{H}^{T(e^{*-})}\ \mathbf{n}^{(e^{*-})}\ \mathbf{H}_3^{(e^{*-})} \mathrm{d}S,
\end{aligned}
$$

$$
\begin{aligned}
\mathbf{K}_{HN}^{(e)} \approx& \mathbf{K}_{HN}^{(e^*)} \\
=& \int_{S_w^{(e^{*+})}} \rho_w g x_3\ \mathbf{H}^{T(e^{*+})}\ \mathbf{Q}_N^{(e^{*+})}\ \mathbf{H}^{(e^{*+})} \mathrm{d}S + \int_{S_w^{(e^{*-})}} \rho_w g x_3\ \mathbf{H}^{T(e^{*-})}\ \mathbf{Q}_N^{(e^{*-})}\ \mathbf{H}^{(e^{*-})} \mathrm{d}S,
\end{aligned}
$$

$$
\begin{aligned}
\mathbf{R}_{HS}^{(e)} \approx& \mathbf{R}_{HS}^{(e^*)} \\
=& \int_{S_w^{(e^{*+})}} \rho_w g x_3\ \mathbf{H}^{T(e^{*+})}\ \mathbf{n}^{(e^{*+})}\ \mathrm{d}S, + \int_{S_w^{(e^{*-})}} \rho_w g x_3\ \mathbf{H}^{T(e^{*-})}\ \mathbf{n}^{(e^{*-})}\ \mathrm{d}S,
\end{aligned}
$$

$$
\begin{aligned}
\mathbf{K}_{HS}^{(e)} \approx& \mathbf{K}_{HS}^{(e^*)} \\
=& \int_{S_w^{(e^{*+})}} \rho_w g x_3\ \mathbf{H}^{T(e^{*+})} \frac{\partial \mathbf{H}^{(e^{*+})}}{\partial x_i} \mathbf{n}^{(e^{*+})}\ \mathrm{d}S + \int_{S_w^{(e^{*-})}} \rho_w g x_3\ \mathbf{H}^{T(e^{*-})} \frac{\partial \mathbf{H}^{(e^{*-})}}{\partial x_i} \mathbf{n}^{(e^{*-})}\ \mathrm{d}S.
\end{aligned} \tag{2.23}
$$

Here, the numerical integration procedure is explained for 4-node rectangular elements. The situations of partially submerged 3-node elements also can be easily considered through a similar numerical integration scheme. Finally, Equation 2.13 for elastic bodies and Equation 2.18 for rigid bodies are iteratively solved without adjustment of the initial finite element mesh. This means that a re-meshing scheme is not required in the present nonlinear hydrostatic analysis of floating structures.

2.5 Numerical examples

In this section, several numerical tests are performed to validate the proposed numerical method and to demonstrate its capabilities through various nonlinear hydrostatic problems.

A freely floating box barge is considered to obtain hydrostatic equilibrium states in both flexible and rigid body cases. The usual hydrostatic stability curve is evaluated and compared with the ORCA 3D [31] in the rigid body case. In addition, the importance of a nonlinear hydrostatic analysis in the stress analysis of flexible floating structures is demonstrated.

We then perform a nonlinear hydrostatic analysis of a flexible cargo barge in freely floating and grounded cases. Various results including center of gravity (COG), center of buoyancy (COB), buoyancy, total weight of the floating structure, displaced volume, and strain energy are presented and the stress distributions are plotted. In the following, the parameter ε in CASE 3 of Section 4 is set to 1.0×10^{-8} for the numerical integrations.

2.5.1 Freely floating rigid box barge

A box barge of length 200m, width 100m, and height 60m is considered; see Figure 2.5. The barge consists of three parts: the bottom, side hulls (bow, stern, starboard and port), and the top deck. The geometric and material properties are listed in Table 2.1, and it is ensured that the draft d is 40m with a vertical center of gravity (COG) -4.3m, vertical center of buoyancy -20.0m, and displaced volume 80,000m^3 in the rigid body case. The density of water ρ_w is $1000kg/m^3$ and the gravitational acceleration g is $9.8m/s^2$. The barge model is discretized using 4-node MITC (Mixed Interpolation of Tensorial Components) shell finite elements [27, 28, 29, 30]; see Figure 2.5(b).

In Figure 2.6(a), the box barge is initially positioned in the water with a trim angle of 20 degrees. The initial configuration does not correspond to the hydrostatic equilibrium. An incremental rigid body hydrostatic analysis is performed using Equation 2.18 until Equation 2.22 is satisfied ($\varepsilon = 1.0 \times 10^{-8}$). As shown in Figure 2.6(c), the hydrostatic equilibrium is found after 5 iterations and the details of incremental solutions are listed in Table 2.2. In the hydrostatic equilibrium, the buoyancy ($7.840 \times 10^9 N$) is balanced with the self-weight of the floating structure. In addition, the numerical results quickly converge to the analytical results.

The proposed formulation also can be used to calculate hydrostatic stability curves (GZ-curves). Figure 2.7 shows the GZ-curves of the box barge for the transverse and longitudinal directions. There is good agreement between the results of the proposed formulation and those obtained using ORCA 3D [31].

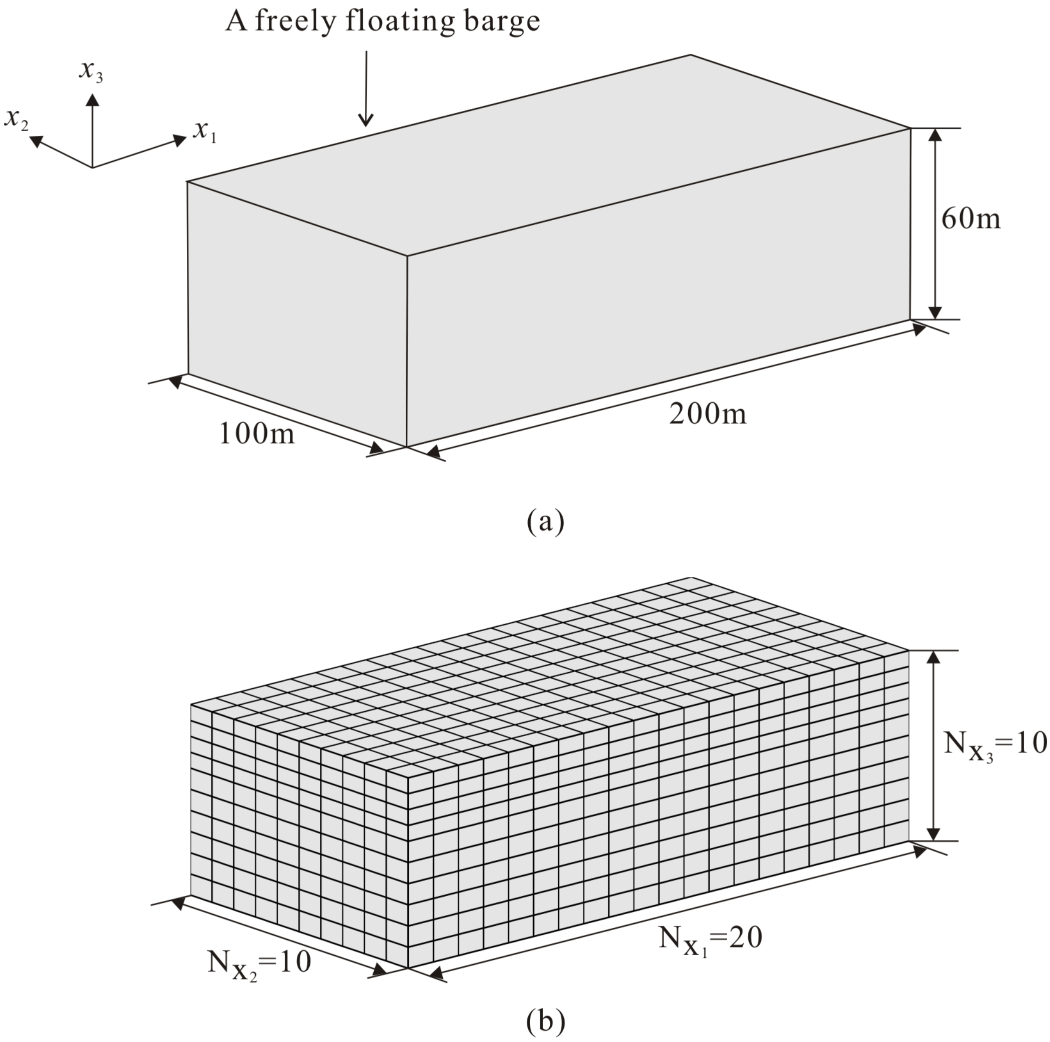

Figure 2.5: A box barge: (a) dimensions and (b) finite element mesh.

Table 2.1: Material properties of box barge. (*For simplicity, the density of the bottom hull is set to zero.)

	Bottom	Top	Sides
Thickness (m)	0.4	0.2	0.2
Density (kg/m^3)	0^*	3.8×10^4	9.0×10^4
Young's modulus (Pa)	2.0×10^{13}	2.0×10^{13}	1.0×10^{12}
Poisson's ratio	0.3	0.3	0.3

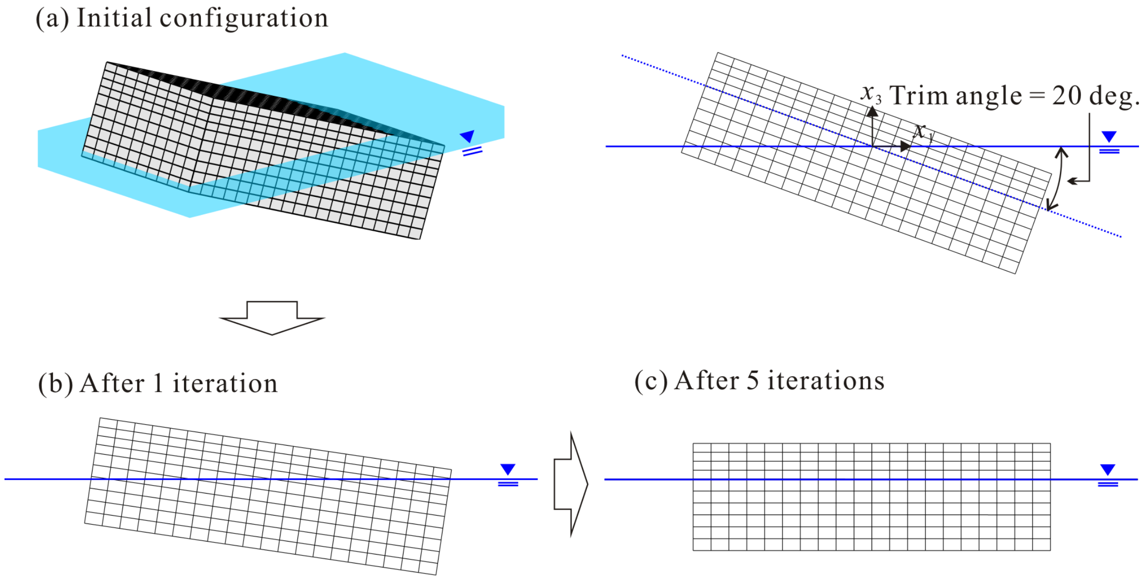

Figure 2.6: Hydrostatic analysis of the rigid box barge: (a) initial configuration, (b) instantaneous configuration (after 1 iteration), and (c) configuration for hydrostatic equilibrium (after 5 iterations).

Table 2.2: Incremental solutions for hydrostatic analysis of the rigid box barge.

Iteration	Buoyancy (N)	COG (m) (x_1^g, x_2^g, x_3^g)	COB (m) (x_1^b, x_2^b, x_3^b)	Energy criteria (ε_E)
1	7.779×10^{9}	(-0.627,0,-4.254)	(9.373,0,-20.682)	-
2	7.842×10^{9}	(-0.072,0,-4.297)	(1.068,0,-20.009)	3.062×10^{-1}
3	7.841×10^{9}	(-0.010,0,-4.298)	(0.151,0,-20.001)	1.125×10^{-4}
4	7.840×10^{9}	(-0.002,0,-4.299)	(0.011,0,-20.000)	6.223×10^{-8}
5	7.840×10^{9}	(0,0,-4.300)	(0,0,-20.000)	6.436×10^{-9}
Ref.	7.840×10^{9} (Self-weight)	(0,0,-4.300)	(0,0,-20.000)	-

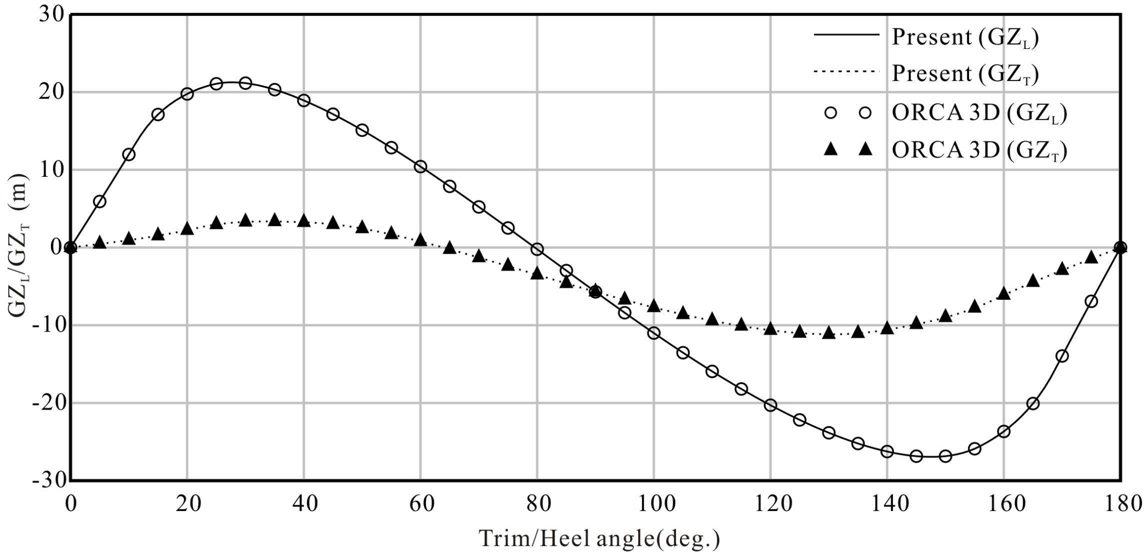

Figure 2.7: Comparison of GZ-curves.

2.5.2 Freely floating flexible box barge

In the case of a flexible body, the box barge deforms and thus the configuration in Figure 2.6(c) is no longer in equilibrium. The structural deformation causes a change of the displaced volume, resulting in a buoyancy change, while the structural self-weight does not change. A new hydrostatic equilibrium should be then found. We here start the hydrostatic analysis of the flexible box barge from the configuration obtained in the hydrostatic analysis of the rigid box barge, as shown in Figure 2.8(a). The x_1- and x_2- directional displacements are fixed at the nodal position (0, 0, -d). The convergence of the incremental hydrostatic analysis of flexible bodies highly depends on the initial configuration given.

Figure 2.8(b) presents the configuration calculated for the hydrostatic equilibrium of the flexible box barge. The details of incremental solutions are summarized in Table 2.3. We can observe that the buoyancy is varying during the iterations whereas the self-weight is not changed because the structural density is correctly updated using Equation 2.10. After 5 iterations, the buoyancy is balanced with the self-weight and the energy criterion defined in Equation 2.16 is satisfied ($\varepsilon_E = 1.0 \times 10^{-8}$).

We then demonstrate the importance of a nonlinear hydrostatic analysis in the stress analysis. In order to calculate the stress distribution of floating structures in usual engineering practice, the hydrostatic pressure is first calculated through the rigid body hydrostatic analysis. The pressure distribution is then projected into the flexible floating body as an external load, and the stress distribution is evaluated. This procedure would be adequate for relatively rigid floating structures, but results in larger errors as the structure becomes more flexible.

Using the present formulation, we can accurately calculate the stress distribution at the hydrostatic equilibrium of flexible floating structures. The distribution of von Mises stress is plotted in Figures 2.8(c) and (d), obtained after 1 iteration and 5 iterations, respectively. Note that Figure 2.8(c) is equivalent to the results of the usual stress analysis based on the rigid body hydrostatic analysis because the incremental analysis starts from the configuration for the hydrostatic equilibrium of the rigid box barge. Figure 2.8(d) is obtained at the final hydrostatic equilibrium of the flexible box barge.

It is observed that the distribution of von Mises stress is totally different between both results and the maximum value in Figure 2.8(d) is almost four times larger than that in Figure 2.8(c). Therefore, the use of a nonlinear hydrostatic analysis is recommended for the stress analysis of general flexible floating structures.

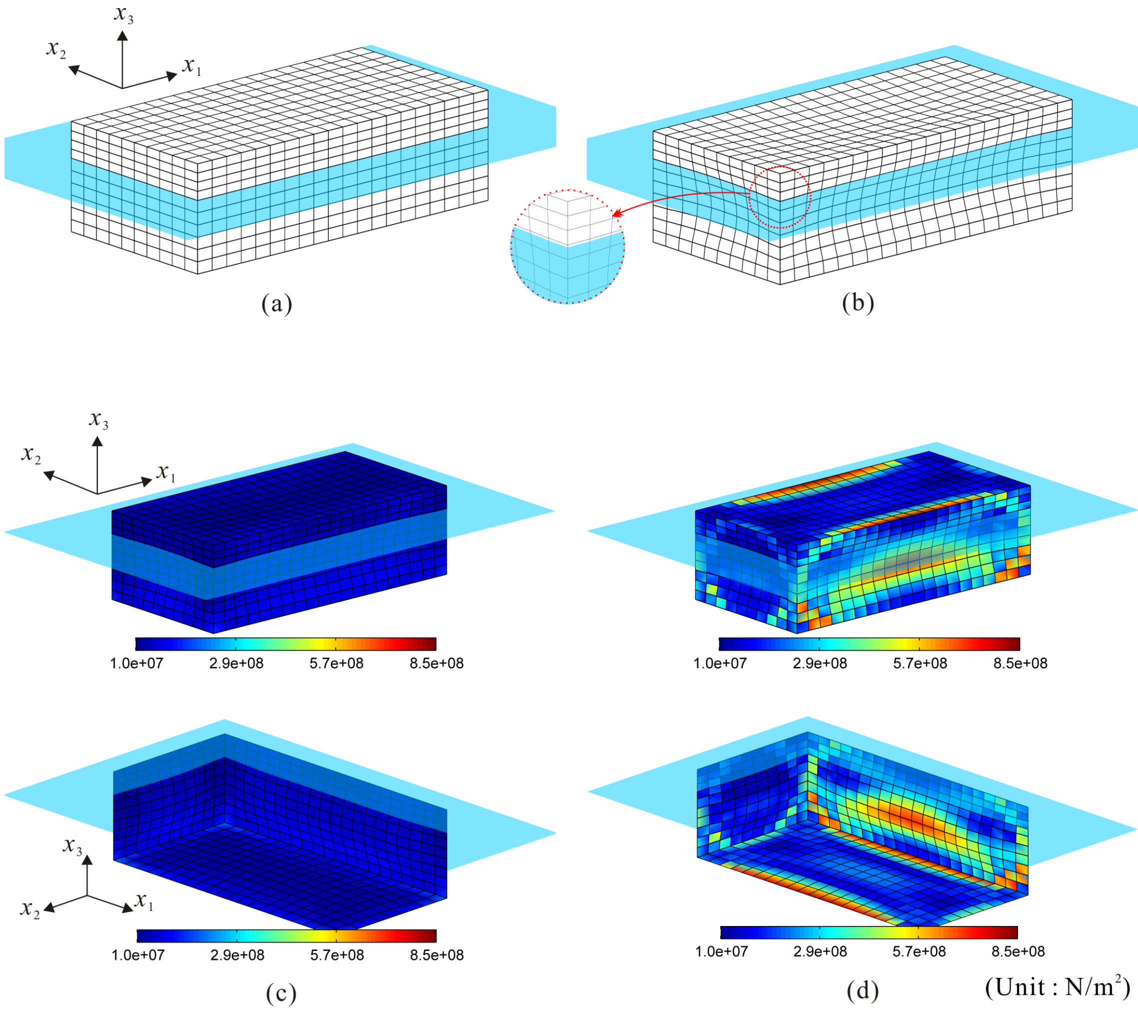

Figure 2.8: Hydrostatic analysis results of the flexible box barge: (a) initial configuration (configuration for hydrostatic equilibrium of the rigid box barge), (b) configuration for hydrostatic equilibrium (after 5 iterations), (c) distribution of von Mises stress (after 1 iteration, maximum value: 2.0328×10^8 N), and (d) distribution of von Mises stress (after 5 iterations, maximum value: 8.3839×10^8 N).

Table 2.3: Incremental solutions for hydrostatic analysis of the flexible box barge.

Iteration	Buoyancy (N)	COG (m) (x_1^g, x_2^g, x_3^g)	COB (m) (x_1^b, x_2^b, x_3^b)	Energy criteria (ε_E)
1	7.788302×10^9	(0,0,-8.7259)	(0,0,-21.774)	-
2	7.840521×10^9	(0,0,-9.4776)	(0,0,-22.052)	1.030899×10^1
3	7.840042×10^9	(0,0,-9.4669)	(0,0,-22.075)	3.382075×10^{-1}
4	7.840003×10^9	(0,0,-9.4683)	(0,0,-22.079)	1.023977×10^{-4}
5	7.840000×10^9	(0,0,-9.4682)	(0,0,-22.080)	9.436614×10^{-9}
Ref.	7.840000×10^9 (Self-weight)	-	-	-

2.5.3 Cargo barge problems

In this section, various nonlinear hydrostatic analyses are conducted for freely floating and grounded flexible cargo barge models. The cargo barge model (thickness is 1m, Poisson's ratio is 0.37, Young's modulus is $1.0{\times}10^9$ Pa, and structural density ρ_s is 2655.06 kg/m^3) is presented in Figure 2.9(a) and it is discretized with 2,300 shell finite elements, as shown in Figure 2.9(b). The "cargo hold" is the area where the surface force will be applied. The various floating and loading conditions considered here are summarized in Table 2.4 and Figure 2.10. Note that, in the freely floating cases, the x_1- and x_2-directional nodal displacements are clamped at (0, 0, -d).

We first conduct a flexible body hydrostatic analysis using a freely floating cargo barge model. The initial draft d is set to 8.0 m. The hydrostatic equilibrium of the flexible cargo barge can be obtained after 5 iterations; see Table 2.5. The corresponding configuration is depicted in Figure 2.11(a), in which local bending deformation is observed. Figure 2.11(b) presents the distribution of von Mises stress calculated.

In addition, we consider the case where the barge is subjected to cargo loading. Uniform surface force ($1.0{\times}10^5 N/m^2$) is applied on the "cargo hold" shown in Figure 2.10(b). In this case, the hydrostatic equilibrium is obtained after 6 iterations. Figure 2.12 shows the deformed configuration and the distribution of von Mises stress. In the loaded case, the buoyancy equals the sum of self-weight and external forces; see Table 2.5.

Finally, we consider two grounded situations of cargo barge, as described in Figures 2.10(c) and (d). To model these situations, we introduce the pin-support boundary condition and therefore no displacements are introduced at the nodes of grounding points. The initial draft d is set to be 6m for both cases and the corresponding initial configurations are presented in Figures 2.13(a) and (b), respectively.

On top of Figures 2.14(a) and (b), the deformed configurations of two grounded cases are presented. In these hydrostatic equilibriums, the weight of the floating structure should be equal to the sum of buoyancy and reaction force at the grounding point; see Table 2.6. The distributions of von Mises stress are presented on the bottom of Figures 2.14(a) and (b), respectively. A symmetric deformation and stress fields are obtained in grounded case-1, as shown in Figure 2.14(a). In grounded case-2, as shown in Figure 2.14(b), an asymmetric deformation including a twisting mode is observed and thus the transverse COB (x_2^b) is no longer zero.

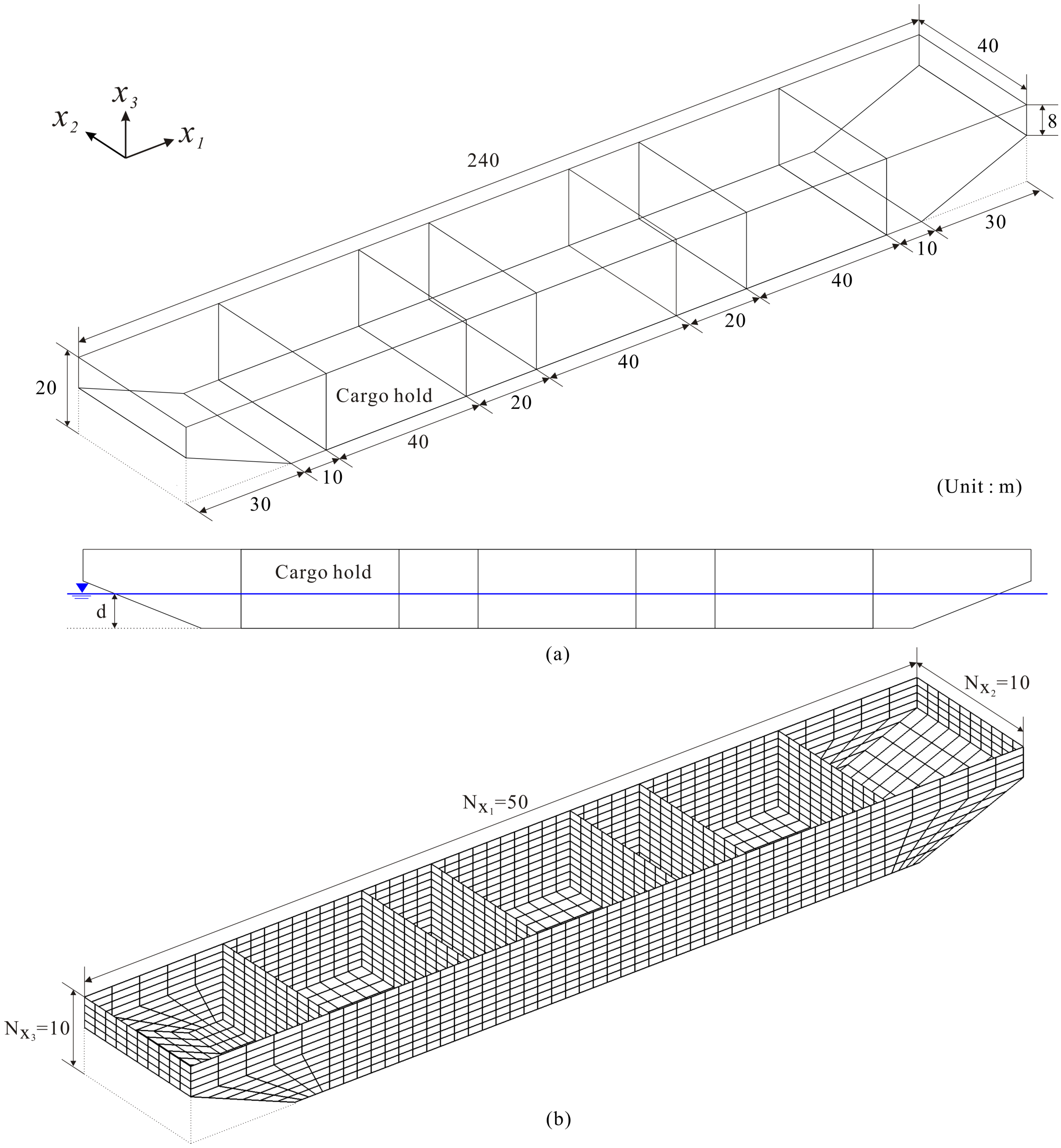

Figure 2.9: A flexible cargo barge: (a) dimensions and (b) finite element mesh used.

Table 2.4: Floating and loading conditions in the cargo barge problems.

	Initial draft (m)	Weight (N)	External force (N)/ Grounding points (m)
(a) Freely floating (w/o loading)	8.0	6.272×10^8	-
(b) Freely floating (Loaded)	8.0	6.272×10^8	Cargo hold : 1.600×10^8 N
(c) Grounded case-1	6.0	6.272×10^8	(80,0,-6)
(d) Grounded case-2	6.0	6.272×10^8	(80,-20,-6)

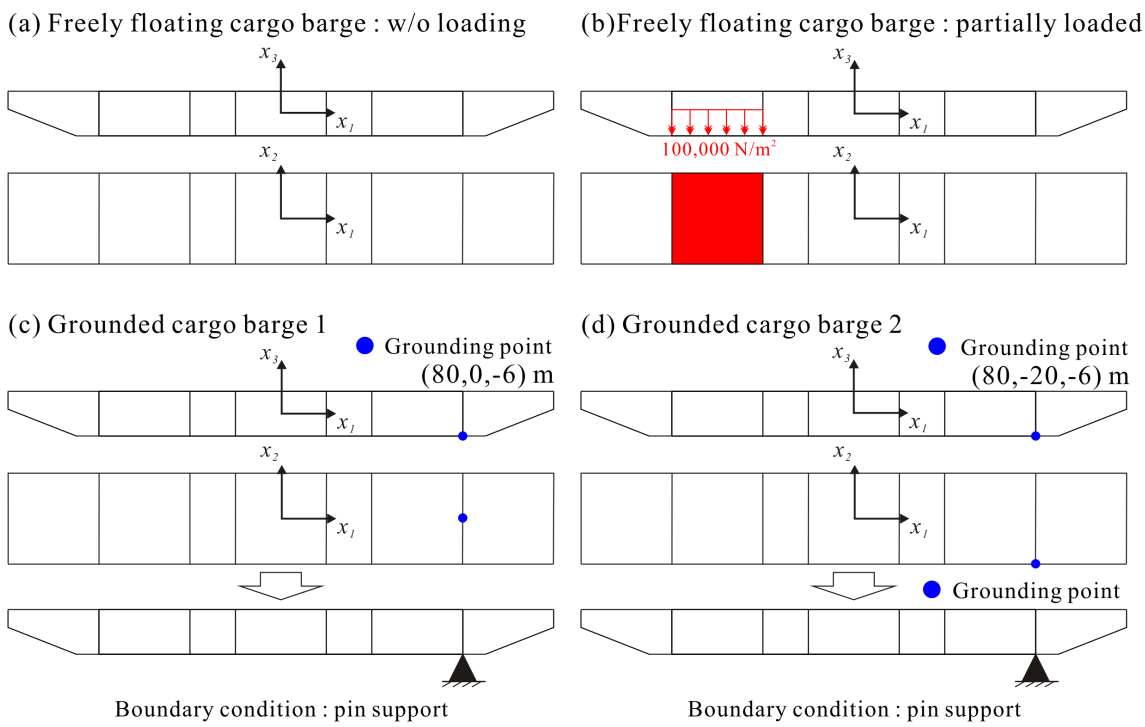

Figure 2.10: Various floating and loading conditions.

Table 2.5: Hydrostatic analysis results of the freely floating cargo barge.

Analysis condition	Freely floating (w/o loading)	Freely floating (loaded)
Number of iterations	5	6
Buoyancy (N)	6.272×10^{8}	7.872×10^{8}
Weight (N)	6.272×10^{8}	6.272×10^{8}
External force (N)	-	1.600×10^{8}
COB (x_1^b, x_2^b, x_3^b)	(0,0,-3.726)	(-12.073,0,-4.751)
Total strain energy (N·m)	3.061×10^{8}	8.700×10^{8}
Energy criteria	3.221×10^{-9}	1.889×10^{-9}

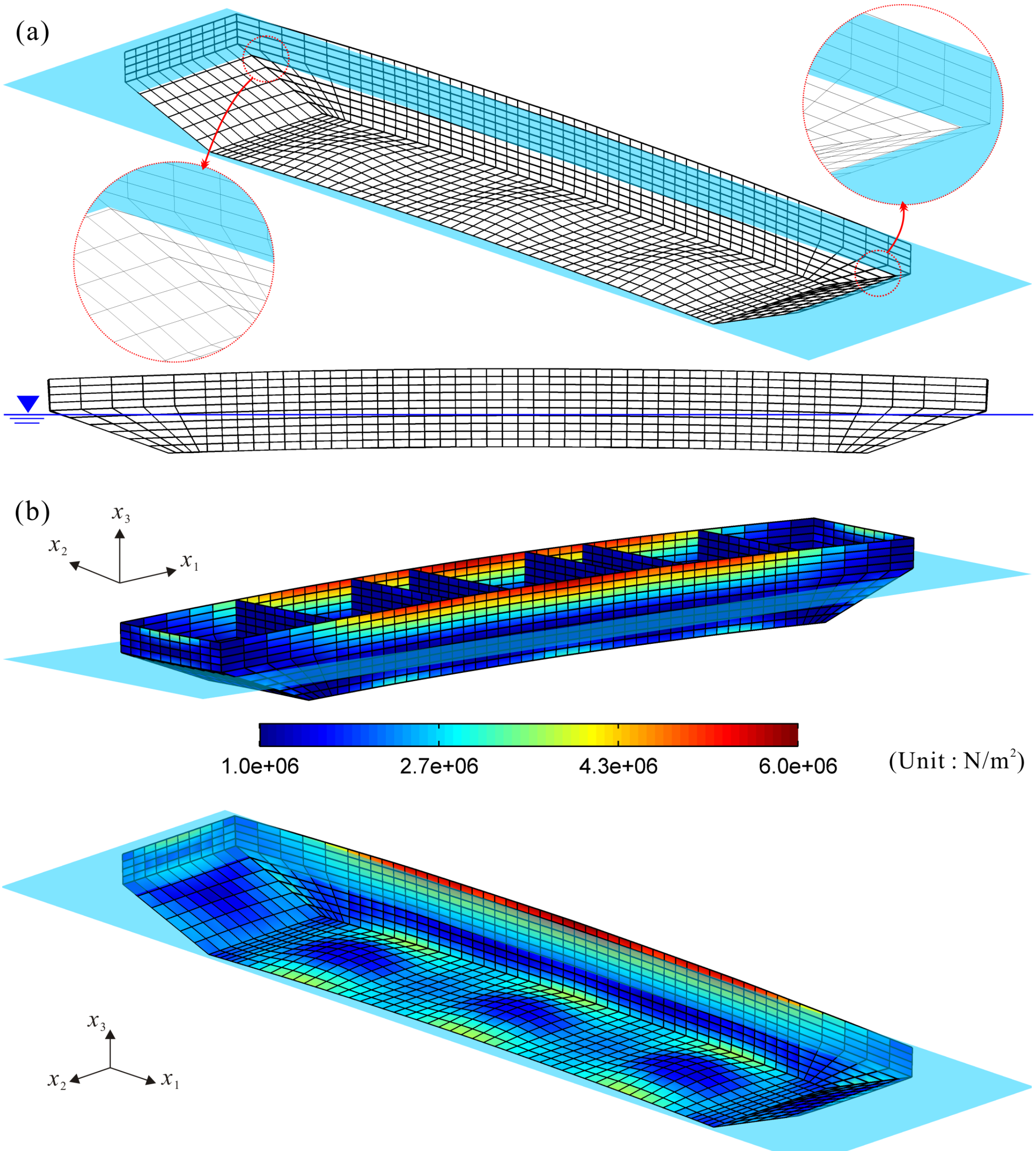

Figure 2.11: Hydrostatic analysis results of the freely floating cargo barge (w/o loading): (a) deformed configuration and (b) distribution of von Mises stress (maximum value: 5.7788×10^6 N).

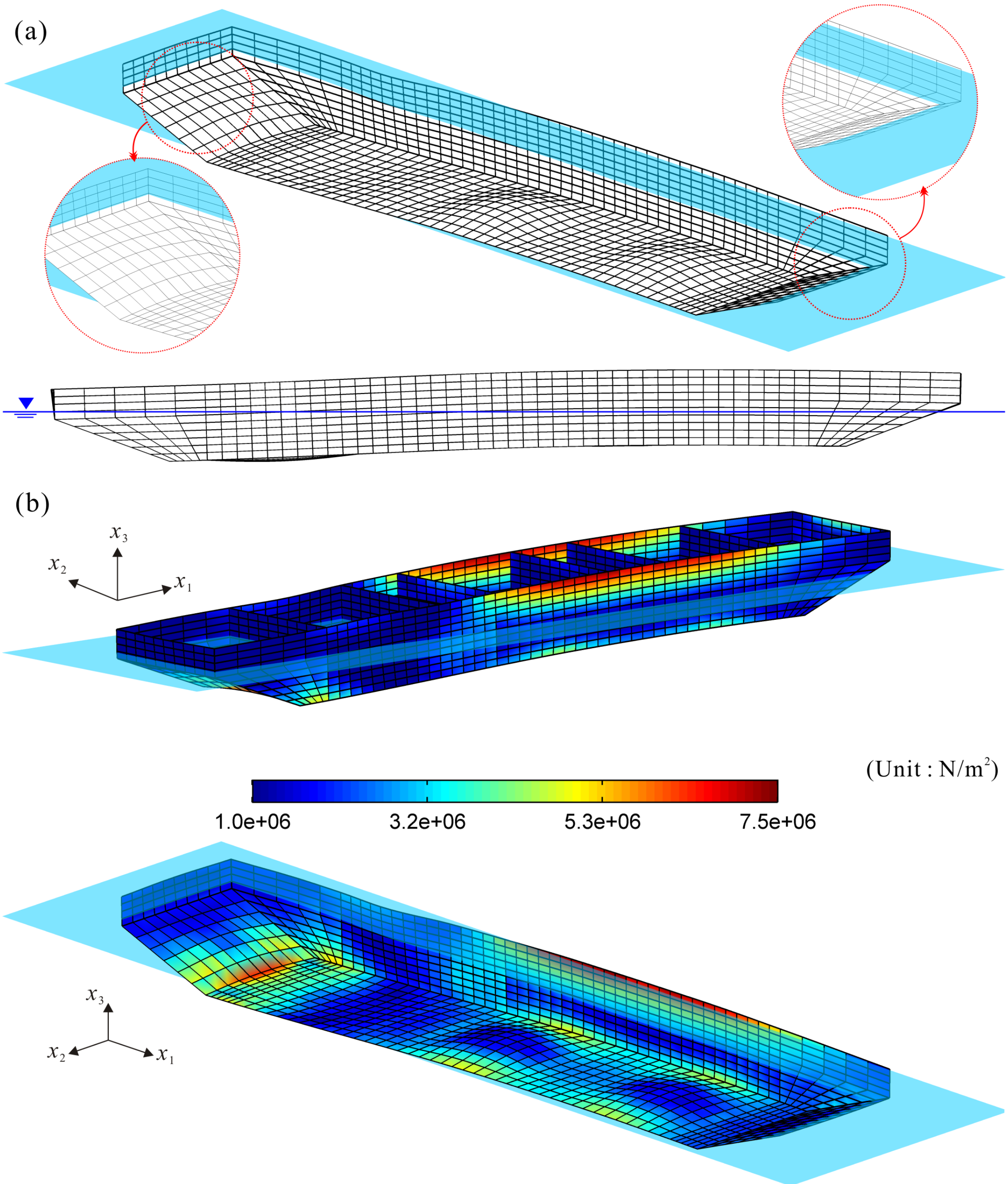

Figure 2.12: Hydrostatic analysis results of the freely floating cargo barge (loaded): (a) deformed configuration and (b) distribution of the von Mises stress (maximum value: 7.4338×10^6 N).

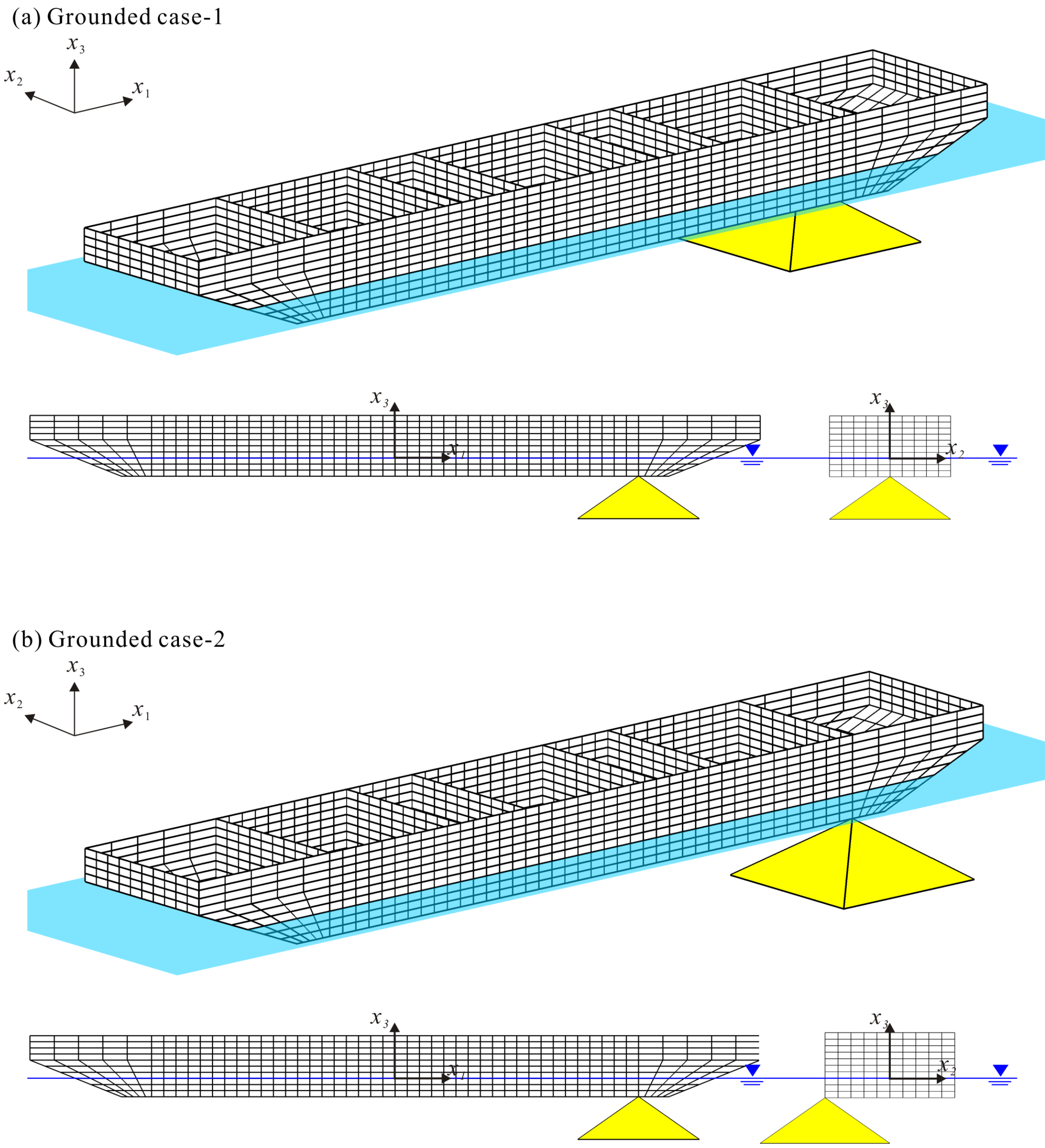

Figure 2.13: Initial configurations of grounded cargo barge: (a) grounded case-1 and (b) grounded case-2.

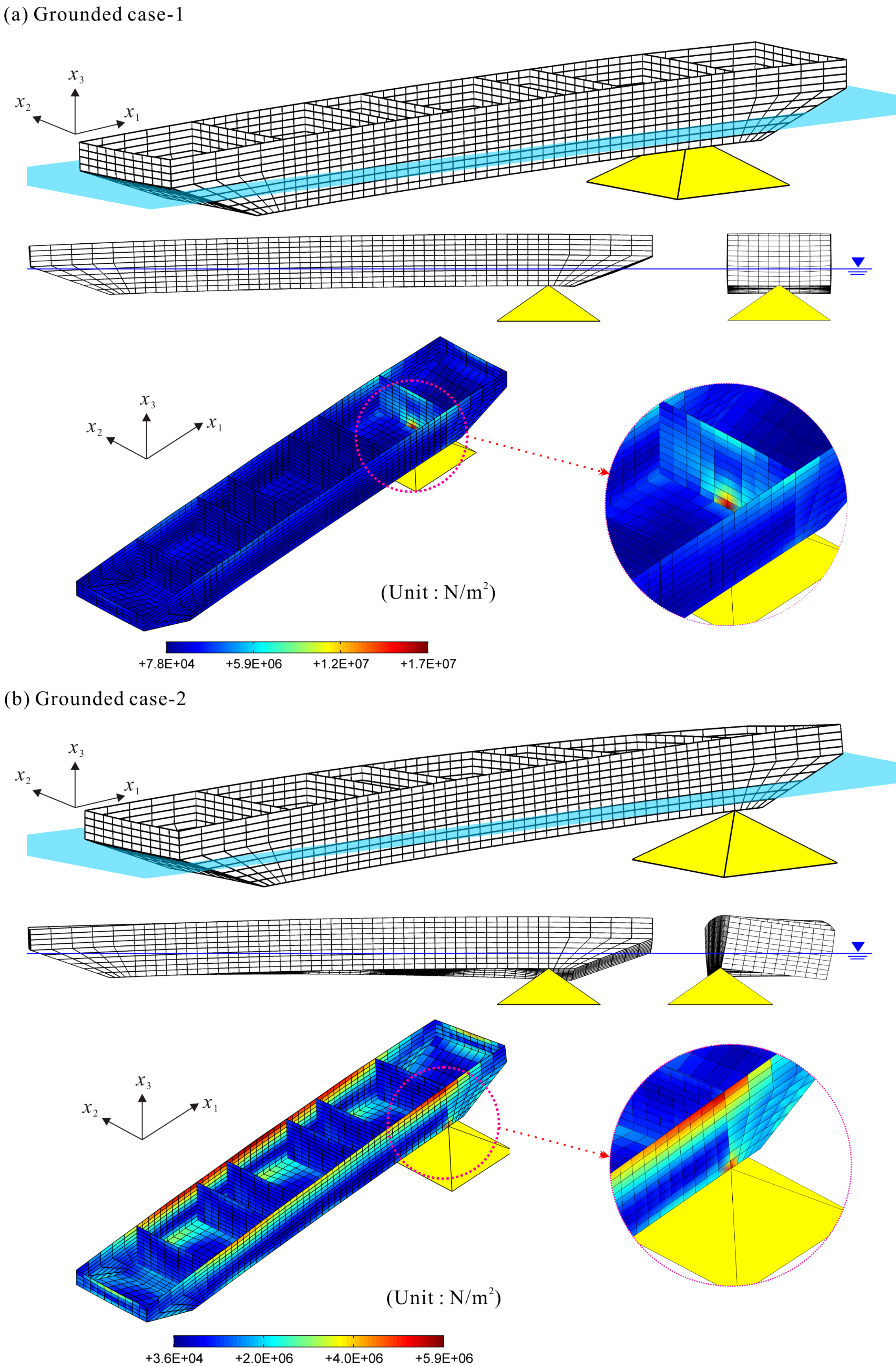

Figure 2.14: Hydrostatic equilibrium and distribution of the von Mises stress: (a) grounded case-1 (maximum stress: 1.7485×10^{7} N) and (b) grounded case-2 (maximum stress: 5.9431×10^{6} N).

Table 2.6: Hydrostatic analysis results of the grounded cargo barge.

Analysis condition	Grounded case-1	Grounded case-2
Number of iterations	4	6
Buoyancy (N)	5.544×10^{8}	6.061×10^{8}
Weight (N)	6.272×10^{8}	6.272×10^{8}
Reaction force at grounding point (N)	0.728×10^{8}	0.211×10^{8}
COB (x_1^b, x_2^b, x_3^b)	(-10.506,0,-3.412)	(-3.262,-1.348,-3.639)
Total strain energy (N·m)	5.149×10^{8}	8.099×10^{8}
Energy criteria	7.155×10^{-9}	4.423×10^{-9}

2.6 Summary

In this chapter, we proposed a numerical method for a nonlinear hydrostatic analysis of flexible floating structures. The incremental equilibrium equation for rigid and flexible (elastic) floating bodies was derived using the updated Lagrangian formulation, which is discretized using the finite element procedure. An effective numerical integration technique was developed to treat the significant wet surface change and thus the non-matching mesh problem is resolved without re-meshing.

The feasibility of the proposed numerical procedure was demonstrated through various hydrostatic problems considering both rigid and flexible body cases. The importance of the nonlinear solution procedure in the stress analysis of flexible floating structures was discussed. The configurations in hydrostatic equilibrium and the corresponding stress distributions were presented for various floating and loading conditions.

The proposed numerical method can be easily used for the stress analysis of damaged ships and offshore platforms with various loading conditions. Moreover, it can be extended to the transient analysis of flexible floating structures in flooded conditions by considering the inertia forces and internal free surface effect.

Chapter 3. Hydroelastic analysis of floating structures with liquid tanks

3.1 Introduction

Since the early 2000s, the hydrodynamic analysis of floating liquid storage structures subjected to surface regular waves has been widely studied due to the significant increase in demand for floating production storage and offloading (FPSO) units, floating liquefied natural gas (FLNG) units, and other related structures. One of the important design issues is the influence of sloshing in liquid tanks on the dynamic response of floating structures during offloading operations, see Refs. [32, 33] for comprehensive reviews of sloshing phenomena and their importance. Related mathematical, numerical, and experimental studies are presented in Refs. [34, 35, 36, 37, 38, 39, 40, 41, 42, 43, 44, 45, 46, 47, 48, 49].

Most previous studies mainly addressed the coupling effect between rigid body motions and sloshing. However, the size and the weight of floating liquid storage structures are becoming increasingly greater in tandem with growing market demand and on the basis of their economic benefits. In such floating structural systems, the assumption of rigid body motions is no longer suitable because, as the dimensions of floating structures increase, the overall stiffness decreases, resulting in relatively low resonant frequencies close to the range of excitation frequencies and sloshing resonance frequencies. In spite of the increasing importance of the hydroelastic behavior of floating liquid storage structures, few related studies have been reported [50, 51, 52]. Accordingly, a complete mathematical formulation has not been developed and the numerical results have not been verified by experimental studies.

A direct coupling method was first developed for 1D and 2D linear hydroelastic problems [13, 14, 15, 16]. The main idea is that the structural and fluid equations are directly coupled to each other and the coupled equations are solved simultaneously. The solution procedure is consequently simpler than that of the conventional method [34, 37, 43, 44, 47], which requires radiation and diffraction analysis procedures to obtain the interaction coefficients. Recently, this method was generalized for a 3D linear hydroelastic analysis of floating structures by Kim et al. [10]. Since the 3D formulation is obtained by consistently linearizing nonlinear solid mechanics equations, all the interaction terms including hydrostatic stiffness are included [10, 11, 12].

In this chapter, we extend the direct-coupled formulation developed in Ref. [10, 17, 18] for a hydroelastic analysis of floating structures with liquid tanks. The structural formulation is based on the updated Lagrangian approach, which is consistently applied to hydrostatic and steady state hydrodynamic analyses. The velocity potential is employed to model both internal and external fluid flows without decomposing them into the diffraction and radiation potentials. The finite element method is employed for the structure and the internal fluid, and the boundary element method is used for the external fluid. The structural equation is then directly coupled with the fluid equations. The use of the mode superposition method for the discrete structural and internal fluid equations is also introduced to improve the computational efficiency. Of course, all the interaction terms among structural motions, sloshing and water waves are completely included in the formulation. In particular, the initial stress is correctly considered in the geometric stiffness [10, 11]. In the fluid formulation, we use the extended boundary integral equations to remove the well-known irregular frequency effect [53, 54, 55].

To verify the proposed formulation, various numerical tests including free-vibration, rigid body hydrodynamic and hydroelastic analyses are conducted for a box barge with three rectangular liquid tanks. We then present the 3D hydroelastic experiments performed to verify the proposed formulation. A floating production unit (FPU) model with three rectangular sloshing tanks was designed and fabricated for the experimental tests in an ocean basin. An overall description of the experimental setup and the test model are provided in detail. The measured dynamic responses are compared with the numerical results obtained using the proposed formulation.

We present the mathematical formulation in Section 3.2 and the numerical procedure in Section 3.3, and several numerical test results are provided in Section 3.4. In Section 3.5, the overall description of the experimental setup is presented and the test results are compared with the numerical results.

3.2 Mathematical formulation

Figure 3.1 shows the problem description considered in this study. It is assumed that the floating structure has a homogeneous, isotropic, and linear elastic material and the fluid flow is incompressible, inviscid, and irrotational and thus the potential flow theory can be used. An incident regular water wave comes continuously from the positive x_1 direction with an angle θ and the amplitude is assumed to be small enough to use the linear wave theory. Also, the resulting motions of the floating structure and sloshing in tanks are assumed to be small. All the waves are gravity waves with a zero atmospheric pressure assumption and the surface tension effect is ignored.

The volumes occupied by the floating structure, the internal fluid in tanks, and the external fluid are denoted by V_S, V_{FI}, and V_{FE}, respectively. The surface of the floating structure S_S consists of dry, internal wet, and external wet surfaces, which are denoted by S_D, S_{WI}, and S_{WE}, respectively. The internal fluid is bounded by the internal wet surface and the internal free surface and the external fluid is enveloped by the external wet surface S_{WE}, the external free surface S_{FE}, the surface S_∞ which is a circular cylinder with a sufficiently large radius R, and a flat bottom surface S_G. The external water depth h_E is measured from the flat bottom to the external free surface of calm water. The internal water depth ($h_I = h_I(x_1, x_2)$) is the distance from the wet surface (S_{WI}) to the free surface (S_{FI}) at rest in tanks.

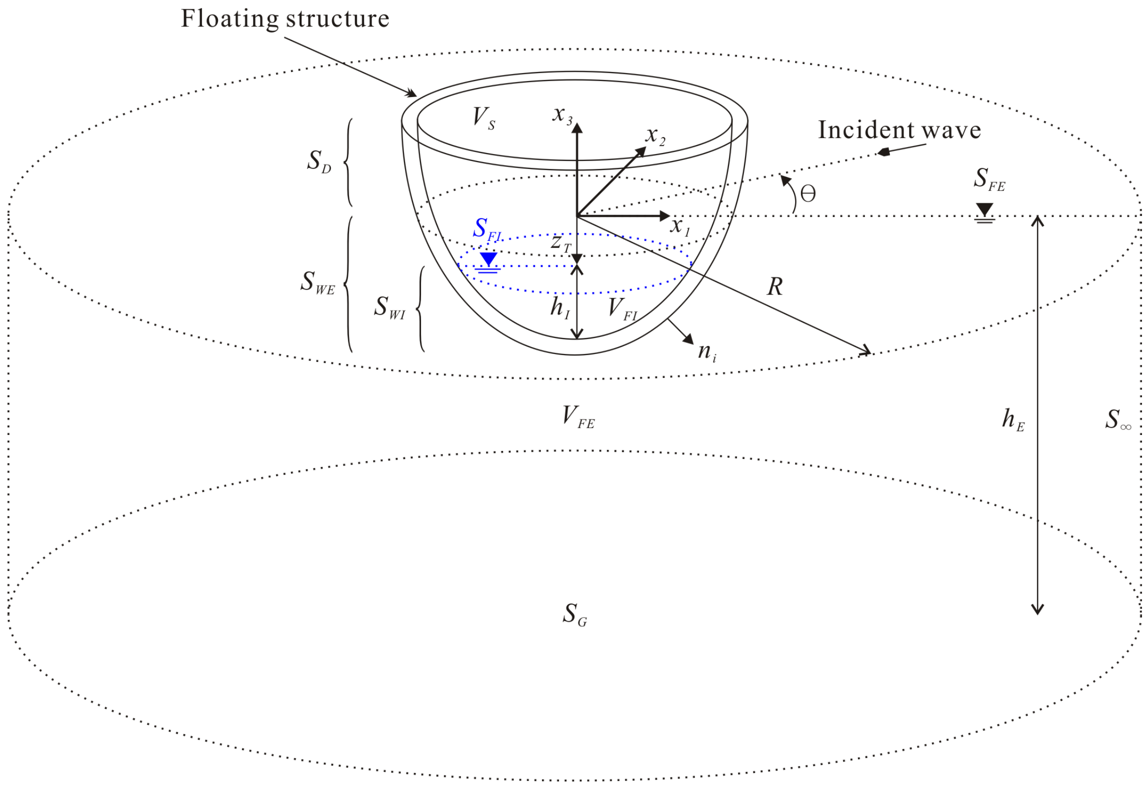

Figure 3.1: Problem description: a floating structure with a liquid tank in an incident water wave.

The fixed Cartesian coordinate system (x_1, x_2, x_3) on the external free surface of calm water is introduced. For clear and compact notation, the subscripts i and j, which vary from 1 to 3, are used to express the components of tensors and the Einstein summation convention is adopted.

Figure 3.2 shows three important states: initial state, hydrostatic equilibrium state, and hydrodynamic equilibrium state. The initial state is a virtual configuration in which the structure does not contact the external and internal fluids. These three states are denoted by the left superscripts $\tilde{0}$, 0, and t, respectively. The material point vectors for the floating structure in each state are then expressed by ${}^{\tilde{0}}x_i$, ${}^{0}x_i$, and ${}^{t}x_i$, respectively. The displacement vectors of the floating structure are defined by

$$ {}^{0}_{\tilde{0}}u_i = {}^{0}x_i - {}^{\tilde{0}}x_i, \quad {}^{t}_{\tilde{0}}u_i = {}^{t}x_i - {}^{\tilde{0}}x_i, \quad {}^{t}_{0}u_i = {}^{t}x_i - {}^{0}x_i. \tag{3.1} $$

The total pressure fields of the external and internal fluids are defined as

$$ {}^{0}P_E = -\rho_E g x_3, \quad {}^{t}P_E = -\rho_E g x_3 + {}^{t}P_{DE}, $$

$$ {}^{0}P_I = -\rho_I g x_{I3}, \quad {}^{t}P_I = -\rho_I g x_{I3} + {}^{t}P_{DI}; \quad x_{I3} = x_3 - z_T, \tag{3.2} $$

where ρ_E is the density of the external fluid, ρ_I is the density of the internal fluid, g is the gravitational acceleration, z_T is the vertical position of the internal free surface, and ${}^{t}P_{DE}$ and ${}^{t}P_{DI}$ are the hydrodynamic pressures for the external and internal fluids.

In the following sections, the mathematical formulations of the floating structure, the external fluid, and the internal fluid are briefly derived. The detailed derivation of the formulations for the floating structure and the external fluid can be found in [10].

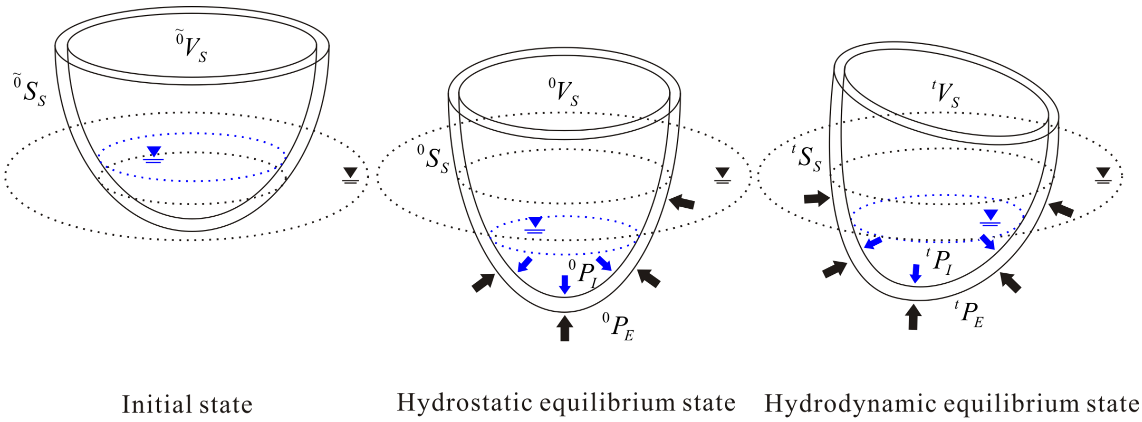

Figure 3.2: Three equilibrium states.

3.2.1 Equations for the floating structure

Note that a hydrostatic analysis is an essential procedure to find the hydrostatic equilibrium state referred to the configuration of the initial state. Through a hydrodynamic analysis, we find the hydrodynamic equilibrium state referred to the configuration of the hydrostatic equilibrium state.

The updated Lagranagian formulation [25] is consistently applied to the hydrostatic and hydrodynamic analyses. The equilibrium equations at time $\tau + \Delta\tau$ are

$$
\begin{aligned}
&\frac{\partial^{\tau+\Delta\tau}\sigma_{ij}}{\partial^{\tau+\Delta\tau}x_j} - {}^{\tau+\Delta\tau}\rho_s g\delta_{i3} - {}^{\tau+\Delta\tau}\rho_s{}^{\tau+\Delta\tau}\ddot{x}_i = 0 && \text{in } {}^{\tau+\Delta\tau}V_S, \\
&{}^{\tau+\Delta\tau}\sigma_{ij}{}^{\tau+\Delta\tau}n_j = -{}^{\tau+\Delta\tau}P_E{}^{\tau+\Delta\tau}n_i && \text{on } {}^{\tau+\Delta\tau}S_{WE}, \\
&{}^{\tau+\Delta\tau}\sigma_{ij}{}^{\tau+\Delta\tau}n_j = -{}^{\tau+\Delta\tau}P_I{}^{\tau+\Delta\tau}n_i && \text{on } {}^{\tau+\Delta\tau}S_{WI}, \\
&{}^{\tau+\Delta\tau}\sigma_{ij}{}^{\tau+\Delta\tau}n_j = 0 && \text{on } {}^{\tau+\Delta\tau}S_D, \qquad (3.3)
\end{aligned}
$$

where σ_{ij} is the Cauchy stress tensor, ρ_s is the density of the floating structure, ${}^{\tau+\Delta\tau}n_i$ is the unit normal vector outward from the floating structure to both the internal and external fluids, δ_{ij} is the Kronecker delta, and the over-dot represents the material time derivative.

After linearizing the principle of virtual work at time $\tau+\Delta\tau$ referred to the configuration at time τ, the following weak form can be obtained

$$\int_{{}^{\tau}V_S} {}^{\tau}\rho_s \, {}^{\tau+\Delta\tau}_{\;\;0}\ddot{u}_i \bar{u}_i \, \mathrm{d}V + \int_{{}^{\tau}V_S} C_{ijkl} \, {}^{\tau+\Delta\tau}_{\;\;\tau}e_{kl} \, {}_{\tau}\bar{e}_{ij} \, \mathrm{d}V + \int_{{}^{\tau}V_S} {}^{\tau}\sigma_{ij} \, {}^{\tau+\Delta\tau}_{\;\;\tau}\bar{\eta}_{ij} \, \mathrm{d}V$$

$$- \int_{{}^{\tau}S_{WE}} \rho_E g \, {}^{\tau+\Delta\tau}_{\;\;\tau}u_3 \, {}^{\tau}n_i \bar{u}_i \, \mathrm{d}S - \int_{{}^{\tau}S_{WI}} \rho_I g \, {}^{\tau+\Delta\tau}_{\;\;\tau}u_3 \, {}^{\tau}n_i \bar{u}_i \, \mathrm{d}S$$

$$- \int_{{}^{\tau}S_{WE}} \rho_E g \, {}^{\tau}x_3 \, {}^{\tau}n_j \, {}_{\tau+\Delta\tau}^{\;\;\;\;\tau}\mathcal{Q}_{ij} \bar{u}_i \, \mathrm{d}S - \int_{{}^{\tau}S_{WI}} \rho_I g \, {}^{\tau}x_{I3} \, {}^{\tau}n_j \, {}_{\tau+\Delta\tau}^{\;\;\;\;\tau}\mathcal{Q}_{ij} \bar{u}_i \, \mathrm{d}S$$

$$+ \int_{{}^{\tau}S_{WE}} {}^{\tau+\Delta\tau}P_{DE} \, {}^{\tau}n_i \bar{u}_i \, \mathrm{d}S + \int_{{}^{\tau}S_{WI}} {}^{\tau+\Delta\tau}P_{DI} \, {}^{\tau}n_i \bar{u}_i \, \mathrm{d}S$$

$$= - \int_{{}^{\tau}V_S} {}^{\tau}\rho_s g \bar{u}_3 \, \mathrm{d}V - \int_{{}^{\tau}V_S} {}^{\tau}\sigma_{ij} \, {}_{\tau}\bar{e}_{ij} \, \mathrm{d}V + \int_{{}^{\tau}S_{WE}} \rho_E g \, {}^{\tau}x_3 \, {}^{\tau}n_i \bar{u}_i \, \mathrm{d}S + \int_{{}^{\tau}S_{WI}} \rho_I g \, {}^{\tau}x_{I3} \, {}^{\tau}n_i \bar{u}_i \, \mathrm{d}S, \quad (3.4)$$

where

$${}^{\tau+\Delta\tau}_{\;\;\tau}e_{ij} = \frac{1}{2}\left(\frac{\partial \, {}^{\tau+\Delta\tau}_{\;\;\tau}u_i}{\partial \, {}^{\tau}x_j} + \frac{\partial \, {}^{\tau+\Delta\tau}_{\;\;\tau}u_j}{\partial \, {}^{\tau}x_i}\right), \quad {}_{\tau}\bar{e}_{ij} = \frac{1}{2}\left(\frac{\partial \bar{u}_i}{\partial \, {}^{\tau}x_j} + \frac{\partial \bar{u}_j}{\partial \, {}^{\tau}x_i}\right),$$

$${}^{\tau+\Delta\tau}_{\;\;\tau}\bar{\eta}_{ij} = \frac{1}{2}\left(\frac{\partial \bar{u}_k}{\partial \, {}^{\tau}x_i}\frac{\partial \, {}^{\tau+\Delta\tau}_{\;\;\tau}u_k}{\partial \, {}^{\tau}x_j} + \frac{\partial \, {}^{\tau+\Delta\tau}_{\;\;\tau}u_k}{\partial \, {}^{\tau}x_i}\frac{\partial \bar{u}_k}{\partial \, {}^{\tau}x_j}\right), \quad {}_{\tau+\Delta\tau}^{\;\;\;\;\tau}\mathcal{Q}_{ij} = \delta_{ij}\frac{\partial \, {}^{\tau+\Delta\tau}_{\;\;\tau}u_k}{\partial \, {}^{\tau}x_k} - \frac{\partial \, {}^{\tau+\Delta\tau}_{\;\;\tau}u_j}{\partial \, {}^{\tau}x_i}, \quad (3.5)$$

in which ${}^{\tau+\Delta\tau}_{\;\;\tau}u_i$ is the displacement from the configuration at time τ to the configuration at time $\tau+\Delta\tau$, $\bar{u}_i$ is the virtual displacement vector, ${}_{\tau}\bar{e}_{ij}$ and ${}^{\tau+\Delta\tau}_{\;\;\tau}\bar{\eta}_{ij}$ are the virtual linear and nonlinear strain tensors, and C_{ijkl} is the stress-strain relation tensor.

In the hydrostatic analysis, the acceleration $\ddot{u}_i$ and the hydrodynamic pressures P_{DE} and P_{DI} are equal to zero. Setting $\tau = \tilde{0}$ and $\tau + \Delta\tau = 0$ in Equation 3.4, we obtain the following nonlinear incremental equation for the hydrostatic analysis:

$$
\begin{aligned}
&\int_{{}^{\tilde{0}}V_S} C_{ijkl}\,{}^{0}_{\tilde{0}}e_{kl}\,{}_{0}\bar{e}_{ij}\ \mathrm{d}V + \int_{{}^{\tilde{0}}V_S} {}^{\tilde{0}}\sigma_{ij}\,{}^{0}_{\tilde{0}}\bar{\eta}_{ij}\ \mathrm{d}V \\
&- \int_{{}^{\tilde{0}}S_{WE}} \rho_E g\,{}^{0}_{\tilde{0}}u_3\,{}^{\tilde{0}}n_i \bar{u}_i\ \mathrm{d}S - \int_{{}^{\tilde{0}}S_{WI}} \rho_I g\,{}^{0}_{\tilde{0}}u_3\,{}^{\tilde{0}}n_i \bar{u}_i\ \mathrm{d}S \\
&- \int_{{}^{\tilde{0}}S_{WE}} \rho_E g\,{}^{\tilde{0}}x_3\,{}^{\tilde{0}}n_j\,{}^{\tilde{0}}_{0}\mathcal{Q}_{ij}\bar{u}_i\ \mathrm{d}S - \int_{{}^{\tilde{0}}S_{WI}} \rho_I g\,{}^{\tilde{0}}x_{I3}\,{}^{\tilde{0}}n_j\,{}^{\tilde{0}}_{0}\mathcal{Q}_{ij}\bar{u}_i\ \mathrm{d}S \\
&= - \int_{{}^{\tilde{0}}V_S} {}^{\tilde{0}}\rho_s g \bar{u}_3\ \mathrm{d}V - \int_{{}^{\tilde{0}}V_S} {}^{\tilde{0}}\sigma_{ij}\,{}_{\tilde{0}}\bar{e}_{ij}\ \mathrm{d}V + \int_{{}^{\tilde{0}}S_{WE}} \rho_E g\,{}^{\tilde{0}}x_3\,{}^{\tilde{0}}n_i \bar{u}_i\ \mathrm{d}S + \int_{{}^{\tilde{0}}S_{WI}} \rho_I g\,{}^{\tilde{0}}x_{I3}\,{}^{\tilde{0}}n_i \bar{u}_i\ \mathrm{d}S. \qquad (3.6)
\end{aligned}
$$

Note that an iterative solution scheme like the Newton-Raphson method is required to find the hydrostatic equilibrium state using Equation 3.6.

Once the hydrostatic equilibrium state is obtained, the right hand side of. Equation 3.4 vanishes. We then set $\tau = 0$ and $\tau + \Delta\tau = t$ in Equation 3.4 and invoke a harmonic response with angular frequency ω (${}^t_0u_i = \mathrm{Re}\left\{ u_i({}^0\mathbf{x})e^{j\omega t} \right\}$; $j = \sqrt{-1}$). Finally, the following equation is obtained for a hydrodynamic analysis in the steady state:

$$
\begin{aligned}
&-\omega^2 \int_{{}^0V_S} {}^0\rho_s u_i \bar{u}_i \,\mathrm{d}V + \int_{{}^0V_S} C_{ijkl} e_{kl}\, {}_0\bar{e}_{ij} \,\mathrm{d}V + \int_{{}^0V_S} {}^0\sigma_{ij} \bar{\eta}_{ij} \,\mathrm{d}V \\
&- \int_{{}^0S_{WE}} \rho_E g u_3 {}^0n_i \bar{u}_i \,\mathrm{d}S - \int_{{}^0S_{WI}} \rho_I g u_3 {}^0n_i \bar{u}_i \,\mathrm{d}S - \int_{{}^0S_{WE}} \rho_E g {}^0x_3 {}^0n_j \mathcal{Q}_{ij} \bar{u}_i \,\mathrm{d}S \\
&- \int_{{}^0S_{WI}} \rho_I g {}^0x_{I3} {}^0n_j \mathcal{Q}_{ij} \bar{u}_i \,\mathrm{d}S + \int_{{}^0S_{WE}} P_{DE} {}^0n_i \bar{u}_i \,\mathrm{d}S + \int_{{}^0S_{WI}} P_{DI} {}^0n_i \bar{u}_i \,\mathrm{d}S = 0,
\end{aligned} \tag{3.7}
$$

where

$$
{}^t_0e_{ij} = \mathrm{Re}\left\{ e_{ij}({}^0x_k)e^{j\omega t} \right\}, \quad {}^t_0\bar{\eta}_{ij} = \mathrm{Re}\left\{ \bar{\eta}_{ij}({}^0x_k)e^{j\omega t} \right\},
$$

$$
{}^0_t\mathcal{Q}_{ij} = \mathrm{Re}\left\{ \mathcal{Q}_{ij}({}^0x_k)e^{j\omega t} \right\}, \quad {}^tP_{DE} = \mathrm{Re}\left\{ P_{DE}({}^0x_k)e^{j\omega t} \right\} \quad {}^tP_{DI} = \mathrm{Re}\left\{ P_{DI}({}^0x_k)e^{j\omega t} \right\}. \tag{3.8}
$$

Since we assume that the motion of the floating structure is small and the change of the wet surface is negligible, Equation 3.7 can be solved without an iterative solution scheme.

3.2.2 Equations for the external fluid

In the steady state, the governing equation and boundary conditions for the external fluid, which are approximated at the configuration of the hydrostatic equilibrium state, are given as

$$ {}^{t}\phi_E^{'} = \mathrm{Re}\left\{ \phi_E^{'}(x_i)e^{j\omega t} \right\}, \tag{3.9a} $$

$$ \frac{\partial^2 \phi_E^{'}}{\partial x_i \partial x_i} = 0 \qquad \text{in } {}^{0}V_{FE}, \tag{3.9b} $$

$$ \frac{\partial \phi_E^{'}}{\partial x_3} = \frac{\omega^2}{g}\phi_E^{'} \qquad \text{for } x_3 = 0 \text{ on } S_{FE}, \tag{3.9c} $$

$$ \frac{\partial \phi_E^{'}}{\partial x_3} = 0 \qquad \text{on } S_G \ (x_3 = -h_E), \tag{3.9d} $$

$$ \sqrt{R}\left(\frac{\partial}{\partial R} + jk\right)(\phi_E^{'} - \phi^I) = 0 \qquad \text{on } S_\infty \ (R \to \infty), \tag{3.9e} $$

$$ \frac{\partial \phi_E^{'}}{\partial n} = j\omega u_i n_i \qquad \text{on } {}^{0}S_{WE}, \tag{3.9f} $$

where $\phi_E^{'}$ is the velocity potential for the external fluid, k is the wave number, ϕ^I is the velocity potential for an incident wave, Equation 3.9c is the combined free surface boundary condition linearized at $x_3 = 0$ [56, 57], and Equation 3.9e is the Sommerfeld radiation condition [56]. The body boundary condition in Equation 3.9f means that the normal velocities of the structure and the external fluid should be the same on the external wet surface.

The corresponding boundary integral equation is

$$2\pi\phi_E^{'} - P.V. \int_{{}^0S_{WE}} \frac{\partial G(x_i;\xi_i)}{\partial n(\xi_i)} \phi_E^{'}(\xi_i) \mathrm{d}S_\xi$$

$$= -P.V. \int_{{}^0S_{WE}} G(x_i;\xi_i) \frac{\phi_E^{'}(\xi_i)}{\partial n(\xi_i)} \mathrm{d}S_\xi + 4\pi\phi^I(x_i) \quad \text{for } x_i \text{ on } {}^0S_{WE}, \tag{3.10}$$

where $P.V.$ refers to the Cauchy principal value, the subscript ξ denotes that the integral is conducted with respect to the variable ξ_i, and $G(x_i;\xi_i)$ is the Green's function, which is located at position ξ_i and generated by a source potential with strength -4π and angular frequency ω. The detailed procedure to obtain the Green's function in finite and infinite depth cases is described by Wehausen and Laitone [57].

It should be noted that Equation 3.10 could result in the irregular frequencies and thus the coefficient matrix in the corresponding discrete equation becomes ill-conditioned near these frequencies. In order to remove the irregular frequency effects, several methods have been developed by Ohmatsu [53], Kleinman [54], and Lee et al. [55]. We here employ the extended boundary integral equations [55].

$$2\pi\phi_E^{'}(x_i) - P.V. \int_{{}^0S_{WE}+{}^0S_{FI}^{EXT}} \frac{\partial G(x_i;\xi_i)}{\partial n(\xi_i)} \phi_E^{'}(\xi_i) \mathrm{d}S_\xi$$

$$= -P.V. \int_{{}^0S_{WE}} G(x_i;\xi_i) \frac{\partial \phi_E^{'}(\xi_i)}{\partial n(\xi_i)} \mathrm{d}S_\xi + 4\pi\phi^I(x_i) \quad \text{for } x_i \text{ on } {}^0S_{WE}, \tag{3.11a}$$

$$-4\pi\phi_E^{EXT}(x_i) - P.V. \int_{{}^0S_{WE}+{}^0S_{FI}^{EXT}} \frac{\partial G(x_i;\xi_i)}{\partial n(\xi_i)} \phi_E^{EXT}(\xi_i) \mathrm{d}S_\xi$$

$$= -P.V. \int_{{}^0S_{WE}} G(x_i;\xi_i) \frac{\partial \phi_E^{EXT}(\xi_i)}{\partial n(\xi_i)} \mathrm{d}S_\xi + 4\pi\phi^I(x_i) \quad \text{for } x_i \text{ on } {}^0S_{FI}^{EXT}, \tag{3.11b}$$

where ${}^0S_{FI}^{EXT}$ is the extended internal free surface described in Figure 3.3 and ϕ_E^{EXT} is the velocity potential on the extended boundary ${}^0S_{FI}^{EXT}$.

Multiplying test functions $\bar{\phi}_E^{'}$ and $\bar{\phi}_E^{EXT}$ to Equations 3.11a and 3.11b, respectively, and integrating over the external wet surface ${}^0S_{WE}$ and the internal free surface ${}^0S_{FI}^{EXT}$, the following equations are obtained:

$$2\pi \int_{{}^0S_{WE}} \phi_E^{'} \bar{\phi}_E^{'} \mathrm{d}S - \int_{{}^0S_{WE}} P.V. \int_{{}^0S_{WE}+{}^0S_{FI}^{EXT}} \left(\frac{\partial G}{\partial n_\xi} \phi_E^{'} - G \frac{\partial \phi_E^{'}}{\partial n_\xi} \right) \mathrm{d}S_\xi \ \bar{\phi}_E^{'} \ \mathrm{d}S_x$$

$$= 4\pi \int_{{}^0S_{WE}} \phi^I \bar{\phi}_E^{'} \mathrm{d}S \qquad \text{for } x_i \text{ on } {}^0S_{WE}, \tag{3.12a}$$

$$-4\pi \int_{{}^0S_{FI}^{EXT}} \phi_E^{EXT} \bar{\phi}_E^{EXT} \mathrm{d}S - \int_{{}^0S_{FI}^{EXT}} P.V. \int_{{}^0S_{WE}+{}^0S_{FI}^{EXT}} \left(\frac{\partial G}{\partial n_\xi} \phi_E^{EXT} - G \frac{\partial \phi_E^{EXT}}{\partial n_\xi} \right) \mathrm{d}S_\xi \ \bar{\phi}_E^{EXT} \ \mathrm{d}S_x$$

$$= 4\pi \int_{{}^0S_{FI}^{EXT}} \phi^I \bar{\phi}_E^{EXT} \mathrm{d}S \qquad \text{for } x_i \text{ on } {}^0S_{FI}^{EXT}. \tag{3.12b}$$

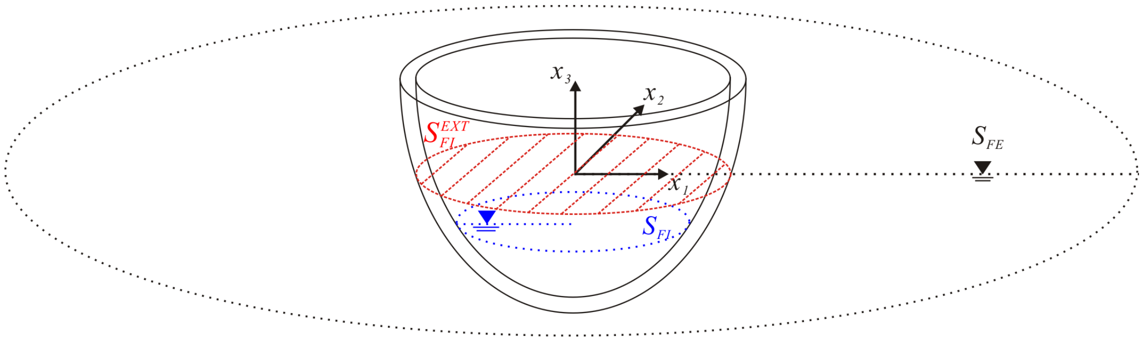

Figure 3.3: Extended internal free surface (${}^0S_{FI}^{EXT}$).

3.2.3 Equations for the internal fluid

In the steady state, the governing equation and boundary conditions for the internal fluid in tanks, which are approximated at the configuration of the hydrostatic equilibrium state, are given as

$$ {}^{\mathrm{t}}\phi_I = \mathrm{Re}\left\{\phi_I(x_i)e^{j\omega t}\right\}, \tag{3.13a}$$

$$ \rho_I \frac{\partial^2 \phi_I}{\partial x_i \partial x_i} = 0 \qquad \text{in } {}^0V_{FI}, \tag{3.13b}$$

$$ \frac{\partial \phi_I}{\partial x_3} = \frac{\omega^2}{g}\phi_I \qquad \text{on } {}^0S_{FI}\ (x_3 = z_T), \tag{3.13c}$$

$$ \frac{\partial \phi_I}{\partial n} = j\omega u_i n_i \qquad \text{on } {}^0S_{WI}, \tag{3.13d}$$

where ${}^{\mathrm{t}}\phi_I$ is the velocity potential in time domain and ϕ_I are the velocity potentials in the steady state.

By multiplying a test function $\bar{\phi}_I$ to 3.13b and integrating over the volume of the internal fluid ${}^0V_{FI}$, the following equation can be obtained:

$$ \int_{{}^0V_{FI}} \rho_I \frac{\partial^2 \phi_I}{\partial x_i \partial x_i} \mathrm{d}V = 0. \tag{3.14}$$

After Equation 3.14 is integrated by part and the divergence theorem and the boundary condition in Equation 3.13c are applied to Equation 3.14, the weak form equation of the internal fluid is obtained

$$ \int_{{}^0S_{FI}} \rho_I \left(\frac{\omega^2}{g}\right) \phi_I \bar{\phi}_I \mathrm{d}S - \int_{{}^0S_{WI}} \rho_I \frac{\partial \phi_I}{\partial n} \bar{\phi}_I \mathrm{d}S - \int_{{}^0V_{FI}} \rho_I \frac{\partial \phi_I}{\partial x_i}\frac{\partial \bar{\phi}_I}{\partial x_i} \mathrm{d}V = 0. \tag{3.15}$$

3.2.4 Direct-coupled equations

To obtain the direct-coupled equations, Equation 3.7 for the floating structure, Equation 3.12a and 3.12b for the external fluid, and Equation 3.15 for the internal fluid are considered with the interaction conditions in Equations 3.9f and 3.13d. Using the linearized Bernoulli equations, the hydrodynamic pressures P_{DE} and P_{DI} can be expressed as

$$P_{DE} = -j\omega\rho_E\phi_E^{'}, \quad P_{DI} = -j\omega\rho_I\phi_I. \tag{3.16}$$

Substituting Equation 3.16 into Equation 3.7, Equation 3.9f into Equation 3.12a and 3.12b, and Equation 3.13d into Equation 3.15, the following coupled equations are obtained:

$$\begin{aligned}
&-\omega^2\int_{{}^0V_S} {}^0\rho_s u_i\bar{u}_i \,\mathrm{d}V + \int_{{}^0V_S} C_{ijkl}e_{kl\,0}\bar{e}_{ij}\,\mathrm{d}V + \int_{{}^0V_S} {}^0\sigma_{ij}\bar{\eta}_{ij}\,\mathrm{d}V \\
&-\int_{{}^0S_{WE}} \rho_E g u_3{}^0n_i\bar{u}_i\,\mathrm{d}S - \int_{{}^0S_{WI}} \rho_I g u_3{}^0n_i\bar{u}_i\,\mathrm{d}S \\
&-\int_{{}^0S_{WE}} \rho_E g{}^0x_3{}^0n_j\mathcal{Q}_{ij}\bar{u}_i\,\mathrm{d}S - \int_{{}^0S_{WI}} \rho_I g{}^0x_{I3}{}^0n_j\mathcal{Q}_{ij}\bar{u}_i\,\mathrm{d}S \\
&-\int_{{}^0S_{WE}} j\omega\rho_E\phi_E^{'}{}^0n_i\bar{u}_i\,\mathrm{d}S - \int_{{}^0S_{WI}} j\omega\rho_I\phi_I{}^0n_i\bar{u}_i\,\mathrm{d}S = 0,
\end{aligned} \tag{3.17}$$

$$2\pi \int_{{}^0S_{WE}} \phi_E^{'} \bar{\phi}_E^{'} \mathrm{d}S - \int_{{}^0S_{WE}} P.V. \int_{{}^0S_{WE} + {}^0S_{FI}^{EXT}} \left(\frac{\partial G}{\partial n_\xi} \phi_E^{'} - j\omega G u_i n_i \right) \mathrm{d}S_\xi \; \bar{\phi}_E^{'} \; \mathrm{d}S_x$$

$$= 4\pi \int_{{}^0S_{WE}} \phi^I \bar{\phi}_E^{'} \mathrm{d}S \qquad \text{for } x_i \text{ on } {}^0S_{WE}, \tag{3.18a}$$

$$-4\pi \int_{{}^0S_{FI}^{EXT}} \phi_E^{EXT} \bar{\phi}_E^{EXT} \mathrm{d}S - \int_{{}^0S_{FI}^{EXT}} P.V. \int_{{}^0S_{WE} + {}^0S_{FI}^{EXT}} \left(\frac{\partial G}{\partial n_\xi} \phi_E^{EXT} - j\omega G u_i n_i \right) \mathrm{d}S_\xi \; \bar{\phi}_E^{EXT} \; \mathrm{d}S_x$$

$$= 4\pi \int_{{}^0S_{FI}^{EXT}} \phi^I \bar{\phi}_E^{EXT} \mathrm{d}S \qquad \text{for } x_i \text{ on } {}^0S_{FI}^{EXT}, \tag{3.18b}$$

and

$$\int_{{}^0S_{FI}} \rho_I \left(\frac{\omega^2}{g} \right) \phi_I \bar{\phi}_I \mathrm{d}S - j\omega \int_{{}^0S_{WI}} \rho_I u_i n_i \bar{\phi}_I \mathrm{d}S - \int_{{}^0V_{FI}} \rho_I \frac{\partial \phi_I}{\partial x_i} \frac{\partial \bar{\phi}_I}{\partial x_i} \mathrm{d}V = 0. \tag{3.19}$$

3.3 Numerical methods

In this section, the direct-coupled equations are discretized by using the finite and boundary element methods. In addition, for efficient computation, reduced linear equations are introduced by using the mode superposition method. We also extract added mass matrices, the radiated wave damping matrix, and the wave exciting force vector for the 3D hydroelastic analysis of floating structures with liquid tanks.

3.3.1 Finite and boundary element discretization

The finite element method is employed for the floating structure and internal fluid in tanks, and the boundary element method is used for the external fluid. The finite and boundary element meshes and the mesh matching scheme are depicted in Figure 3.4.

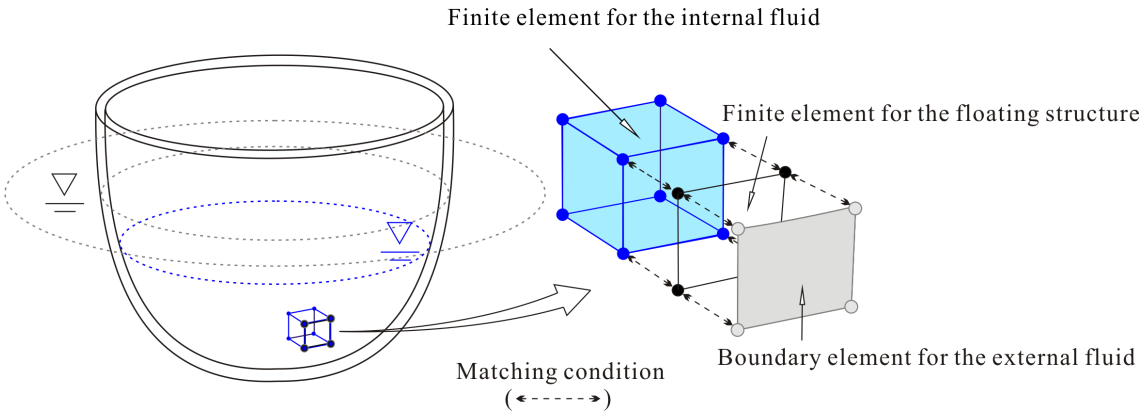

Figure 3.4: Finite and boundary element discretization and mesh matching scheme.

The fields of structural displacements and velocity potentials are interpolated using the nodal displacement vector ($\mathbf{u}$) and the nodal velocity potential vectors ($\mathbf{\Phi}_I$ and $\mathbf{\Phi}_E$) for internal and external fluids, in which $\mathbf{\Phi}_E = [\mathbf{\Phi}_E^{'} \quad \mathbf{\Phi}_E^{EXT}]^{\mathrm{T}}$, and $\mathbf{\Phi}_E^{'}$ and $\mathbf{\Phi}_E^{EXT}$ corresponds to the velocity potentials $\phi_E^{'}$ and ϕ_E^{EXT}, respectively.

The term-by-term finite element discretization of Equation 3.17 yields:

$$\omega^2 \int_{{}^0V_S} {}^0\rho_s u_i \bar{u}_i \mathrm{d}V = \bar{\mathbf{u}}^{\mathrm{T}} \omega^2 \mathbf{S}_M \mathbf{u}, \tag{3.20a}$$

$$\int_{{}^0V_S} C_{ijkl} e_{kl0} \bar{e}_{ij} \mathrm{d}V = \bar{\mathbf{u}}^{\mathrm{T}} \mathbf{S}_K \mathbf{u}, \tag{3.20b}$$

$$\int_{{}^0V_S} {}^0\sigma_{ij} \bar{\eta}_{ij} \mathrm{d}V = \bar{\mathbf{u}}^{\mathrm{T}} \mathbf{S}_{KN} \mathbf{u}, \tag{3.20c}$$

$$\int_{{}^0S_{WE}} \rho_E g u_3 {}^0n_i \bar{u}_i \mathrm{d}S = \bar{\mathbf{u}}^{\mathrm{T}} \mathbf{S}_{HD}^E \mathbf{u}, \quad \int_{{}^0S_{WI}} \rho_I g u_3 {}^0n_i \bar{u}_i \mathrm{d}S = \bar{\mathbf{u}}^{\mathrm{T}} \mathbf{S}_{HD}^I \mathbf{u}, \tag{3.20d}$$

$$\int_{{}^0S_{WE}} \rho_E g {}^0x_3 {}^0n_j \mathcal{Q}_{ij} \bar{u}_i \mathrm{d}S = \bar{\mathbf{u}}^{\mathrm{T}} \mathbf{S}_{HN}^E \mathbf{u}, \quad \int_{{}^0S_{WI}} \rho_I g {}^0x_{I3} {}^0n_j \mathcal{Q}_{ij} \bar{u}_i \mathrm{d}S = \bar{\mathbf{u}}^{\mathrm{T}} \mathbf{S}_{HN}^I \mathbf{u}, \tag{3.20e}$$

$$j\omega \int_{{}^0S_{WE}} \rho_E \phi_E {}^0n_i \bar{u}_i \mathrm{d}S = \bar{\mathbf{u}}^{\mathrm{T}} j\omega \mathbf{S}_D^E \mathbf{\Phi}_E, \quad j\omega \int_{{}^0S_{WI}} \rho_I \phi_I {}^0n_i \bar{u}_i \mathrm{d}S = \bar{\mathbf{u}}^{\mathrm{T}} j\omega \mathbf{S}_D^I \mathbf{\Phi}_I. \tag{3.20f}$$

Similarly, the boundary element discretization of Equation 3.18a and 3.18b yields

$$2\pi \int_{{}^0S_{WE}} \phi_E^{'} \bar{\phi}_E^{'} \mathrm{d}S - 4\pi \int_{{}^0S_{FI}^{EXT}} \phi_E^{EXT} \bar{\phi}_E^{EXT} \mathrm{d}S = \bar{\mathbf{\Phi}}_E^{\mathrm{T}} \mathbf{F}_M^E \mathbf{\Phi}_E, \tag{3.21a}$$

$$\int_{{}^0S_{WE}} P.V. \int_{{}^0S_{WE}+{}^0S_{FI}^{EXT}} \frac{\partial G}{\partial n_\xi} \phi_E^{'} \mathrm{d}S_\xi \; \bar{\phi}_E^{'} \; \mathrm{d}S_x$$

$$+ \int_{{}^0S_{FI}^{EXT}} P.V. \int_{{}^0S_{WE}+{}^0S_{FI}^{EXT}} \frac{\partial G}{\partial n_\xi} \phi_E^{EXT} \mathrm{d}S_\xi \; \bar{\phi}_E^{EXT} \; \mathrm{d}S_x = \bar{\mathbf{\Phi}}_E^{\mathrm{T}} \mathbf{F}_{Gn}^E \mathbf{\Phi}_E, \tag{3.21b}$$

$$j\omega \int_{{}^0S_{WE}} P.V. \int_{{}^0S_{WE}+{}^0S_{FI}^{EXT}} G u_i n_i \mathrm{d}S_\xi \; \bar{\phi}_E^{'} \; \mathrm{d}S_x$$

$$+ j\omega \int_{{}^0S_{FI}^{EXT}} P.V. \int_{{}^0S_{WE}+{}^0S_{FI}^{EXT}} G u_i n_i \mathrm{d}S_\xi \; \bar{\phi}_E^{EXT} \; \mathrm{d}S_x = \bar{\mathbf{\Phi}}_E^{\mathrm{T}} j\omega \mathbf{F}_G \mathbf{u}, \tag{3.21c}$$

$$4\pi \left(\int_{{}^0S_{WE}} \phi^I \bar{\phi}_E^{'} \mathrm{d}S + \int_{{}^0S_{WE}} \phi^I \bar{\phi}_E^{'} \mathrm{d}S \right) = \bar{\mathbf{\Phi}}_E^{\mathrm{T}} 4\pi \mathbf{R}_I. \tag{3.21d}$$

Finally, the finite element discretization of Equation 3.19 yields

$$\int_{{}^0S_{FI}} \rho_I \left(\frac{\omega^2}{g} \right) \phi_I \bar{\phi}_I \mathrm{d}S = \bar{\mathbf{\Phi}}_I^{\mathrm{T}} \omega^2 \mathbf{F}_M^I \bar{\mathbf{\Phi}}_I, \tag{3.22a}$$

$$j\omega \int_{{}^0S_{WI}} \rho_I u_i n_i \bar{\phi}_I \mathrm{d}S = \bar{\mathbf{\Phi}}_I^{\mathrm{T}} j\omega \mathbf{F}_W^I \mathbf{u}, \tag{3.22b}$$

$$\int_{{}^0V_{FI}} \rho_I \frac{\partial \phi_I}{\partial x_i} \frac{\partial \bar{\phi}_I}{\partial x_i} \mathrm{d}V = \bar{\mathbf{\Phi}}_I^{\mathrm{T}} \mathbf{F}_K^I \bar{\mathbf{\Phi}}_I, \tag{3.22c}$$

The final discrete coupled equation for the steady state 3D hydroelastic analysis of floating structures with liquid tanks is given by

$$\begin{bmatrix} -\omega^2\mathbf{S}_M + \mathbf{S}_K + \mathbf{S}_{CH} & -j\omega\mathbf{S}_D^E & -j\omega\mathbf{S}_D^I \\ j\omega\mathbf{F}_G & \mathbf{F}_M^E - \mathbf{F}_{Gn} & 0 \\ -j\omega\mathbf{F}_W^I & 0 & \omega^2\mathbf{F}_M^I - \mathbf{F}_K^I \end{bmatrix} \begin{bmatrix} \mathbf{u} \\ \mathbf{\Phi}_E \\ \mathbf{\Phi}_I \end{bmatrix} = \begin{bmatrix} 0 \\ 4\pi\mathbf{R}_I \\ 0 \end{bmatrix}, \tag{3.23}$$

with $\quad \mathbf{S}_{CH} = \mathbf{S}_{KN} - \mathbf{S}_{HD}^E - \mathbf{S}_{HD}^I - \mathbf{S}_{HN}^E - \mathbf{S}_{HN}^I.$

where the matrix $\mathbf{S}_{CH}$ is the complete hydrostatic stiffness of the floating liquid storage structure. The terms $\mathbf{S}_{HD}^E$, $\mathbf{S}_{HN}^E$, $\mathbf{S}_{HD}^I$, and $\mathbf{S}_{HN}^I$ are the hydrostatic pressure stiffnesses and $\mathbf{S}_{KN}$ is the geometric stiffness. In particular, the contributions of the internal fluid to the hydrostatic pressure stiffness are $\mathbf{S}_{HD}^I$ and $\mathbf{S}_{HN}^I$, and a hydrostatic analysis should be performed in advance to properly obtain the geometric stiffness $\mathbf{S}_{KN}$. Note that no artificial damping is considered in Equation 3.23.

Since the extended boundary integral method is applied in the external fluid part of Equation 3.23, the resonance phenomena induced by sloshing and structural elasticity can be distinguished from the resonances caused by the irregular frequency effects.

3.3.2 Reduced equation

We now apply the standard mode superposition method in Equation 3.23. First, the following two eigenvalue problems should be solved

$$\mathbf{S}_K \boldsymbol{\Psi}_i = \lambda_i \mathbf{S}_M \boldsymbol{\Psi}_i; \qquad i = 1, 2, ..., \ N_a \qquad \text{for the floating structure,} \tag{3.24a}$$

$$\mathbf{F}_K^I \boldsymbol{\gamma}_i = \mu_i \mathbf{F}_M^I \boldsymbol{\gamma}_i; \qquad i = 1, 2, ..., \ M_a \qquad \text{for the internal fluid,} \tag{3.24b}$$

where N_a and M_a are the numbers of degrees of freedom in the floating structure and internal fluid, respectively, $\boldsymbol{\Psi}_i$ and $\boldsymbol{\gamma}_i$ are the eigenvectors which are othonormalized with respect to the matrices $\mathbf{S}_M$ and $\mathbf{F}_M^I$, respectively, and, λ_i and μ_i are the corresponding eigenvalues.

The nodal displacement vector of the floating structures and the nodal potential vector of the internal fluid are approximated as

$$\mathbf{u} \approx q_1 \boldsymbol{\Psi}_1 + q_2 \boldsymbol{\Psi}_2 + \cdots + q_{\hat{N}_a} \boldsymbol{\Psi}_{\hat{N}_a} = \boldsymbol{\Psi}\mathbf{q}, \quad \hat{N}_a < N_a, \tag{3.25a}$$

$$\boldsymbol{\Phi}_I \approx y_1 \boldsymbol{\gamma}_1 + y_2 \boldsymbol{\gamma}_2 + \cdots + y_{\hat{M}_a} \boldsymbol{\gamma}_{\hat{M}_a} = \boldsymbol{\gamma}\mathbf{y}, \quad \hat{M}_a < M_a, \tag{3.25b}$$

in which $\mathbf{q}$ and $\mathbf{y}$ are the generalized coordinate vectors.

Substituting Equation 3.25a and 3.25b into Equation 3.23 and pre-multiplying $\mathbf{\Psi}^{\mathrm{T}}$ and $\boldsymbol{\gamma}^{\mathrm{T}}$ to the structural and internal fluid parts of Equation 3.23, respectively, the following reduced equation is obtained:

$$\begin{bmatrix} -\omega^2\mathbf{I}+\mathbf{\Lambda}+\mathbf{S}_{CH}^{G} & -j\omega\mathbf{\Psi}^{\mathrm{T}}\mathbf{S}_{D}^{E} & -j\omega\mathbf{\Psi}^{\mathrm{T}}\mathbf{S}_{D}^{I}\gamma \\ j\omega\mathbf{F}_{G}\mathbf{\Psi} & \mathbf{F}_{M}^{E}-\mathbf{F}_{Gn} & 0 \\ -j\omega\boldsymbol{\gamma}^{\mathrm{T}}\mathbf{F}_{W}^{I}\mathbf{\Psi} & 0 & \omega^2\mathbf{I}-\Omega \end{bmatrix} \begin{bmatrix} \mathbf{q} \\ \mathbf{\Phi}_{E} \\ \mathbf{y} \end{bmatrix} = \begin{bmatrix} 0 \\ 4\pi\mathbf{R}_{I} \\ 0 \end{bmatrix}, \tag{3.26}$$

where $I_{ij}=\delta_{ij}$, $\Lambda_{ij}=\lambda_i\delta_{ij}$, and $\Omega_{kl}=\mu_k\delta_{kl}$ (no summation); $i,j=1,2,...,\ \hat{N}_a$ and $k,l=1,2,...,\ \hat{M}_a$.

Note that, in Equation 3.26, $\mathbf{S}_{CH}^{G}$ is the complete hydrostatic stiffness in the generalized coordinate ($\mathbf{S}_{CH}^{G}=\mathbf{\Phi}^{\mathrm{T}}\mathbf{S}_{CH}\mathbf{\Phi}$), and the rigid body hydrodynamic analysis can be conducted when only the rigid body modes of the floating structure are contained in Equation 3.25a.

Condensing out the fluid variables in 3.26, we can extract added masses, the radiated wave damping matrix, and the wave exciting force vector in the generalized coordinates. Therefore, the present direct-coupled formulation can be linked term-by-term to the conventional formulation [10, 14]. The condensed structural equation becomes

$$\left[-\omega^2\left(\mathbf{I}+\mathbf{S}_{MA}^{E,G}-\mathbf{S}_{MA}^{I,G}\right)+j\omega\mathbf{S}_{CW}^{G}+\mathbf{\Lambda}+\mathbf{S}_{CH}^{G}\right]\mathbf{q}=\mathbf{R}_{W}^{G}, \tag{3.27}$$

where $\mathbf{S}_{MA}^{E,G}$, $\mathbf{S}_{MA}^{I,G}$, $\mathbf{S}_{CW}^{G}$, and $\mathbf{R}_{W}^{G}$ are the interaction coefficients, which are defined as follows:

$$\mathbf{S}_{MA}^{E,G} = \mathrm{Re}\left\{\mathbf{\Psi}^{\mathrm{T}}\mathbf{S}_{D}^{E}\left(\mathbf{F}_{M}^{E} - \mathbf{F}_{Gn}\right)^{-1}\mathbf{F}_{G}\mathbf{\Psi}\right\} \quad : \text{ added mass matrix (external fluid),}$$

$$\mathbf{S}_{MA}^{I,G} = \mathbf{\Psi}^{\mathrm{T}}\mathbf{S}_{D}^{I}\boldsymbol{\gamma}\left(\omega^{2}\mathbf{I} - \mathbf{\Omega}\right)^{-1}\boldsymbol{\gamma}^{\mathrm{T}}\mathbf{F}_{W}^{I}\mathbf{\Psi} \quad : \text{ added mass matrix (internal fluid),}$$

$$\mathbf{S}_{CW}^{G} = -\omega \times \mathrm{Im}\left\{\mathbf{\Psi}^{\mathrm{T}}\mathbf{S}_{D}^{E}\left(\mathbf{F}_{M}^{E} - \mathbf{F}_{Gn}\right)^{-1}\mathbf{F}_{G}\mathbf{\Psi}\right\} \quad : \text{ radiated wave damping matrix,}$$

$$\mathbf{R}_{W}^{G} = j\omega\mathbf{\Psi}^{\mathrm{T}}\mathbf{S}_{D}^{E}\left(\mathbf{F}_{M}^{E} - \mathbf{F}_{Gn}\right)^{-1}4\pi\mathbf{R}_{I} \quad : \text{ wave exciting force vector.} \tag{3.28}$$

In this section, we finally remark on the solution procedures for the present and conventional formulations as depicted in Figure 3.5. In the present solution procedure, the displacement of the structure ($\mathbf{u}$) and the velocity potential of the external ($\mathbf{\Phi}_E$) and internal ($\mathbf{\Phi}_I$) fluids are obtained by solving the discrete coupled equations, and one additional step of a modal analysis can be optionally employed to reduce the number of degrees of freedom. The conventional solution procedure requires four solution steps. However, both procedures provide theoretically equivalent solutions and their solution efficiency is also similar.

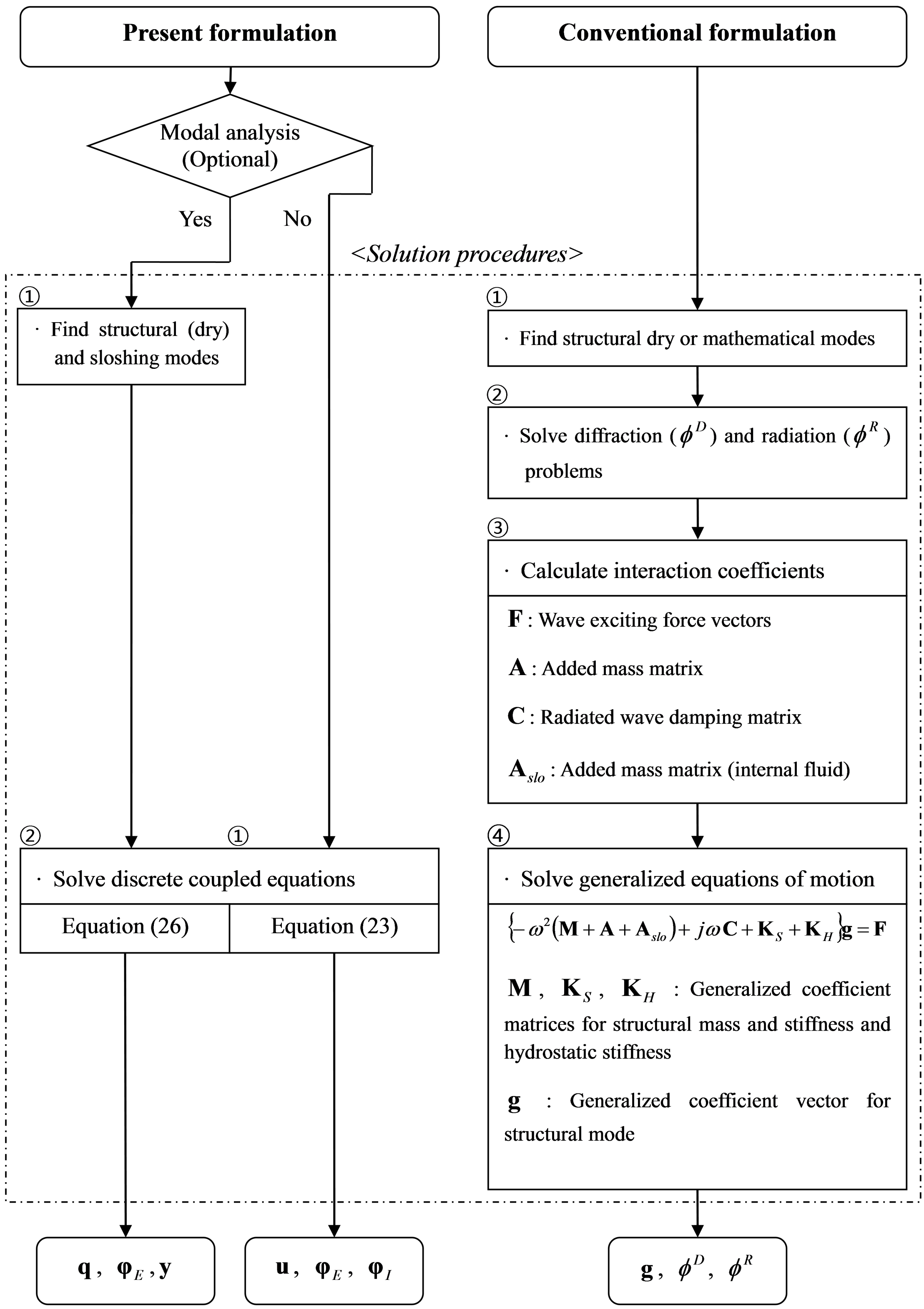

Figure 3.5: Solution procedures for the steady state hydrodynamic analysis in the present and conventional formulations.

3.4 Numerical tests

In this section, various numerical tests are presented for a 3D box barge model: free vibration analyses, a rigid body hydrodynamic analysis, and a hydroelastic analysis. The hydrostatic analysis is performed prior to the dynamic analysis to include the initial stress effect in the hydroelastic analysis. In the hydrostatic and hydrodynamic analyses, the reference configuration is assumed as the hydrostatic equilibrium state calculated for the rigid body case.

Figure 3.6(a) presents a 3D box barge with three liquid tanks (length L is 300m, width W is 50m, and height H is 30m) used in the numerical tests. The model consists of three parts: the bottom, side hulls (bow, stern, starboard and port), and four bulkheads. The thicknesses and material properties are listed in Table 3.1, and it is ensured that the draft d is 10m and the vertical center of gravity (COG) is -4m in the rigid body case. For simplicity, all three rectangular tanks (length L_T is 90m, width W is 50m, and height H is 30m) are designed to be the same and located from bow to stern in order. In the tanks, the density of the internal fluid ρ_I is 500 kg/m^3 and the filling height h_I is 10 m, which is measured from the bottom of the tanks. The density of the external fluid ρ_E is 1000kg/m^3 and the depth h_E is assumed to be infinite. Also, the gravitational acceleration g is 9.8m/sec^2. Three angles of incident waves ($\theta = 0°,\ 45°$ and $90°$) and angular frequencies ω from 0.2 to 1.2 rad/sec with a constant increment ($\Delta\omega = 0.01$ rad/sec) are considered.

The meshes used for the box barge, internal fluid, and external fluid are shown in Figure 3.6(b), (c), and (d). A four-node mixed interpolation of tensorial components (MITC) shell finite element [27, 28, 29, 30] is used for the floating structure, an eight-node brick element is used for the internal fluid in tanks, and a four-node boundary element is used for the external fluid.

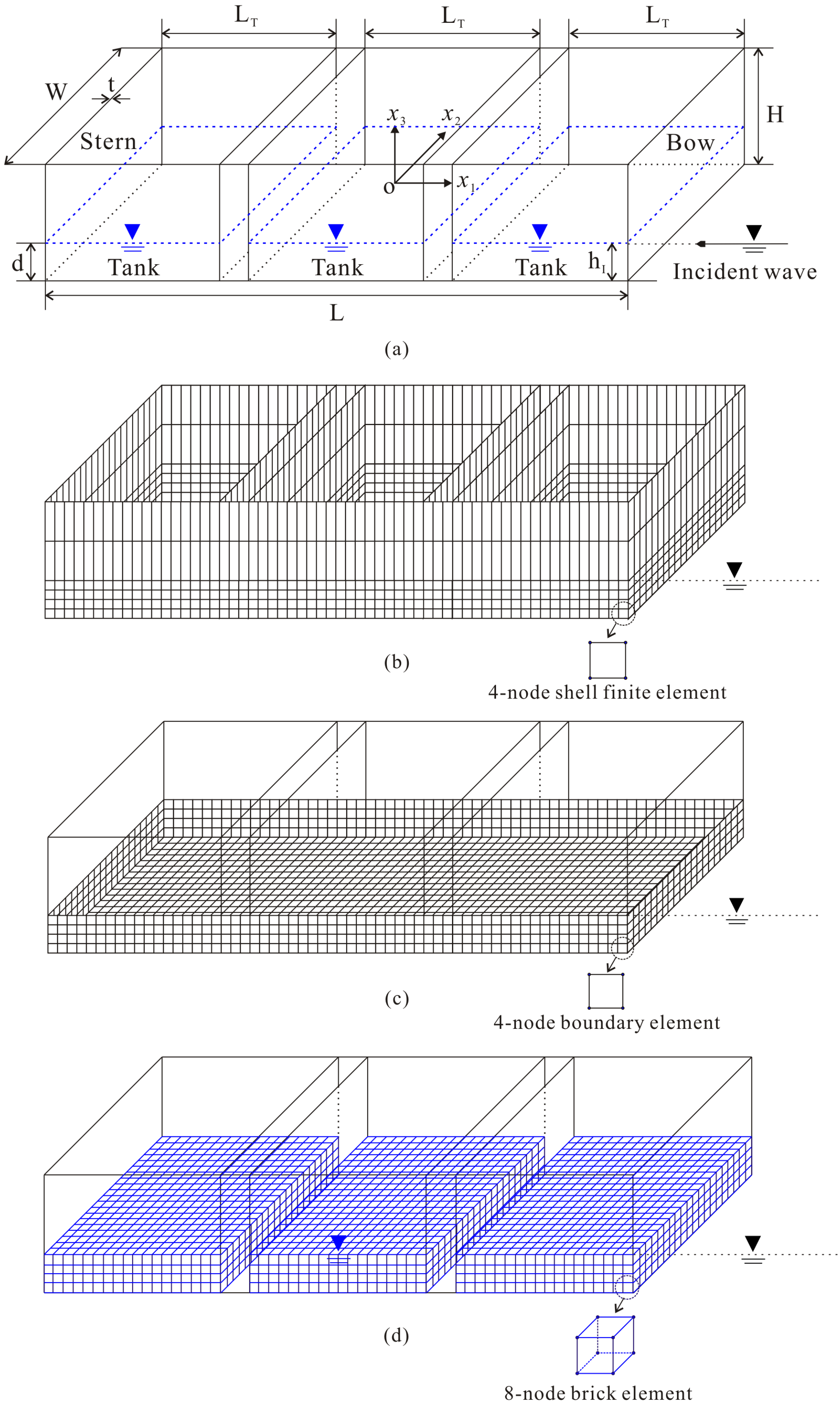

Figure 3.6: 3D box barge model: (a) overall description, (b) finite element mesh used for the box barge, (c) boundary element mesh used for the external fluid, and (d) finite element meshes used for the internal fluid.

Table 3.1: Material properties of the box barge model.

	Bottom	Side hulls	Bulkheads
Thickness t (m)	0.4	0.2	0.2
Density ρ_s (kg/m^3)	$15,000$	15,000	10,000
Young's modulus E (GPa)	2.0×10^{11}	2.0×10^{11}	1.0×10^{11}
Poisson's ratio ν	0.3	0.3	0.3

3.4.1 Free vibration analyses

Free vibration analyses of the box barge and the internal fluid are performed to obtain the natural frequencies and the mode shapes. The finite element model of the box barge is shown in Figure 3.6(b). The four elastic dry mode shapes of the box barge that correspond to the first four natural frequencies are presented in Figure 3.7. It is observed that the first mode shown in Figure 3.7(a) is the torsional mode.

For the internal fluid, the first eight free surface mode shapes and the corresponding natural frequencies (ω_i^N; i indicates the free surface mode number) computed here are illustrated in Figure 3.8 and Table 3.2. Figure 3.8(a), (c), and (f) are the first three longitudinal sloshing modes, (b) and (h) are the first two transverse sloshing modes, and the others are mixed sloshing modes. In Table 3.2, the computed natural frequencies of the present formulation are compared with the analytical solutions [32, 33] obtained by

$$\omega_{m,n}^A = \sqrt{g\ k_{m,n} \tanh k_{m,n} h_I}; \quad k_{m,n} = \pi \sqrt{\left(\frac{m}{L_T}\right)^2 + \left(\frac{n}{W}\right)^2}; \quad m, n = 0, 1, 2, ...;\ m + n \neq 0, \quad (3.29)$$

where the subscripts m and n denote the longitudinal and transverse directions, respectively, and $\omega_{m,n}^A$ is the analytical solution of the sloshing natural frequencies.

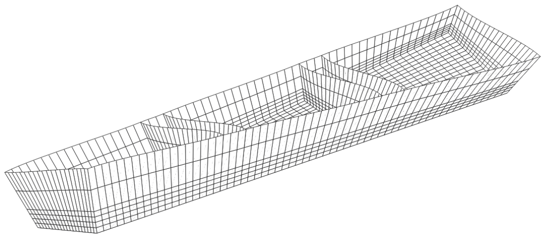

(a) 0.124 (rad/sec)

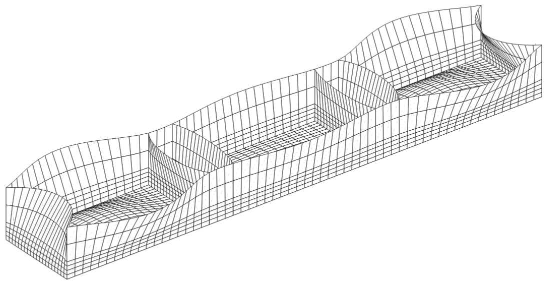

(b) 0. 546 (rad/sec)

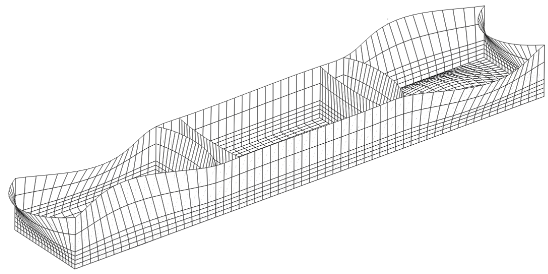

(c) 0.548 (rad/sec)

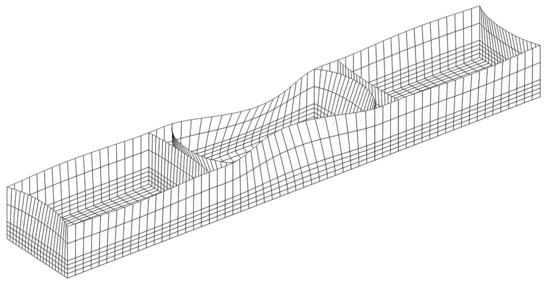

(d) 0.565 (rad/sec)

Figure 3.7: Mode shapes of the box barge.

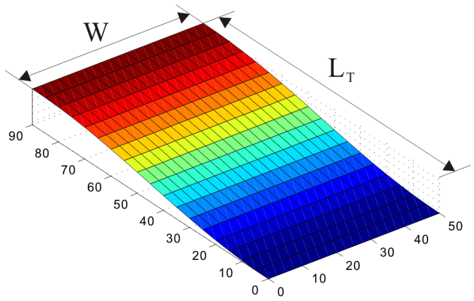

(a) Mode 1 (ω_1^N)

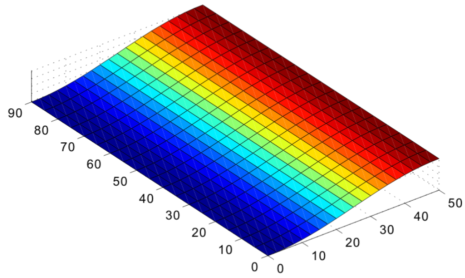

(b) Mode 2 (ω_2^N)

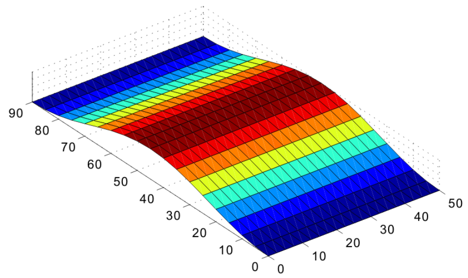

(c) Mode 3 (ω_3^N)

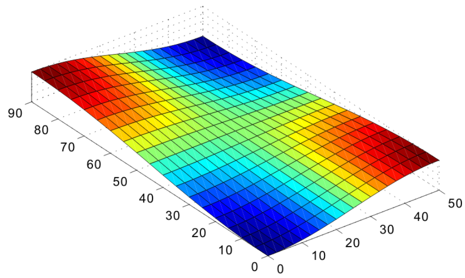

(d) Mode 4 (ω_4^N)

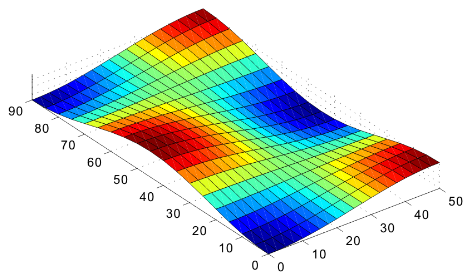

(e) Mode 5 (ω_5^N)

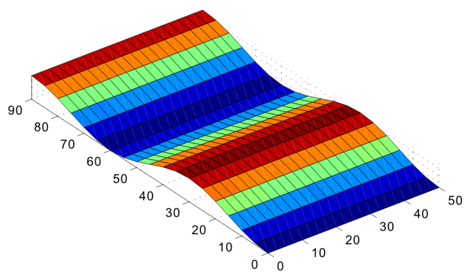

(f) Mode 6 (ω_6^N)

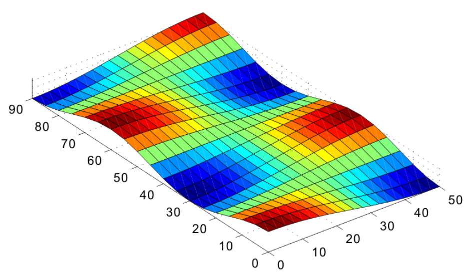

(g) Mode 7 (ω_7^N)

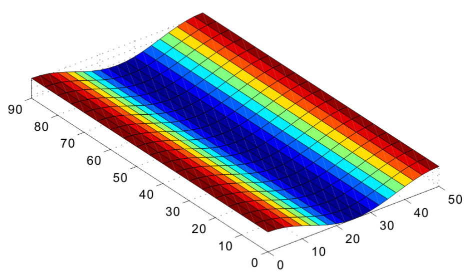

(h) Mode 8 (ω_8^N)

Figure 3.8: Computed free surface mode shapes and natural frequencies (ω_i^N) of the internal fluid.

Table 3.2: Numerical (ω_i^N) and analytical ($\omega_{m,n}^A$) results for the natural frequencies (rad/sec) of the internal fluid.

Numerical results (ω_i^N)	Analytical results ($\omega_{m,n}^A$)
0.339 (ω_1^N)	0.339 ($\omega_{1,0}^A$)
0.588 (ω_2^N)	0.586 ($\omega_{0,1}^A$)
0.646 (ω_3^N)	0.642 ($\omega_{2,0}^A$)
0.662 (ω_4^N)	0.659 ($\omega_{1,1}^A$)
0.827 (ω_5^N)	0.822 ($\omega_{2,1}^A$)
0.905 (ω_6^N)	0.895 ($\omega_{3,0}^A$)
1.012 (ω_7^N)	1.003 ($\omega_{3,1}^A$)
1.038 (ω_8^N)	1.023 ($\omega_{0,2}^A$)

3.4.2 Rigid body hydrodynamic analysis

We perform a rigid body hydrodynamic analysis and the results are compared with the results of WAMIT [58]. In WAMIT, a higher-order method (using the 4th-order B-spline functions) is employed for the external and internal fluids. For the spatial discretization, 60, 20, and 4 panels are used for the box barge in the length, width, and depth directions and 18, 20, and 4 panels are used for each internal fluid in the three tanks.

Figures 3.9 and 3.10 show the response amplitude operators (RAOs) when the incident wave angles θ are $0°$, $90°$, and $45°$. In the figures, q_i is the generalized coordinates defined with respect to the center of floatation of the box barge. The subscript i varies from 1 to 6, which denote 6 rigid body motions, i.e., surge, sway, heave, roll, pitch, and yaw motions.

All the results of the present formulation and WAMIT are in good agreement. However, unlike the higher-order method used in WAMIT, a bilinear interpolation is employed in the present discretization and thus small differences can be observed near the resonance points.

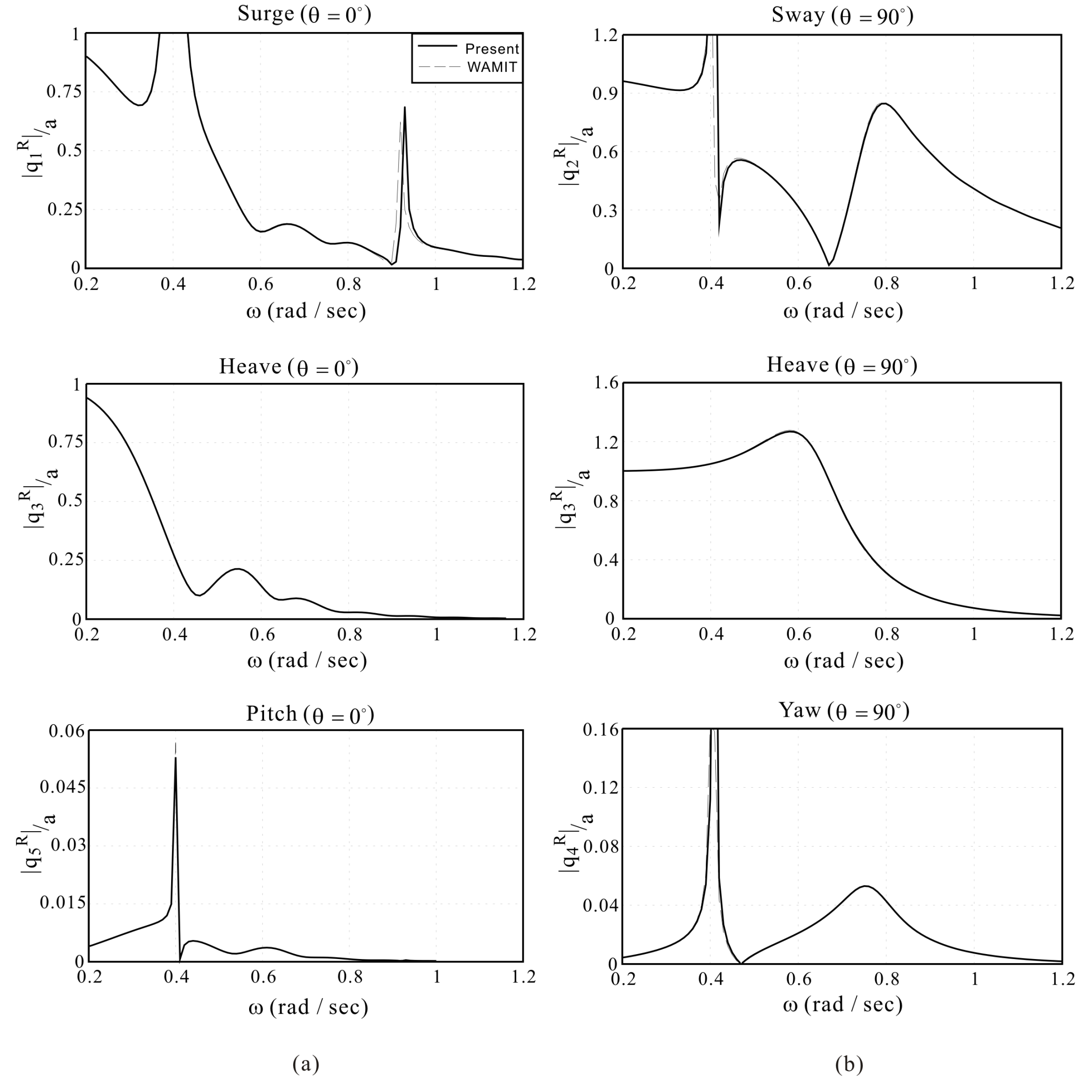

Figure 3.9: RAOs of rigid body motions of the box barge: (a) surge, heave, and pitch motions when $\theta = 0°$, and (b) sway, heave, and roll motions when $\theta = 90°$.

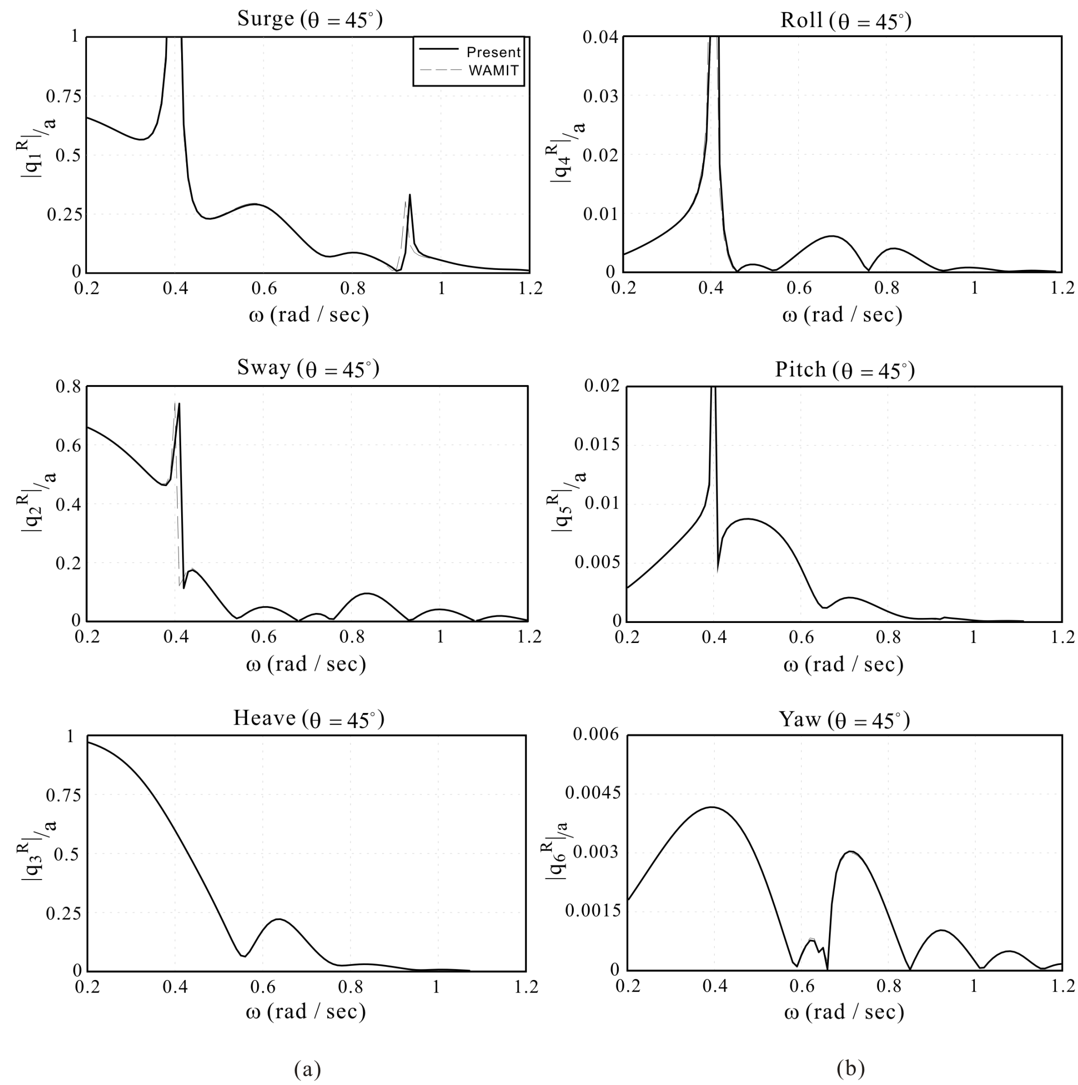

Figure 3.10: RAOs of rigid body motions of the box barge when $\theta = 45°$: (a) surge, sway, and heave, and (b) roll, pitch, and yaw motions.

3.4.3 Hydroelastic analysis

The hydroelastic analysis of the box barge model is performed with the mode superposition method for efficient computation. The dry modes of the box barge and the sloshing modes of the internal fluid that correspond to the natural frequencies up to $\sqrt{1000}$rad/sec are contained for the reduced equation and the generalized coordinates are constructed with respect to the center of floatation of the box barge.

As well known, the hydrostatic stiffness plays an important role in hydrodynamic analysis of floating structures in both rigid and elastic body cases. In particular, the geometric stiffness term $\mathbf{S}_{KN}$ in Equation 3.20c should be carefully considered in hydroelastic analysis because Equation 3.20c requires the initial stress field ${}^{0}\sigma_{ij}$ due to hydrostatic pressures. Therefore, hydrostatic analysis is prerequisite for hydroelastic analysis.

Figure 3.11 shows the vertical displacements calculated in both rigid and elastic body cases. In particular, it is observed that, in the elastic cases, quite different results are obtained when the initial stress effect is not considered. Table 3.3 shows the differences in hydrostatic stiffness terms. This comparison study demonstrates the importance of the initial stress in hydroelastic analysis. However, the differences would be small for relatively rigid floating structures.

Figure 3.11, there are peaks which arise from many different resonance sources (e.g. floating structure, sloshing, and external waves) and their combinations. It is a hard task to identify the sources of peaks, in particular, when multiple sloshing tanks are considered.

Finally, some diagonal components of the external and internal added masses $S^{E,G}_{MA,ij}$ and $S^{I,G}_{MA,ij}$ calculated using Equation 3.28 are presented in Figures 3.12 and 3.13. In contrast to the results in Figure 3.12, resonance phenomena can be found in Figure 3.13.

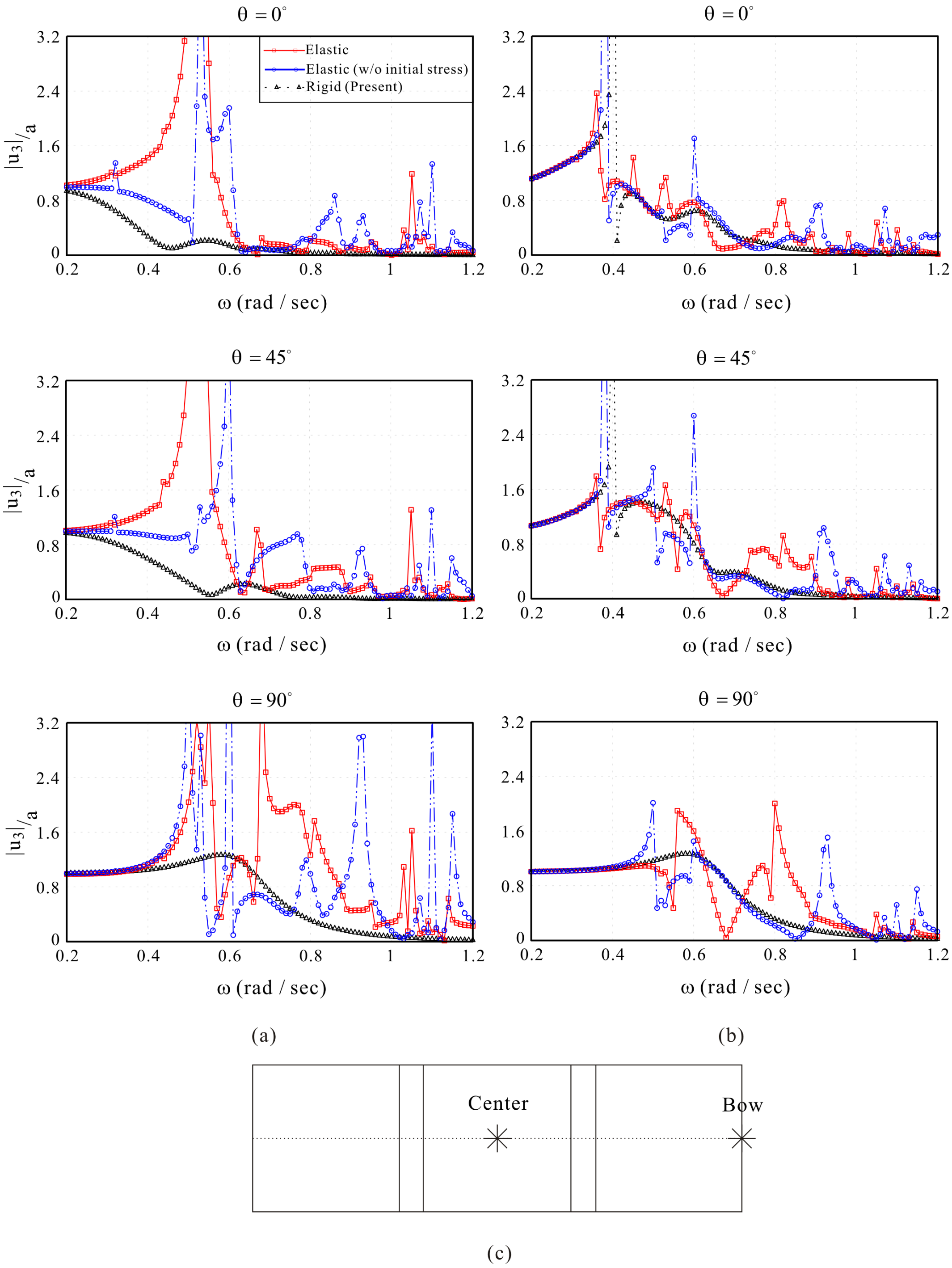

Figure 3.11: RAOs of the vertical displacements ($|u_3/a$) at the bottom of the box barge: (a) center, (b) bow, and (c) corresponding measuring points.

Table 3.3: Comparison of the hydrostatic stiffness terms. The subscripts i and j vary from 1 to 10; 1,2,...,6, denote the values corresponding to the six rigid body motions and 7,8,9,10 denote the values corresponding to the first four elastic modes shown in Figures 3.6.

(i,j)	$S^G_{CH,ij}$	$S^G_{CH,ij}$ (w/o initial stress)
(3,3)	0.98000	0.98000
(4,4)	0.42365	0.69250
(5,5)	0.85619	0.87069
(7,7)	0.41157	0.61645
(8,8)	0.54137	0.03300
(9,9)	0.46628	0.03144
(10,10)	1.81060	0.03505

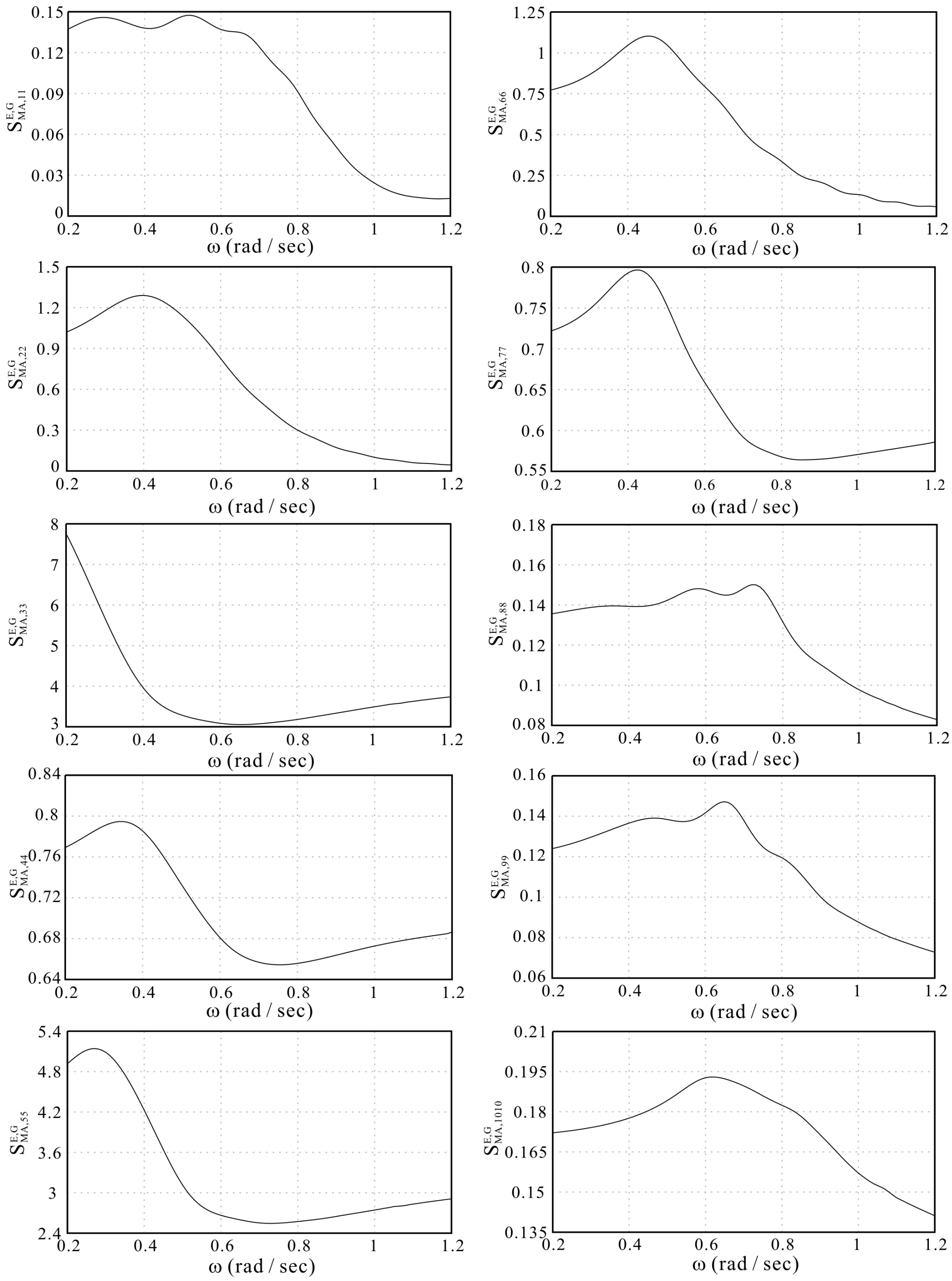

Figure 3.12: External added mass coefficients: for the rigid modes ($S^{E,G}_{MA,11} \sim S^{E,G}_{MA,66}$) and for the elastic modes ($S^{E,G}_{MA,77} \sim S^{E,G}_{MA,1010}$).

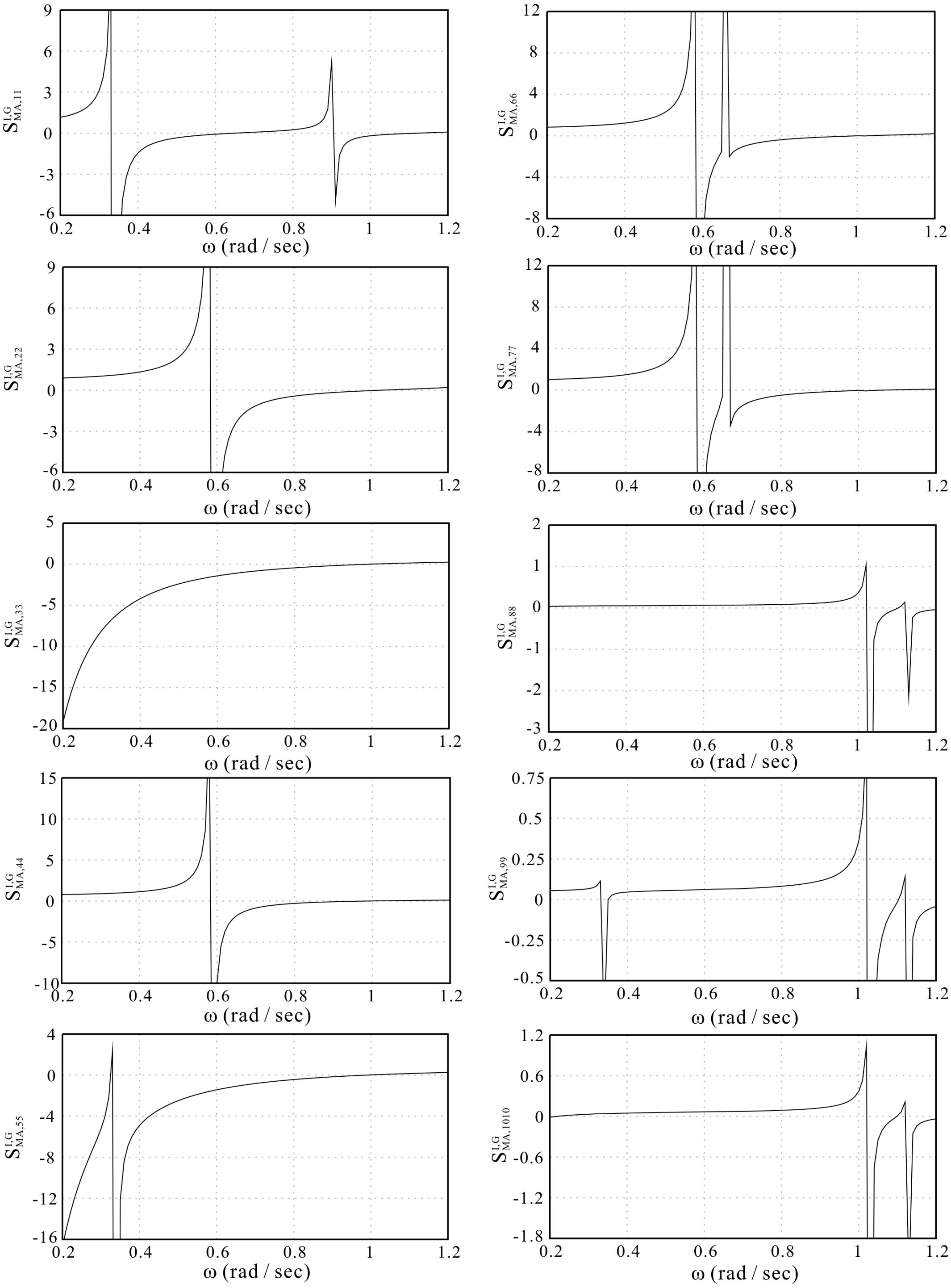

Figure 3.13: Internal added mass coefficients: for the rigid modes ($S^{I,G}_{MA,11} \sim S^{I,G}_{MA,66}$) and for the elastic modes ($S^{I,G}_{MA,77} \sim S^{I,G}_{MA,1010}$).

3.5 Hydroelastic experiments

To verify the hydroelastic analysis procedure developed in this study, 3D hydroelastic experiments were conducted using a simplified FPU model with three rectangular liquid tanks. In the following, the hydroelastic experiment setup and the numerical model are described. The experimental results are then compared with the numerical results.

3.5.1 Experimental setup

In this section, we present the overall description of the 3D hydroelastic experiment, including the experimental conditions, structural model, mooring method, wave conditions, and measuring devices.

As shown in Figure 3.14, the hydroelastic experiments of the FPU model are carried out in an ocean basin and the water depth (h_E) is set to 1.5m. The FPU model is made of polycarbonate. Details of the FPU model are presented in Figure 3.15 and Table 3.4. The lowest elastic mode of the experimental model is a twisting mode ($\omega_n^{twisting}$=15.66 rad/sec) and the first twenty natural sloshing frequencies are within a range of 4.95 to 19.22 rad/sec.

Figure 3.16 illustrates the overall experimental setup. In order to measure the incident wave frequency (ω), wave length (λ), and amplitude (a), one wave probe is installed at the free surface, located a distance of 1.5m in front of the test model. The wave probe measures the wave elevation during the experiments. The three translations of the floating structure are then measured through four motion capture cameras with infrared reflective (IR) markers. Figure 3.16(a) shows the positions of the six IR markers attached on the FPU model.

The incident waves belong to the range of the linear wave theory in deep water condition ($2a/h_E < 1.0$ and $h_E/\lambda < 1.0$) [59]. The drift of the FPU model due to the incident wave was prevented by mooring the structure upward with four strings. Since the strings should prevent the drift without restraining surge, sway, and heave motions, a small amount of tension is introduced such that the strings are horizontally connected to the structure. That is, the connection angle between the strings and the structure is almost 180°, see Figure 3.16(c).

We then performed the 3D hydroelastic experiments considering eight wave frequencies (ω= 4.3, 5.3, 6.2, 7.4, 8.4 9.5, 10.2, 12.2, and 15 rad/sec) and three different incident wave angles ($\theta = 0°$, 45°, and 90°).

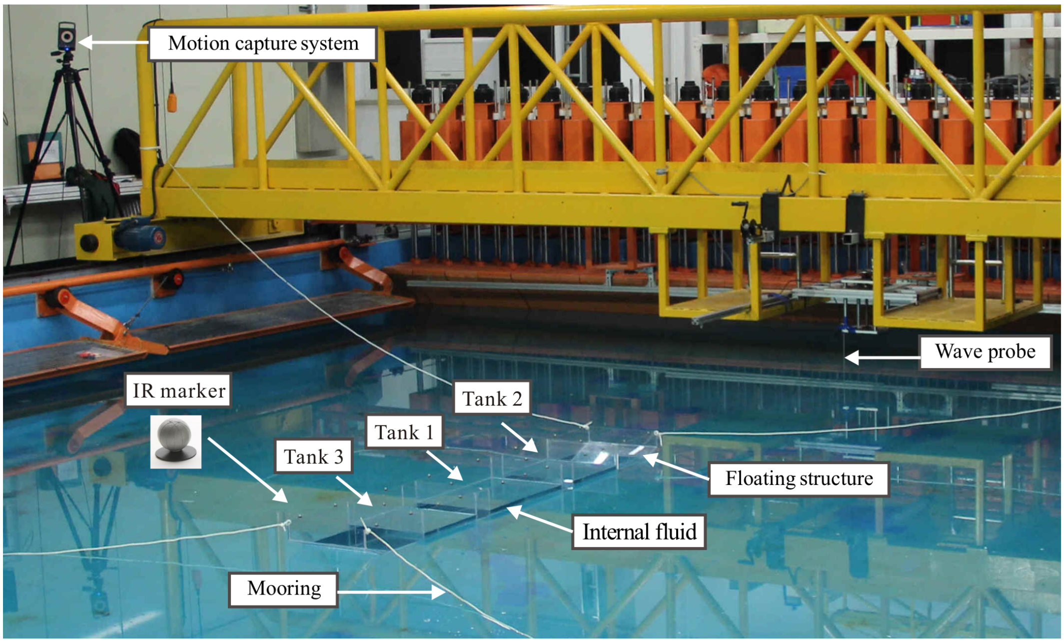

Figure 3.14: Hydroelastic experiment of the FPU model with three liquid tanks in an ocean basin (15m × 10m × 1.5m).

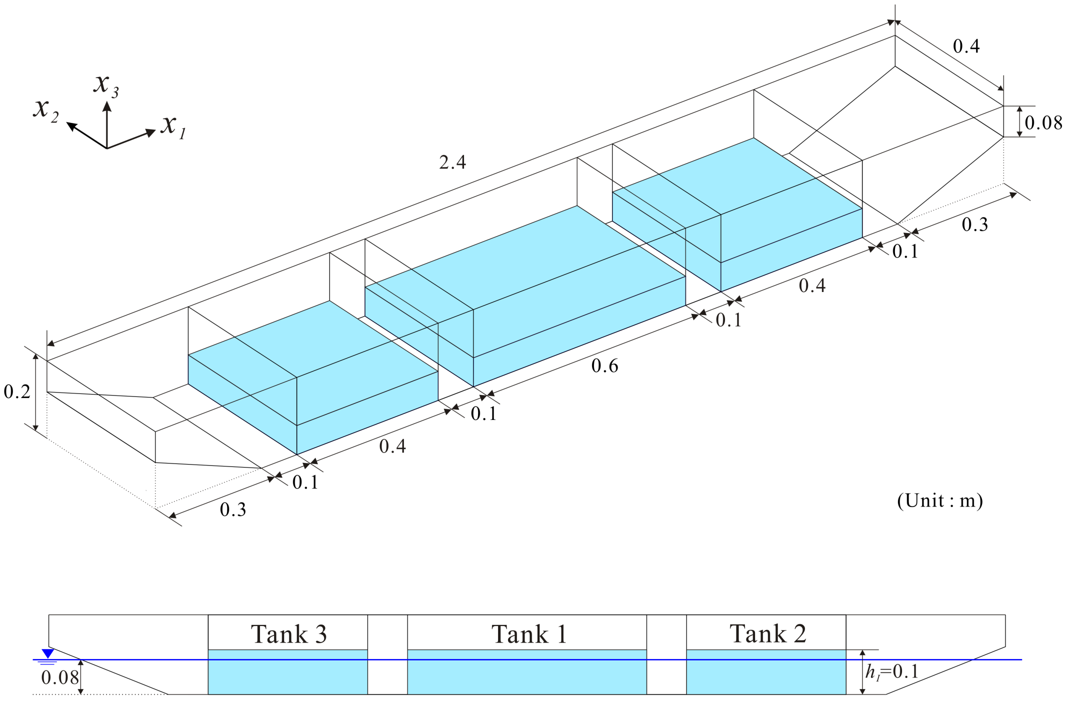

Figure 3.15: FPU model.

Table 3.4: Details of the FPU model.

Length (L)	2.4 m
Width (W)	0.4 m
Height (H)	0.2 m
Thickness (t)	0.003 m
Draft (d)	0.08 m
Young's modulus (E)	2 GPa
Tank1 ($L_t \times W \times h_I$)	$0.6 \times 0.4 \times 0.1$ m
Tank2 and 3 ($L_t \times W \times h_I$)	$0.4 \times 0.4 \times 0.1$ m

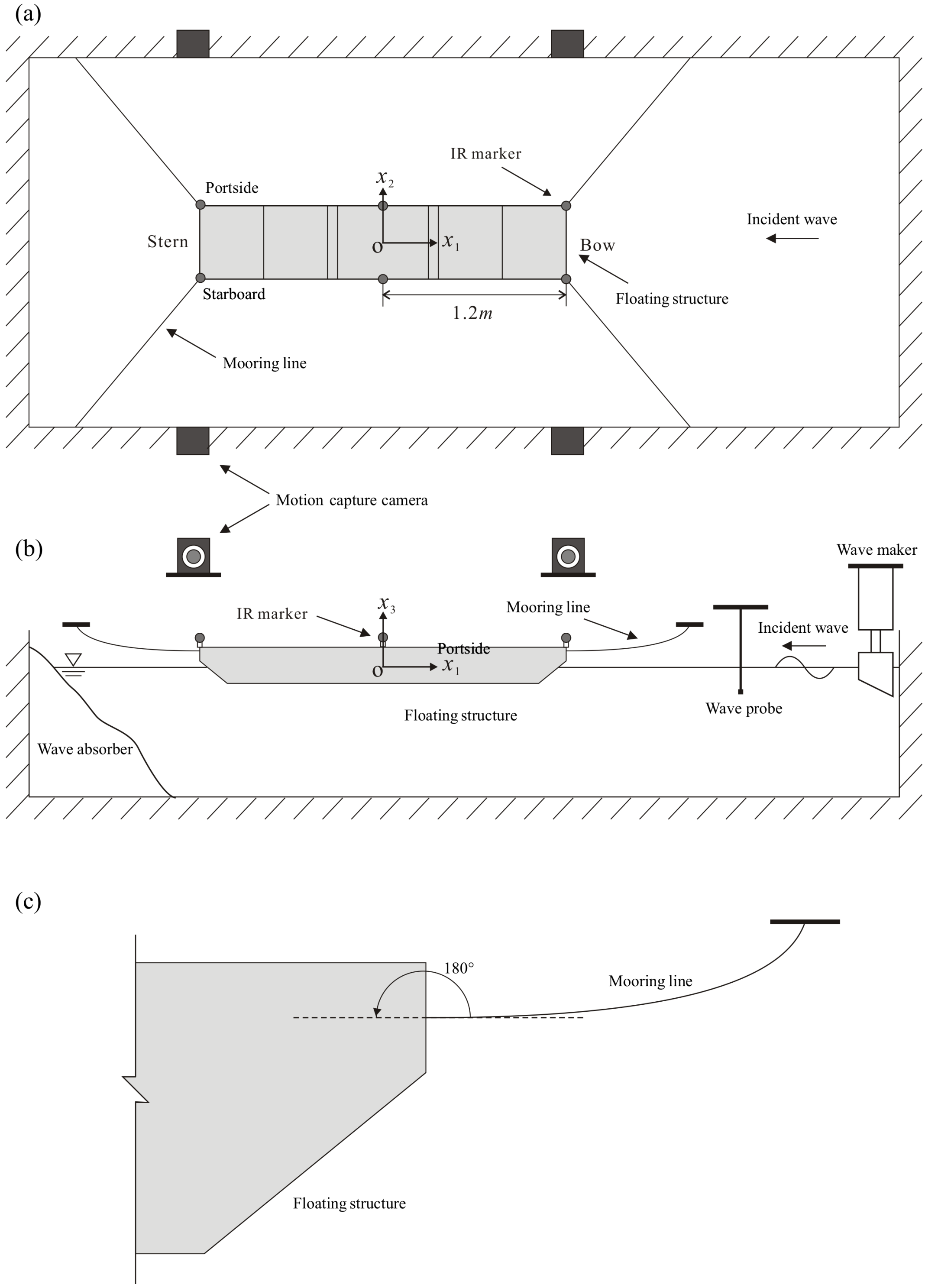

Figure 3.16: A schematic of the experimental setup: (a) top view, (b) front view, (c) mooring lines.

3.5.2 Comparison between experimental and numerical results

Rigid body hydrodynamic and hydroelastic analyses are conducted using the numerical method developed in this study. Figure 3.17 shows the meshes used for the FPU model with three rectangular tanks. The FPU model and internal fluids in tanks are discretized by 5,200 shell elements and 7,000 brick elements, respectively. The external wet surface is discretized by 2,680 boundary elements.

Figures 3.18 and 3.19 show the RAOs of structural displacements (u_1, u_2 and u_3) for three incident wave angles ($\theta = 0°$, $45°$, and $90°$). The results of the rigid body hydrodynamic and hydroelastic analyses are compared with the experimental results. It is observed that the experimental results are in good agreement with the results of the hydroelastic analysis, especially, when the initial stress effect is considered. Since artificial damping is not considered in the numerical analyses, the numerical results over-predict the peaks. In the heading angle ($\theta = 0°$), the FPU model moves like a rigid body in both experimental and numerical results due to its relatively large overall bending rigidity.

Figures 3.20 presents the RAOs of the modal coordinate (q_7) and phase angle calculated, which correspond to the first elastic mode ($\mathbf{\Psi}_7$, twisting mode) when the incident wave angle is 45°. Figures 3.21(a) shows the twisting angles of the FPU model measured in the numerical and experimental results. The largest twisting angle ($\theta_{twisting}$) is observed at 7.4 rad/sec in the experimental results.

In Figures 3.22, we finally present some snapshots of free surface profiles, shape of structural deformation and the corresponding structural displacements when the wave frequency is 7.4 rad/sec. It is observed that the sloshing motion is not beyond the linear potential theory and the tendency of free surface profiles in Figures 3.22(a) agrees well with the numerical results.

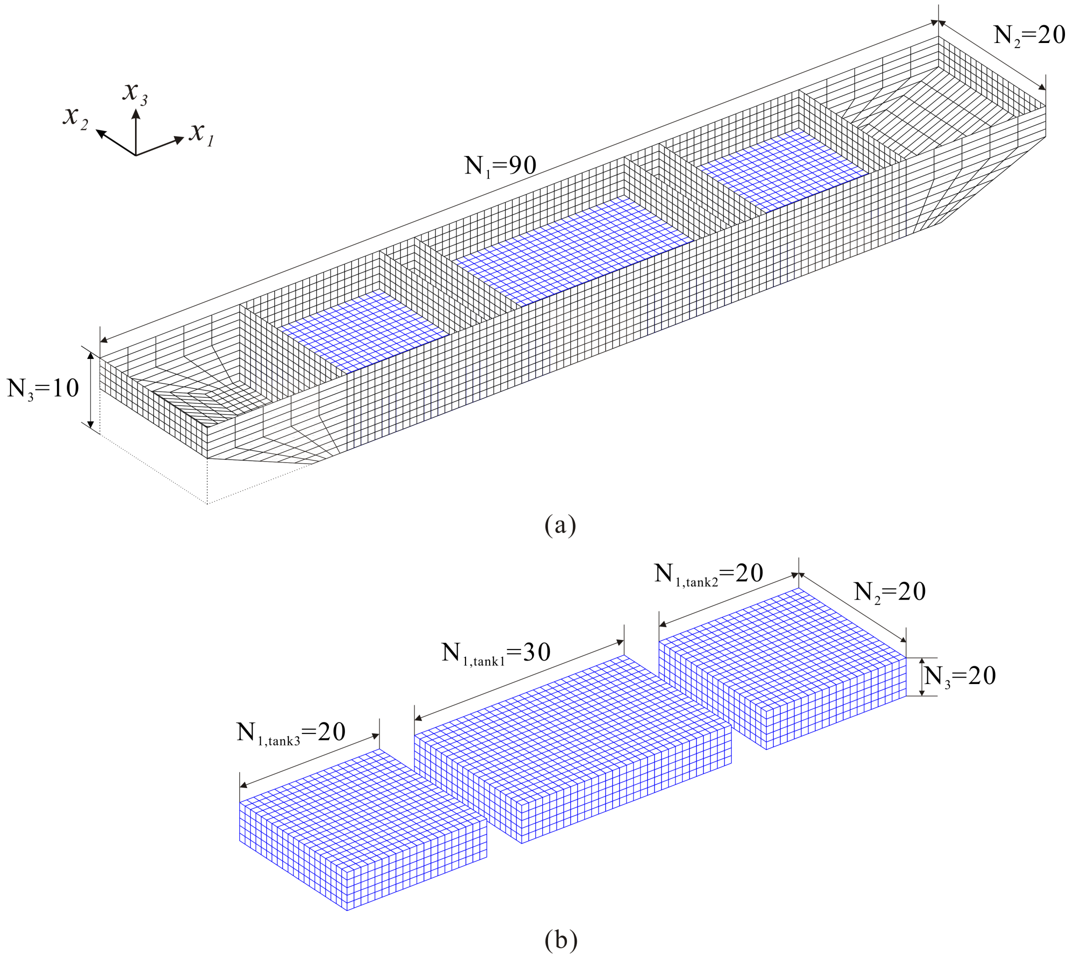

Figure 3.17: Meshes used for (a) FPU with three rectangular tanks and (b) internal fluid.

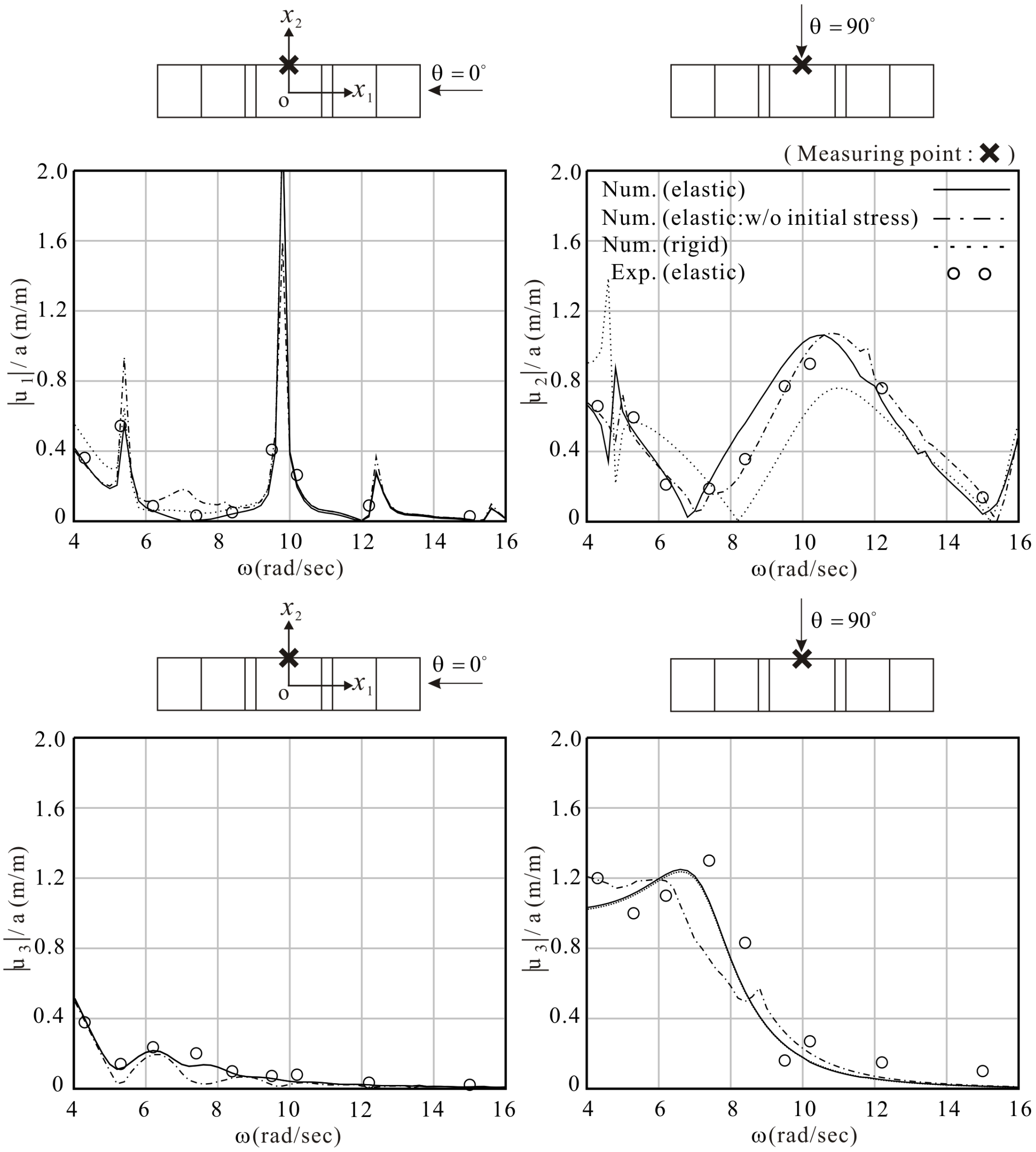

Figure 3.18: RAOs of the displacements of the FPU model for two incident wave angles (θ = 0° and θ = 90°).

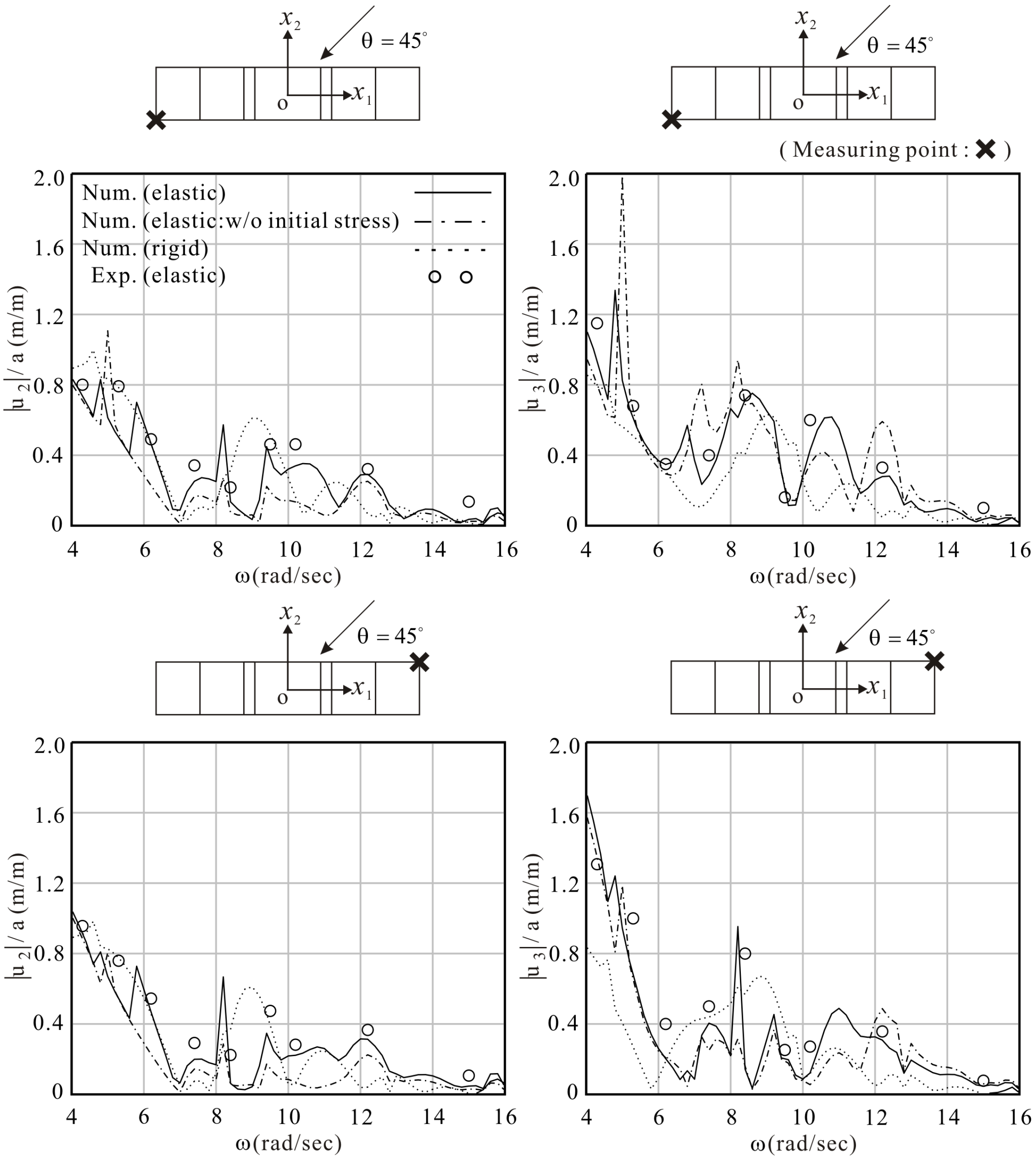

Figure 3.19: RAOs of the displacements of the FPU model (θ = 45°).

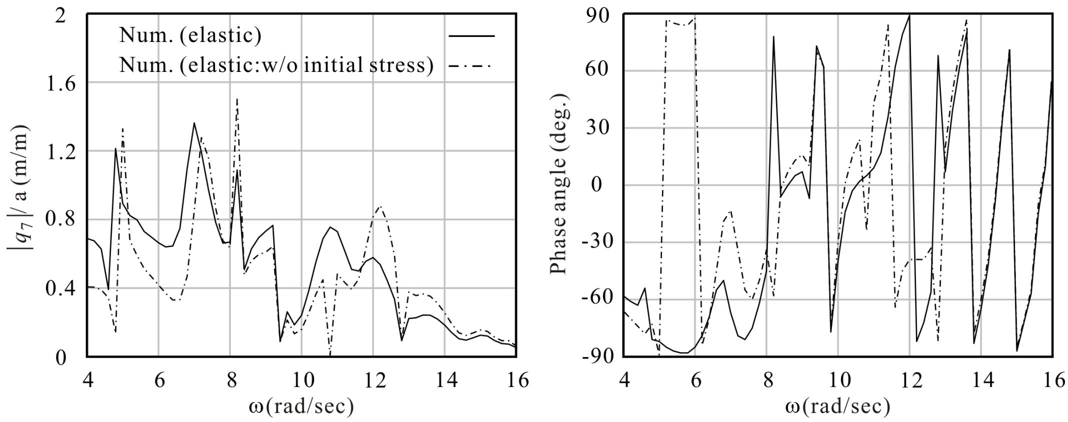

(a)

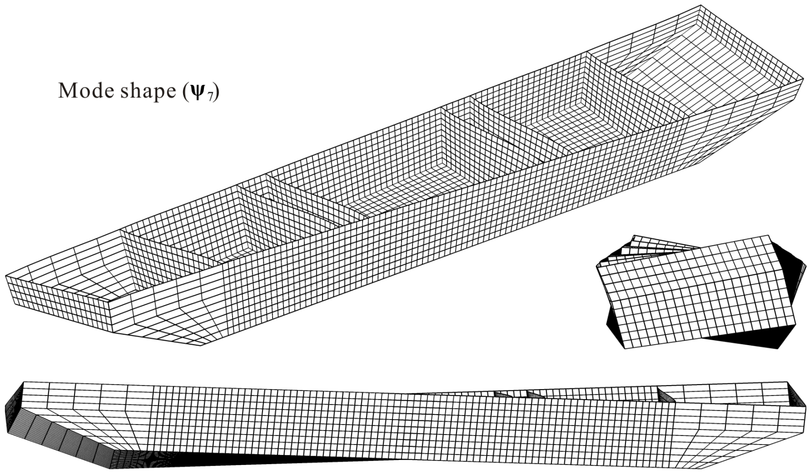

(b)

Figure 3.20: Modal responses calculated: (a) RAOs of the modal coordinate (q_7/a) and phase angle (θ), and (b) mode shape ($\mathbf{\Psi}_7$).

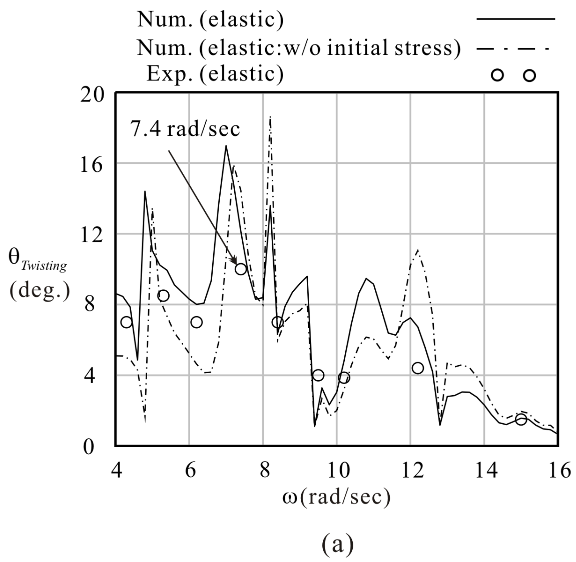

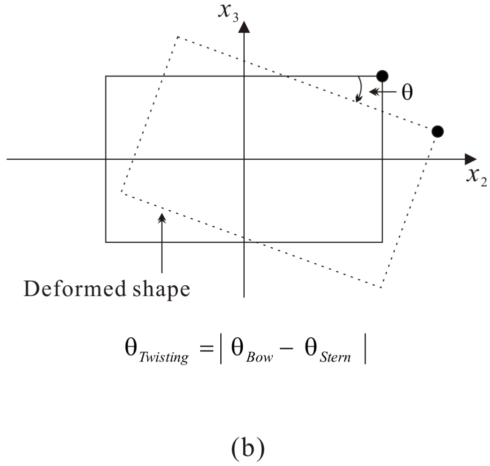

Figure 3.21: Twisting angle ($\theta_{twisting}$) of the FPU model ($\theta = 45°$ and wave amplitude ($a = 0.03$ m)): (a) comparison between numerical and experimental results and (b) definition of twisting angle.

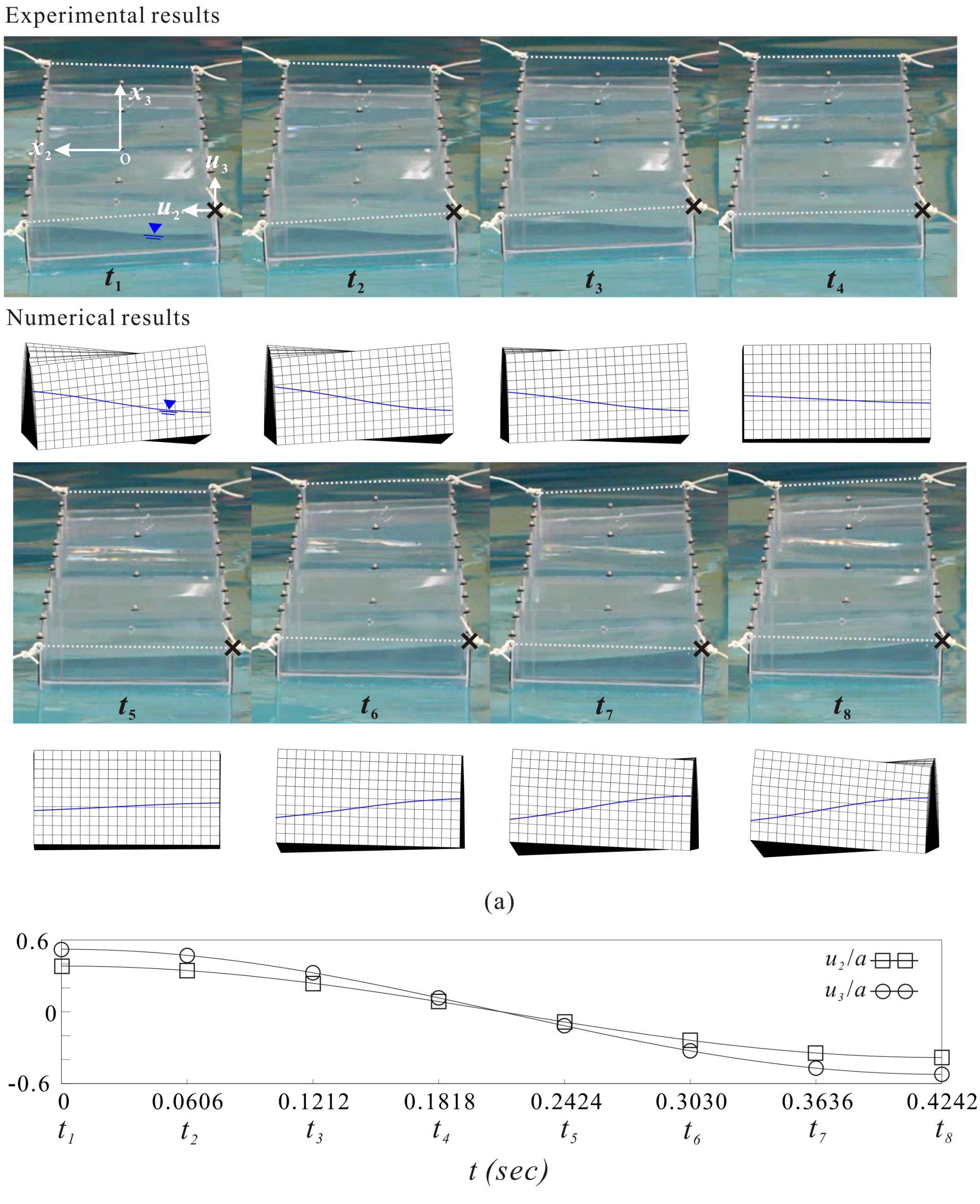

Figure 3.22: Snapshots of hydroelastic response (θ = 45°, ω=7.4 rad/sec, ×: the measuring point of structural displacements): (a) experiment and numerical results, and (b) structural displacements (u_2/a and u_3/a).

3.6 Summary

In this chapter, we presented a mathematical formulation and a numerical method for a hydroelastic analysis of floating structures with liquid tanks in the frequency domain, in which the direct-coupling method was employed to couple structural motions, sloshing, and water waves. The extended boundary integral equation was adopted in order to avoid the irregular frequency problem. The proposed formulation includes all the terms required for a linear hydroelastic analysis of floating structures with liquid tanks.

The proposed formulation was verified through a comparison with the analysis results of WAMIT in a rigid body hydrodynamic analysis. The importance of the initial stress was demonstrated through a comparative hydroelastic analysis. In addition, 3D hydroelastic experiments were performed for a FPU model. We also simulated the hydroelastic behavior of the FPU model. The numerical results were compared with experimental results and good agreement between the results was observed.

In future works, it will be valuable to extend the present direct coupled formulation to nonlinear hydroelastic analyses, in which we could deal with the large motions of floating structures and fluid and wet-surface change. Also, it will be an interesting study to identify resonance sources in hydroelastic analysis of floating structures with liquid tanks.

Chapter 4. Conclusion

The objectives in this work were to develop the numerical methods to calculate the hydrostatic equilibrium of 3D flexible floating structures, by which accurate draft and stress fields of structures in collaborate with the development of numerical method for 3D hydroelastic analysis of floating structure with liquid sloshing.

In Chapter 2, a numerical method for a nonlinear hydrostatic analysis of flexible floating structures was proposed. The incremental equilibrium equation for rigid and flexible (elastic) floating bodies was derived using the updated Lagrangian formulation, which is discretized using the finite element procedure. An effective numerical integration technique was developed to treat the significant wet surface change and thus the non-matching mesh problem is resolved without re-meshing. The feasibility of the proposed numerical procedure was demonstrated through various hydrostatic problems considering both rigid and flexible body cases. The importance of the nonlinear solution procedure in the stress analysis of flexible floating structures was discussed. The configurations in hydrostatic equilibrium and the corresponding stress distributions were presented for various floating and loading conditions. The proposed numerical method can be easily used for the stress analysis of damaged ships and offshore platforms with various loading conditions. Moreover, it can be extended to the transient analysis of flexible floating structures in flooded conditions by considering the inertia forces and internal free surface effect.

In Chapter 3, a mathematical formulation and a numerical method for a hydroelastic analysis of floating structures with liquid tanks in the frequency domain, in which the direct-coupling method was employed to couple structural motions, sloshing, and water waves was proposed. The extended boundary integral equation was adopted in order to avoid the irregular frequency problem. The proposed formulation includes all the terms required for a linear hydroelastic analysis of floating structures with liquid tanks. The proposed formulation was verified through a comparison with the analysis results of WAMIT in a rigid body hydrodynamic analysis. The importance of the initial stress was demonstrated through a comparative hydroelastic analysis. In addition, 3D hydroelastic experiments were performed for a FPU model. We also simulated the hydroelastic behavior of the FPU model. The numerical results were compared with experimental results and good agreement between the results was observed. In future works, it will be valuable to extend the present direct coupled formulation to nonlinear hydroelastic analyses, in which we could deal with the large motions of floating structures and fluid and wet-surface change. Also, it will be an interesting study to identify resonance sources in hydroelastic analysis of floating structures with liquid tanks.

As an extension of this work, we recommend the following future works:

- In Chapter 2, the proposed numerical method can be easily used for the stress analysis of damaged ships and offshore platforms with various loading conditions. Moreover, it can be extended to the transient analysis of flexible floating structures in flooded conditions by considering the inertia forces and internal free surface effect.
- In Chapter 3, it will be valuable to extend the present direct coupled formulation to nonlinear hydroelastic analyses, in which we could deal with the large motions of floating structures and fluid and wet-surface change. Also, it will be an interesting study to identify resonance sources in hydroelastic analysis of floating structures with liquid tanks.

References

[1] Faltinsen OM. *Sea loads on ships and offshore structures.* Vol. 1. Cambridge: Cambridge University Press; 1993.

[2] Witz JA, Patel MH. A pressure integration technique for hydrostatic analysis. *Royal Institution of Naval Architects Transactions* 1985;127:285-294.

[3] Schalck S, Baatrup J. Hydrostatic stability calculations by pressure integration. *Ocean engineering* 1990;17(1):155-169.

[4] Calabrese F, Mancarella L, Zizzari AA, Corallo A. A Multidisciplinary Method for Evaluating Ship Stability. *Journal of Shipping and Ocean Engineering* 2012;2(6):321.

[5] Zizzari AA, Calabrese F, Indiveri G, Coraddu A, Villa D. A Comparative Study on Different Approaches to Evaluate Ship Equilibrium Point. *In: Proc of World Academy of Science, Engineering and Technology* 2013;73:625.

[6] Santos TA, Guedes Soares C. Ro-ro ship damage stability calculations using the pressure integration technique. *International shipbuilding progress* 2001;48(2):169-188.

[7] Tarafder MS, Khalil GM. Calculation of ship sinkage and trim in deep water using a potential based panel method. *International Journal of Applied Mechanics and Engineering* 2006;11(2):401-414.

[8] Yang C, Löhner R. Calculation of ship sinkage and trim using a finite element method and unstructured grids. *International Journal of Computational Fluid Dynamics* 2002;16(3):217-227.

[9] Chandrasekaran S, Chandak NR, Anupam G. Stability analysis of TLP tethers. *Ocean Engineering* 2006;33(3):471-482.

[10] Chandrasekaran S, Chandak NR, Anupam G. Stability analysis of TLP tethers. *Ocean Engineering* 2006;33(3):471-482.

[11] Huang LL, Riggs HR. The hydrostatic stiffness of flexible floating structures for linear hydroelasticity. *Mar Struct* 2000;13:91-106.

[12] Riggs HR. Comparison of formulations for the hydrostatic stiffness of flexible structures. *J Offshore Mech Arct Eng* 2009;131(2), 024501.

[13] Kashiwagi M. A new direct method for calculating hydroelastic deflection of a very large floating structure in waves. *In: Proc of 13th workshop on water wave and floating bodies*. 1998.

[14] Taylor RE. Hydroelastic analysis of plates and some approximations. *J Eng Math* 2007;58:267-278.

[15] Khabakhpasheva TI, Korobkin AA. Hydroelastic behaviour of compound floating plate in waves. *J Eng Math* 2002;44:21-40.

[16] Wang CD, Meylan MH. A higher-order-coupled boundary element and finite element method for the wave forcing of a floating elastic plate. *J Fluid Struct* 2004;19:557-572.

[17] Yoon JS, Cho SP, Jiwinangun RG, Lee PS. Hydroelastic analysis of floating plates with multiple hinge connections in regular waves. *Mar Struct* 2014;36:65-87.

[18] Kim JG, Cho S, Kim KT, Lee PS. Hydroelastic design contour for the preliminary design of very large floating structures. *Ocean Eng* 2014;78:112-123.

[19] Watanabe E, Utsunomiya T, Wang CM. Hydroelastic analysis of pontoon-type VLFS: a literature survey. *Engineering structures* 2004;26(2):245-256.

[20] Kim Y, Kim KH, Kim Y. Analysis of Hydroelasticity of Floating Shiplike Structure in Time Domain Using a Fully Coupled Hybrid BEM-FEM. *Journal of Ship Research* 2009;53(1):31-47.

[21] Kim Y, Kim KH, Kim JH, Kim T, Seo MG, Kim Y. Time-domain analysis of nonlinear motion responses and structural loads on ships and offshore structures: development of WISH programs. *International Journal of Naval Architecture and Ocean Engineering* 2011;3(1):37-52.

[22] Rodrigues JM, Guedes Soares C. Exact pressure integrations on submerged bodies in waves using a quadtree adaptive mesh algorithm. *International Journal for Numerical Methods in Fluids* 2014;76(10):632-652.

[23] Dommermuth DG, Sussman M, Beck RF, O'Shea TT, Wyatt DC, Olson K, MacNeice P. The numerical simulation of ship waves using cartesian grid methods with adaptive mesh refinement. *In: Proceedings of the 25th ONR Symposium on Naval Hydrodynamics* 2004, Canada.

[24] Vavourakis V, Loukidis D, Charmpis DC, Papanastasiou P. Assessment of remeshing and remapping strategies for large deformation elastoplastic Finite Element analysis. *Comput Struct* 2013;114:133-146.

[25] Bathe KJ. *Finite element procedures.* New Jersey, Prentice Hall: Englewood Cliffs, 1996.

[26] Bathe KJ, Ramm E, Wilson EL. Finite element formulations for large deformation dynamic analysis. *Int J Numer Meth Eng* 1975;9(2):353-386.

[27] Lee Y, Lee PS, Bathe KJ. The MITC3+ shell finite element and its performance. *Comput Struct* 2014;138:12-23.

[28] Lee YG, Yoon KH, Lee PS. Improving the MITC3 shell finite element by using the Hellinger-Reissner principle. *Comput Struct* 2012;110-111:93-106.

[29] Jeon HM, Lee PS, Bathe KJ. The MITC3 shell finite element enriched by interpolation covers. *Comput Struct* 2013;134:128-42.

[30] Jeon HM, Lee Y, Lee PS, Bathe KJ. The MITC3+ shell element in geometric nonlinear analysis. *Comput Struct* 2015;146:91-104.

[31] Solutions, DRS Defense. *"ORCA3D User Manual."* (2011).

[32] Faltinsen OM, Timokha AN. *Sloshing.* Cambridge: Cambridge University Press; 2009.

[33] Ibrahim RA. *Liquid sloshing dynamics: theory and applications.* Cambridge: Cambridge University Press; 2005.

[34] Rognebakke OF, Faltinsen OM. Coupling of sloshing and ship motions. *J Ship Res* 2003;47:208-221.

[35] Lee D, Jo G, Kim Y, Choi H, Faltinsen OM. The effect of sloshing on the sway motions of 2D rectangular cylinders in regular waves. *J Mar Sci Technol* 2011;16:323-330.

[36] Molin B, Remy F, Ledoux A, Ruiz N. Effect of roof impacts on coupling between wave response and sloshing in tanks of LNG-carriers. *In: Proc of 27th int conf on offshore mechanics and arctic eng.* 2008.

[37] Molin B, Remy F, Rigaud S, de Jouette Ch. LNG-FPSO's: frequency domain, coupled analysis of support and liquid cargo motions. *In: Proc of IMAM conf.* 2002.

[38] Nasar T, Sannasiraj SA, Sundar V. Experimental study of liquid sloshing dynamics in a barge carrying tank. *Fluid Dynamics Res* 2008;40:427-458.

[39] Nasar T, Sannasiraj SA, Sundar V. Motion responses of barge carrying liquid tank. *Ocean Eng* 2010;37:935-946.

[40] Nasar T, Sannasiraj SA, Sundar V. Liquid sloshing dynamics in a barge carrying container subjected to random wave excitation. *J Nav Archit Mar Eng* 2012;943-65.

[41] Caluss F, Testa D, Sprenger F. Coupling effects between tank sloshing and motions of a LNG Carrier. *In: Proc of 29th int conf on offshore mechanics and arctic eng.* 2010.

[42] Nam BW, Kim Y, Kim DW, Kim YS. Experimental and numerical studies on ship motion responses coupled with sloshing in waves. *J Ship Res* 2009;53:68-82.

[43] Malenica S, Zalar M, Chen XB. Dynamic coupling of seakeeping and sloshing. *In: Proc of 13th int offshore and polar eng conf.* 2003.

[44] Newman JN. Wave effects on vessels with internal tanks. *In: Proc of 20th workshop on water wave and floating bodies.* 2005.

[45] Kim Y. A numerical study on sloshing flows coupled with ship motion – the anti-rolling tank problem. *J Ship Res* 2002;46:52-62.

[46] Kim Y, Nam BW, Kim DW, Kim YS. Study on coupling effects of ship motion and sloshing. *Ocean Eng* 2007;34:2176-2187.

[47] Lee SJ, Kim MH, Lee DH, Kim JW, Kim YH. The effects of LNG-tank sloshing on the global motions of LNG carriers. *Ocean Eng* 2007;34:10-20.

[48] Mitra S, Wang CZ, Reddy JN, Khoo BC. A 3D fully coupled analysis of nonlinear sloshing and ship motion. *Ocean Eng* 2012;39:1-13.

[49] John F. On the motion of floating bodies. *Int commun pure appl math.* 1949;2:13-57.

[50] Lee Y, Tan M, Temarel P, Miao S. Coupling between flexible ship and liquid sloshing using potential flow analysis. *In: Proc of 29th int conf on offshore mechanics and arctic eng.* 2010.

[51] Malenica S, Bigot F., Chen XB, Bralic S. Global hydroelastic model for LNG ships. *In: Proc of 26th workshop on water wave and floating bodies.* 2011.

[52] Malenica S, Choi YM, Vladimir N, Kwon SH, Chen XB. Wave induced hydroelastic behavior of the vertical circular cylinder with liquid filled tank at the top. *In: Proc of 29th workshop on water wave and floating bodies.* 2014.

[53] Ohmatsu S. On the irregular frequencies in the theory of oscillating bodies in a free surface. *Papers of Ship Res Inst* 1975;48:1-13.

[54] Kleinman RE. On the mathematical theory of the motion of floating bodies - an update. 1982. DTNSRDC-82/074.

[55] Lee CH, Newman JN, Zhu X. An extended boundary integral equation method for the removal of irregular frequency effects. *Int J Numer Meth Fluid* 1996;23:637-660.

[56] Dean RG, Dalrymple RA. *Water wave mechanics for engineers and scientists.* New Jersey, Prentice Hall: Englewood Cliffs; 1984.

[57] Wehausen JV, Laitone EV. *Surface waves.* In Encyclopedia of Physics. 1960;9:446-778.

[58] *WAMIT user manual*, 1999. Versions 6.4, WAMIT, Inc.

[59] Komar PD. *Beach processes and sedimentation.* New Jersey, Prentice Hall: Englewood Cliffs; 1976.

Summary

Numerical methods for hydro -static and -dynamic analysis of 3D elastic floating structures

본 연구를 통해 3차원 부유식 탄성 구조물의 정적/동적 해석을 위한 수치해석 기법을 개발하였다.

2장에서는 3차원 탄성 부유체의 정적 해석을 위한 비선형 구성 방정식을 제안하였다. 비선형 정적 평형 방정식은 Updated Lagrangian 정식화를 통해 incremental equilibrium equation 을 구성하였으며 유한요소법을 통해 이산화 하였다. 반복 계산 과정 중 자유수면에서 발생하는 non-matching 격자 문제를 해결하기 위해 효과적인 수치 방법을 제안 하였다. 이는 re-meshing 알고리즘을 이용할 때 발생하는 복잡한 수치해석 절차를 간소화 할 수 있다. 다양한 하중 상태 및 부유 조건에서 탄성 및 강체 부유체의 강도 해석을 통해 제안된 수치해석 기법의 가능성을 보여준다. 제안된 수치해석 기법은 탄성 및 강체 부유체의 다양한 정적/준정적 해석에 적용 가능하며, 손상된 부유체의 강도 해석에도 쉽게 적용 될 것으로 기대된다.

3장에서는 내부유체 효과를 고려한 3차원 탄성 부유식 구조물의 동적해석을 위한 구성방정식을 제안하였다. 내부유체, 파랑하중, 부유식 탄성 구조물은 직접 연성법을 통해 연성 효과를 고려하였다. 내부유체 및 구조물은 유한요소법을 통해 이산화 하였으며, 파랑하중은 경계요소법을 통해 이산화 하였다. 외부유체에서 발생하는 irregular frequency 문제를 해결하기 위해 확장된 경계 적분 방정식을 적용하였다. 제안된 수치해석 기법은 강제 부유체에 대하여 WAMIT 과 비교/검증 하였다. 또한, 3차원 탄성 부유체의 동적 해석에서 geometric stiffness 의 중요성을 보여 줌으로써, 정확한 정적 해석의 필요성을 강조하였다. 내부유체 효과를 고려한 3차원 탄성 부유체 구조물의 유타성 수치해석 결과를 비교/검증을 위해 탄성 부유체를 제작하였으며, 실험을 통해 수치해석 결과의 정확성을 뒷받침 하였다. 향후, 개발된 수치해석 기법은 다양한 해양 하중을 고려한 비선형 동적 해석에 적용 가능하며, 이를 위해 비선형 내부유체 효과를 고려한 수치해석 기법의 개발이 필요하다.